University of Alberta

Gravity currents in two-layer stratified media

by

Alan W. Tan

A thesis submitted to the Faculty of Graduate Studies and Research in partial fulfillment of the requirements for the degree of

Master of Science

in

Thermo Fluids

Department of Mechanical Engineering

Spring 2011
Edmonton, Alberta

Examining Committee

Morris R. Flynn (Supervisor), Department of Mechanical Engineering

Brian A. Fleck (Co-Supervisor), Department of Mechanical Engineering

David S. Nobes, Department of Mechanical Engineering

Bruce R. Sutherland, Department of Mathematical and Statistical Sciences

Abstract

An analytical and experimental study of boundary gravity currents propagating through a two-layer stratified ambient of finite vertical extent is presented. The theoretical discussion considers slumping, supercritical gravity currents, i.e. those that generate an interfacial disturbance whose speed of propagation matches the front speed, U and follows from the classical analysis of Benjamin [*J. Fluid Mech.* **31**, pp. 209–248, 1968]. In contrast to previous investigations, the amplitude of the interfacial disturbance is parameterized so that it can be determined straightforwardly from ambient layer depths. The theoretical model, which is applicable to the special case where the depth, D, of the gravity current fluid at the initial instant spans the channel depth, H, shows good agreement with experimental measurements and also analogue numerical simulations performed in conjunction with the present investigation. Unfortunately, it is difficult to extend our theoretical results to the more general case where $D < H$. Reasons for this difficulty will be discussed.

From experimental and numerical observations, the interface thickness, δ is observed to negligibly affect U of supercritical gravity currents even in the limit where $\delta = H$ so that the ambient fluid is linearly stratified over the whole of its depth. Conversely, subcritical gravity currents show a mild upward trend of U on δ/H. Finally, the effects of densities, ambient depths, δ and D on the horizontal position, X where deceleration first begins are considered. In contrast to the uniform ambient configuration, the gravity current can propagate without decelerating beyond 12 lock lengths and decelerate as early as 1 lock length.

Acknowledgements

I would like to take this opportunity to thank the many people that have helped me along in this journey. First and foremost, I would like to thank my primary supervisor, Dr. Morris Flynn, whom I have worked closely with over the course of the program. His patience, advice and insightful suggestions have helped a great deal in broadening my perspectives, not only in my understanding of science but also of life in general. I am also thankful to Dr. Brian Fleck, my co-supervisor, for his incredible support and encouragement and to Dr. David Nobes for the optical equipment utilized in this study and for his helpful advice on our experimental setup. I am also grateful to Dr. Bruce Sutherland for his many insights on the nature of our problem, as well as Daniel Mooney and Roger Marchand for their fabrication assistance. Lastly, I am sincerely grateful for the patience and support my beloved family and Chin Hooi Chuan have shown me.

In this study, financial support was generously provided by the Mechanical Engineering Department of the University of Alberta, Alberta Ingenuity, the Canadian Foundation for Innovation and NSERC through the Discovery Grant program.

Table of Contents

1 Introduction **1**

1.1 Gravity currents in uniform ambients 2

1.2 Gravity currents in stratified ambients 6

1.2.1 Linear stratification 6

1.2.2 Intrusive gravity currents in two-layer stratified ambient 8

1.2.3 Boundary gravity currents in two-layer stratified ambient 10

1.3 Thesis outline 11

2 Theory **13**

2.1 Model development 13

2.1.1 Full-depth lock release gravity currents 13

2.1.2 Partial-depth gravity currents 20

2.2 Model predictions for full-depth gravity currents 21

3 Experiments **28**

3.1 Thin interface experiments 29

3.2 Thick interface experiments 33

3.3 Error Analysis 35

3.3.1 Discussion on experimental error 35

3.3.2 Sample error calculation 36

4 Results and discussion **37**

4.1 Comparison between numerical and experimental results 37

4.2 Comparison of theoretical predictions and measured results for full depth gravity currents 39
4.3 Partial depth gravity currents 43
4.4 Thick interface results 49
4.5 Deceleration 52
4.6 Dimensionless numbers 56

5 Conclusions **59**
5.1 Summary of present contribution 59
5.2 Outlook and future work 61

A Derivation of the Benjamin (1968) Solution **67**

B Alternate Fr definition **70**

C Sample density profile for thick interface experiments **72**

D Conserving energy in lower or upper ambient layers for partial depth gravity currents **76**

E Interface thickness and deflection **87**

F Measured data **88**

List of Tables

F.1 Thin interface experimental data. Column labels and units are described in text. 89

F.2 Thin interface experimental data. Column labels and units are described in text. 90

F.3 Thick interface experimental data. Here $h_1' = h_2'$ and $H = 20\,\text{cm}$. Column labels and units are as described in text. 91

F.4 Experimental data for experiments considering the point of front deceleration. Here $H = 15\,\text{cm}$. Column labels and units are as described in text. 92

F.5 Measured data from numerical simulations as described in Tan et al. (2010a). Column labels and units are described in text. . . 93

F.6 Measured data from numerical simulations as described in Tan et al. (2010a). Column labels and units are described in text. . . 94

List of Figures

1.1 Definition sketch of a dense gravity current (fluid of density ρ_0) in a uniform ambient and the control volume ABCD.... 3

1.2 **a** Initial conditions for a dense gravity current of density ρ_0 in an ambient of density $\rho_1 < \rho_0$ where the initial height of the gravity current fluid, D equals the channel depth, H. **b** As with panel a but with $D < H$. 4

1.3 Illustrative sketch of a non-equilibrium intrusive gravity current (fluid of density ρ_0) in a two-layer ambient and the control volume $ABCDEF$. 8

2.1 Definition sketch of a dense gravity current (fluid of density ρ_0) and the control volume ABCD.... 14

2.2 **a** Initial conditions for a dense gravity current of density ρ_0 in a two layer ambient where the upper and lower layers span a depth of h_2' and h_1', respectively, and where the initial height of the gravity current fluid, D equals the channel depth, H. **b** As with panel a but with $h_1' < D < H$. **c** As with panel a but with $D < h_1' < H$ 17

2.3 **a** Surface plot of $c_{LW}/\sqrt{g_{02}' H}$ vs. g_{12}'/g_{02}' and h_1'/H where c_{LW} is as defined in (2.11). **b** Surface plot of $c_B/\sqrt{g_{02}' H}$ vs. g_{12}'/g_{02}' and h_1'/H where c_{LW} is as defined in (2.10). 18

2.4 Model output based on the solution of (2.5), (2.8) and (2.6). Panels **a, c, e** show, respectively, h_1/H, h_2/H and h_0/H vs. h_1'/H where the associated dimensional lengths are defined in Fig. 2.1 23

2.5 **a** Upper surface: non-dimensional gravity current speed, Fr, as defined by (2.2), vs. g_{12}'/g_{02}' and h_1'/H. Results are based upon the solution of equations (2.5), (2.8) and (2.6).... 24

2.6 As in Fig. 2.4 but showing model results based upon the solution to equations (2.5), (2.8) and (2.7). 25

2.7 As in Fig. 2.5 but showing model results based upon the solutions of equations (2.5), (2.8) and (2.7). The lower panel is based on the solutions to equation (2.13). Note that the lower surface of the upper panel is identical to that of Fig. 2.5. 26

3.1 Top down schematic diagram of the orientation of the camera with respect to the tank. Lines extending from the camera represent the field of view and θ is as shown in the diagram. 29

3.2 (LHS) Time evolution of a supercritical gravity current with $D/H = 1$, $h_1'/H = 0.50 \pm 0.01$, $g_{12}'/g_{02}' = 0.620 \pm 0.045$. (RHS) Time evolution of a subcritical gravity current with $h_1'/H = 0.25 \pm 0.01$, $g_{12}'/g_{02}' = 0.878 \pm 0.064$ 31

3.3 Time evolution of a surface-propagating supercritical gravity current with $D/H = 1$, $h_1' = 0.75 \pm 0.01$, $g_{12}'/g_{02}' = 0.755 \pm 0.069$, and $t^\star = 5.4$, 8.0, 10.7, 13.4 and 16.1. The field of view is 101 cm across by 20 cm tall. 34

4.1 (TOP ROW): Time evolution images with $h_1'/H = 0.38 \pm 0.01$, $D/H = 0.45 \pm 0.018$ and $g_{12}'/g_{02}' = 0.746 \pm 0.047$. (BOTTOM ROW): Time evolution images with $h_1'/H = 0.25 \pm 0.01$, $D/H = 0.72 \pm 0.020$ and $g_{12}'/g_{02}' = 0.511 \pm 0.045$ 38

4.2 (a) Non-dimensional amplitude, η/H, of the interfacial disturbance versus the non-dimensional ambient lower layer depth, h_1'/H. (b) η/H versus the density ratio g_{12}'/g_{02}' for $h_1'/H = 0.25$ (*upper row* of data points), $h_1'/H = 0.50$ (*middle row*) and $h_1'/H = 0.75$ (*lower row*). 40

4.3 Non-dimensional layer depths as a function of h_1'/H for $g_{12}'/g_{02}' \simeq 0.45$. Theoretical curves are based upon the solution of equations (2.5), (2.8) and (2.6); experimental data points are shown by the *solid triangles*. Representative error bars are as indicated. 40

4.4 Fr, as defined by (2.2), vs. g_{12}'/g_{02}' for a $h_1'/H = 0.25$, (b) $h_1'/H = 0.50$ and (c) $h_1'/H = 0.75$... 42

4.5 Surface plots of the non-dimensional wave amplitude, η/H versus the non-dimensional lower ambient layer height, h_1'/H, and the non-dimensional height of the lock fluid, D/H... 44

4.6 Non-dimensional wave amplitude, η/H versus density ratio, g_{12}'/g_{02}'... . 45

4.7 Time evolution of a subcritical gravity current with $D/H = 0.470 \pm 0.019$, $h_1' = 0.50 \pm 0.01$, $g_{12}'/g_{02}' = 0.752 \pm 0.064$, and $t^\star \equiv (t/H)/\sqrt{g_{02}'H} = 0.0$, 3.5, 7.1, 10.6 and 14.1. The field of view is 101 cm across by 20 cm tall. 47

4.8 Fr vs. h_1'/H for $D/H = 0.25$ (column i), $D/H = 0.50$ (column ii), $D/H = 0.75$ (column iii), and $D/H = 1$ (column iv). The top row, middle row and bottom row show solutions for $g_{12}'/g_{02}' = 0.25$, 0.50 and 0.75, respectively. 48

4.9 Normalized front speed versus the normalized interface thickness. (a) Supercritical flows, (b) subcritical flows... 51

4.10 Front position versus time for four subcritical gravity currents with $g_{12}'/g_{02}' \simeq 0.911$... 53

4.11 Flow snapshots corresponding to points 1, 2 and 3 (panels a) and 4, 5 and 6 (panels b) from Fig. 4.10. In all cases, the field of view is 101 cm across by 15 cm tall. 54

4.12 Normalized point of first deceleration, X/ℓ, vs. (a) h_1'/H for $g_{12}'/g_{02}' = 0.900$ (circles), $g_{12}'/g_{02}' = 0.785$ (triangles), and, $g_{12}'/g_{02}' = 0.694$ (squares) with $\delta/H \simeq 0.123$; (b) g_{12}'/g_{02}' for various h_1'/H with $\delta/H \simeq 0.123$; (c) δ/H for various g_{12}'/g_{02}' with $h_1' = h_2'$; and, (d) D/H for various g_{12}'/g_{02}' with $h_1'/H = 0.50$... 57

A.1 Definition sketch of a dense gravity current (fluid of density ρ_0) in a uniform ambient and the control volume ABCD... 67

B.1 Fr_e, as defined by (2.2), vs. h_1'/H for $g_{12}'/g_{02}' = 0.250$, (b) $g_{12}'/g_{02}' = 0.500$ and (c) $g_{12}'/g_{02}' = 0.750$... 71

C.1 Sample density profile for the ambient of a "thin" interface experiment. 73

C.2 Sample density profile for the ambient of a thick interface experiment. 74

C.3 Sample density profile for the ambient of a intermediate thickness interface experiment. 75

D.1 Model output based on (2.5), (2.6) and (2.14). Panels a–d show h_1/H vs. h_1'/H with $D/H = \frac{1}{4}, \frac{1}{2}, \frac{3}{4}$ and 1, respectively. Panels e–h show h_0/H vs. h_1'/H with $D/H = \frac{1}{4}, \frac{1}{2}, \frac{3}{4}$ and 1, respectively... 79

D.2 As in Fig. 2.4, but showing the non-dimensional velocities $u_1/\sqrt{g_{02}'H}$ (panels a–d) and $u_2/\sqrt{g_{02}'H}$ (panels e–h) 80

D.3 (Upper images): Non-dimensional gravity current speed, Fr, vs. g'_{12}/g'_{02} and h'_1/H (upper surface). (Lower images): Non-dimensional dissipation function, $\Delta R/(g'_{02}H)$, as defined by (2.12).... 81

D.4 As in Fig. 4.8 but showing model results based upon the solutions to equations (2.5), (2.6) and (2.14). 82

D.5 As in Fig. 2.4 but showing model results based upon the solution to equations (2.5), (2.7) and (2.14). 83

D.6 As in Fig. D.2 but showing model results based upon the solution to equations (2.5), (2.7) and (2.14). 84

D.7 As in Fig. D.3 but showing model results based upon the solution to equations (2.5), (2.7) and (2.14). The non-dimensional dissipation function is calculated using (2.13). 85

D.8 As in Fig. 4.8 but showing model results based upon the solutions to equations (2.5), (2.7) and (2.14). 86

E.1 The correlation of interface thickness and deflection for a range of values of g'_{12}/g'_{02}. For the experiments considered here, $h'_1 = h'_2$. Representative error bars are as indicated. 87

Chapter 1

Introduction

Gravity currents are primarily horizontal flows driven by differences in density that occur frequently in natural and man-made situations. As discussed in the extensive monologue by Simpson (1997), avalanches which have an increased density due to suspended particulate and sea breeze fronts that arise in coastal regions due to differential heating between land and sea are familiar examples of this phenomena. In our everyday lives, gravity currents manifest themselves as the cool draft that is felt as one opens the door after a hot shower. Including surface tension, an oil spill which propagates radially away from a source along the surface of sea water is also an example of this phenomena. For many decades, researchers and engineers have been studying gravity currents, not only to understand the dynamics of the above mentioned phenomena but also to be used in numerical weather prediction models, the design of low energy building ventilation systems, understanding the impacts on aircraft safety, etc. The remainder of the introduction will be organized as follows: § 1.1 will cover the background of gravity currents propagating into uniform ambients and § 1.2 will cover gravity currents in stratified ambients; specifically linearly stratified and two layer ambients. In all cases, discussion will be restricted to rectilinear geometry. Examples of axisymmetric gravity currents are given by Ungarish (2009).

1.1 Gravity currents in uniform ambients

The rectilinear gravity current propagating into a uniform ambient is the simplest and most studied class of the phenomena. Early research by Keulegan (1957) and Hoult (1972), have found that these types of gravity currents evolve through three distinct phases: (1) a slumping phase where the gravity current propagates at a constant speed, (2) an inertial-buoyancy phase and finally, (3) a viscosity-buoyancy phase where viscous forces become important. As discussed by Rottman and Simpson (1983), the front speed decreases as $t^{-1/3}$ and $t^{-4/5}$ in the 2nd and 3rd phases, respectively. As the slumping phase typically ends after 6-10 lock lengths (Huppert & Simpson 1980), replicating the 2nd and 3rd phases in the laboratory requires a long tank which poses difficulties in terms of cost and setup time. Due to these experimental challenges (and related difficulties associated with running complementary numerical simulations), most studies focus on the constant speed slumping phase.

Simpson & Britter (1979) performed an experimental study on the dynamics of the head of a gravity current advancing over a horizontal surface. The experimental apparatus utilized in the experiments was designed such that the front was held stationary by an opposing recirculating flow. In their study, they discovered that the foremost point of the head is slightly elevated which results in ambient fluid being over-run by the gravity current. Due, however, to the associated density differences, the entrained ambient fluid then rises to the top of the gravity current head. This, along with shear instabilities between the two fluids, forms a secondary mixing layer which sits above the denser layer. As an additional consequence of less dense fluid being over-run by the gravity current head, complicated three-dimensional lobes and clefts form (see Fig. 1.3 and Fig. 11.3 of Simpson 1997). Moreover, over an extended range, they measured the speed of the gravity current, rate of mixing between the ambient and

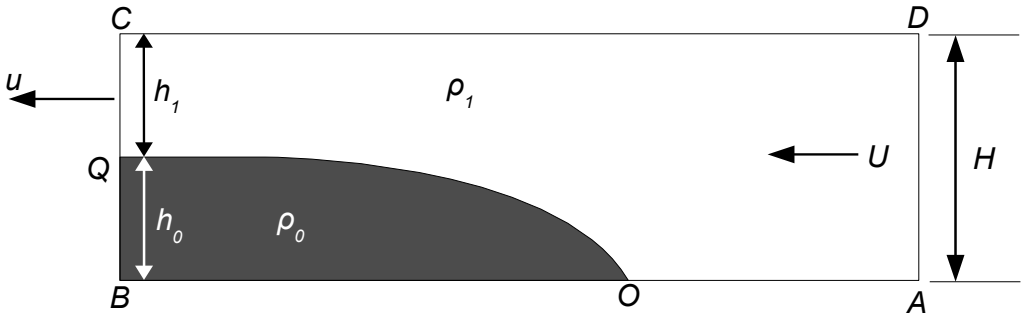

Figure 1.1: Definition sketch of a dense gravity current (fluid of density ρ_0) and the control volume $ABCD$.

gravity current fluids, and the relative depths of the mixed layer.

A theoretical description of the speed of a gravity current during the slumping phase was first derived by Benjamin (1968) based on observations of an air cavity propagating into a channel of water. In Benjamin's analysis, as illustrated schematically in Fig. 1.1, he considered a gravity current of density ρ_0 propagating, at a speed of U, into a uniform ambient of density $\rho_1 < \rho_0$ and depth, H. A reference frame that is moving with the gravity current front was utilized so the steady state assumption can be applied. Additionally, it was assumed that (1) the flow is hydrostatic far up- and downstream, (2) fluid exchange between the layers is negligible, (3) the top and bottom boundaries of the control volume are rigid surfaces and (4) $\mathrm{Re} \equiv UH/(2\nu)$ is sufficiently high such that viscosity effects are negligible. By employing mass and momentum conservation far up- and downstream of the front, an expression relating U and h_0. By requiring that energy be conserved within the ambient layer, two unique solutions were obtained: (1) $h_0/H = \frac{1}{2}$ with $\mathrm{Fr} = U/\sqrt{g'_{02}h_0} = \frac{1}{\sqrt{2}}$ and (2) $h_0/H \to 0$ with $\mathrm{Fr} \to \sqrt{2}$, where $g'_{02} = g(\rho_0 - \rho_1)/\rho_1$. The former solution is most often seen in laboratory lock release experiments that have initial conditions as illustrated in Fig. 1.2 a where the initial height of the gravity current fluid, D, matches the channel height, H. These experiments have been described by Huppert &

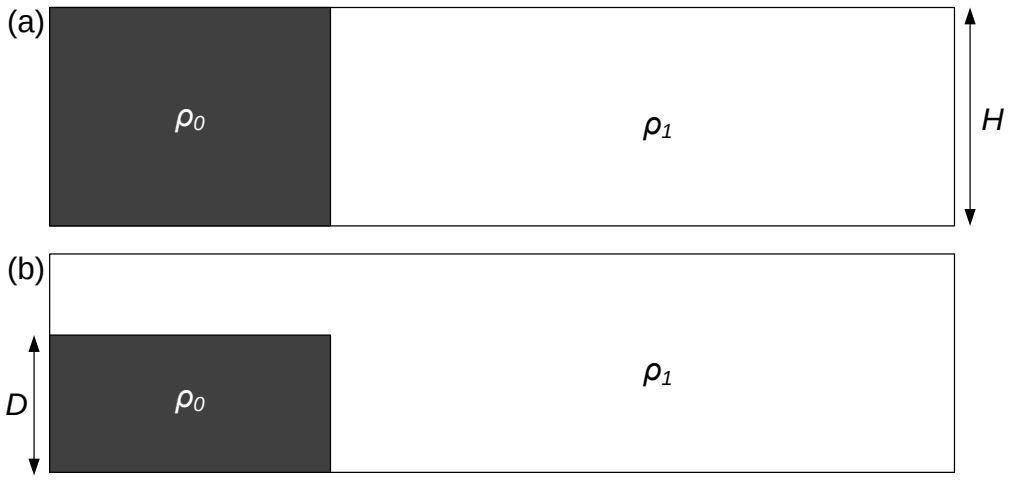

Figure 1.2: **a** Initial conditions for a dense gravity current of density ρ_0 in an ambient of density $\rho_1 < \rho_0$ where the initial height of the gravity current fluid, D equals the channel depth, H. **b** As with panel a but with $D < H$.

Simpson (1980), Shin et al. (2004) and Tan et al. (2010 a). The derivation of the model by Benjamin is outlined in Appendix A.

Huppert & Simpson (1980) proposed a simple alternate model that utilized a relation between Fr and h_0 developed using a curve-fit of experimental data. To close the problem, they assumed that the gravity current slumps through a series of equal area rectangles. With this model, they were able to satisfactorily predict the speed of propagation, duration and length of the constant speed slumping phase. Hoult (1972) developed spreading laws for the inertia-buoyancy and viscosity-buoyancy phases through analysis of depth averaged shallow water equations and omitting the viscosity terms and inertia terms, respectively. Through comparisons with these spreading laws, Huppert & Simpson were able to extend their model to predict the length and duration of the 2nd and 3rd phases.

By solving the shallow water equations (Baines 1995) for two layer fluids, Rottman and Simpson (1983) were able to model gravity currents in uniform ambients for the more general partial depth case, as illustrated in Fig. 1.2 b,

where $D < H$. These equations were derived by assuming that vertical accelerations are negligible and are therefore inapplicable at the gravity current front. In order to compensate for this, they imposed a front condition which was the relation between U and h_0 developed by Benjamin (1968) multiplied by a dimensionless fitting factor, $\beta^2/2$. By setting $\beta^2 = 1$ and solving the shallow water equations, they were able to calculate the speed of the gravity current during the slumping phase. However, their results were quantitatively accurate only when $D/H < 0.5$ but provided a qualitative understanding of the phenomena for the the entire range (i.e. $0 < D/H \leq 1$).

Taking a different approach, Shin et al. (2004) derived an alternate theory to predict the speed of propagation for a partial depth gravity current. In contrast to Benjamin's approach, which considers only the front in a reference frame that is moving at the same speed, Shin et al. (2004) considered the entire system which allowed for the dynamics of the upstream propagating disturbance[1] and the details of the initial conditions to be accounted for. However, in their analysis, a simplifying assumption was made; i.e. the gravity current takes the shape of an box with a upstream propagating bore[2]. In general, experiments have observed that the disturbance is typically a rarefraction wave rather than a constant shape bore when $D/H \lesssim 0.8$ (Rottman & Simpson 1983). This assumption resulted in significant simplifications of the analysis, the most important of which are: (i) ambient velocity can be represented by a variable that is independent of the horizontal position, and (ii) work terms associated with the front and the upstream propagating disturbance cancel out. While model predictions show good agreement with measured results, some re-

[1] A disturbance that propagates back into the lock once the vertical barrier is removed (see Fig. 4 of Shin et al. 2004).

[2] According to Baines (1995), a bore (also known as a hydraulic jump) is a locally steady phenomena located in a compact region that can be modeled as discontinuity between two streams of fluid propagating uniformly. This phenomena is caused by the steepening of a wave.

searchers (e.g. Ungarish 2009) are of the opinion that the theoretical model is fundamentally flawed due to the restrictive nature of the assumptions.

1.2 Gravity currents in stratified ambients

Stratification in the environment occurs frequently due to variations in humidity, density, temperature, suspended particulate, etc. and can be caused by both natural and man-made influences. Examples of natural occurrences of stratification are (1) temperature inversions which most significantly affect cities which are located in valleys or surrounded by mountainous terrain as described by Fernando et al. (2001) and (2) stratified lakes and other large bodies of water due to surface heating from the sun. Stable stratification is a hallmark of a well designed, naturally-ventilating building; displacement ventilation, as identified by Linden et al. (1990), where inflow and outflow occurs at low and high levels respectively, provides an especially familiar example. This stably stratified configuration can also occur if there are internal sources of buoyancy within the building (e.g. heaters, cooking devices and people) and openings for exchange of air with the exterior.

In the context of gravity currents, these types of fluid configurations can play an important role in the dynamics of pollutant and nutrient transport particularly in the speed and distance of travel. Indeed, as will be outline more carefully below, a major objective of this thesis is to identify the effects of the relative depths and densities of a two-layer ambient system on the front speed.

1.2.1 Linear stratification

Maxworthy et al. (2002) performed a series of experiments and numerical simulations to study the constant front speed during the initial slumping phase of a rectilinear gravity current propagating along the bottom boundary of a linearly stratified ambient in a tank with a free upper surface. The results from

their high-resolution two-dimensional numerical simulations agreed well with laboratory measurements. Additionally, they provided a set of curve-fit equations derived from experimental data which were utilized by subsequent studies (e.g. Ungarish & Huppert 2002) for model verification.

Ungarish and Huppert (2002) developed a model using the one-layer shallow water equations and the Huppert and Simpson (1980) front condition which allowed for the prediction of the front speed during the initial slumping phase. The principal assumptions of the model were that the fluid in the ambient layer is infinitely deep and thus effectively stationary, the pressure is hydrostatic and internal wave effects are negligible. The analysis satisfactorily captured the effects of stratification on the speed of propagation for the constant speed slumping phase. Additionally, simplified analytical solutions for the special cases where $g'_{12}/g'_{02} \equiv (\rho_1 - \rho_2)/(\rho_0 - \rho_2) = 0$ and 1 were provided, where ρ_0, ρ_1 and ρ_2 are the densities for the gravity current fluid, ambient fluid at $z = 0$ and $z = H$, respectively. By defining an effective $\mathrm{Fr}_e = U/\sqrt{g'_e D}$ where $g'_e = g[\rho_0 - \rho(z = \frac{1}{4}D)]/\rho_2$, they were able to scale U such that it is approximately independent of g'_{12}/g'_{02}.

Ungarish (2006) took a different approach and derived a generalization of the Benjamin (1968) solution for a gravity current propagating into a linearly stratified ambient. By utilizing Long's flow field solution as described in Baines (1995) with Benjamin's flow force balance, a solution was obtained that allowed for the prediction of Fr as a function of the height of the gravity current, h_0 and the stratification of the ambient fluid without having to solve the partial differential equations inherent to shallow water models. At the limiting case where $g'_{12}/g'_{02} = 0$, the results derived by Benjamin (1968) were recovered. The theoretical solutions agreed satisfactorily with measured results by Maxworthy et al. (2002).

1.2.2 Intrusive gravity currents in two-layer stratified ambient

As described below, an intrusion or an intrusive gravity current is one that propagates along a sharp interface and has been extensively studied over the past several decades. An equilibrium intrusion, where the density of the gravity current is equivalent to the depth-weighted mean density of the ambient fluid, can be modeled as a boundary gravity current propagating along a free-slip surface into a uniform ambient. Using the energy conserving solution of Benjamin (1968), a prediction of the constant speed of propagation during the initial phase can be obtained. However, for the non-equilibrium case, the problem is more complex and a more involved approach is required.

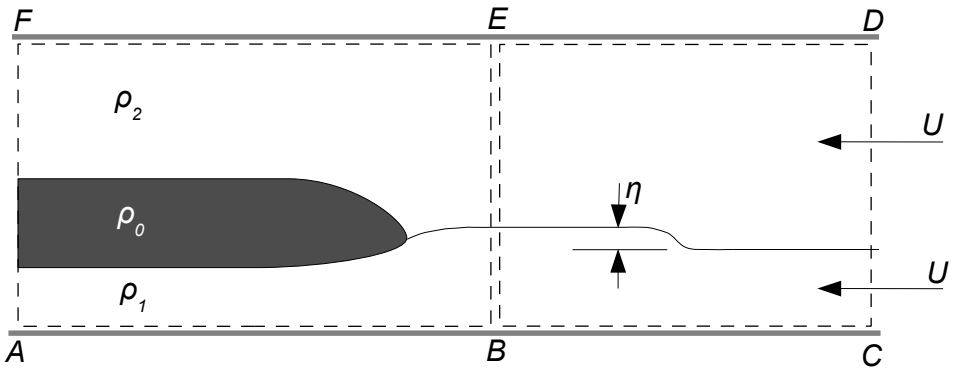

Figure 1.3: Illustrative sketch of a non-equilibrium intrusive gravity current (fluid of density ρ_0) in a two-layer ambient and the control volume $ABCDEF$.

The problem was first approached by Holyer & Huppert (1980) where they utilized Benjamin's approach to derive a predictive model. Using mass and momentum conservation in the Boussinesq limit (i.e. small density differences) in conjunction with Bernoulli's equation applied along the upstream interface, they were able to obtain an expression for the speed of propagation. The results obtained agreed well for the equilibrium case but significantly under-predicted gravity current speeds in the non-equilibrium case. Guided by detailed ex-

perimental images and insights on dynamics of intrusions by Sutherland et al. (2004), Flynn & Linden (2006) were able to develop a successful model that is a modification of Holyer & Huppert's. The control volume, as illustrated schematically in Fig. 1.3, remains attached to the front as it propagates along and is partitioned into two sections. Subsequently, utilizing mass and momentum conservation with Bernoulli's equation applied along the upper and lower layer of the stationary intrusion section as well as along the interface upstream, they were able to arrive at three equations and five unknowns. Finally, to close the system, they coupled the aforementioned equations with the exact solution of the two-layer shallow water equations as described in Baines (1995), and a parameterization for the wave amplitude, η based on initial conditions which accounted for the evolution of the non-linear wave. The results of the model were in very good agreement with the numerical simulations and experimental results, through comparisons between measured and predicted front speeds.

Sutherland and Nault (2007) performed a study of the effects of the interface thickness on the dynamics of the intrusive gravity current. In the doubly symmetric case, the speed of propagation decreases from the two-layer prediction derived by Benjamin (1968) to approximately half of that value when the ambient is linearly stratified (Faust & Plate 1984). Additionally, when the interface is thin but non-zero, a "leaky" closed core solitary wave is excited that carries the intrusion for large distances (>22 lock lengths) without decelerating. This is in stark contrast to boundary gravity currents propagating into a uniform ambient where deceleration begins at approximately 6-10 lock lengths (Huppert & Simpson 1980, Rottman and Simpson 1983).

1.2.3 Boundary gravity currents in two-layer stratified ambient

The boundary gravity current propagating into a two-layer stratified ambient has recently been studied by several groups over the past. Rottman and Simpson (1989) investigated the formation of "Morning Glory" phenomena by gravity currents. Specifically, they focused their attention on the special case where the lower ambient layer, h_1' is small relative to the channel height, H. By utilizing the hydraulic theory of Holyer & Huppert (1980), they were able to predict many of the qualitative features of a bore excited by a gravity current. However, those models proved quantitatively inaccurate.

The first model for the configuration where both ambient layers are of finite height was by Hoyler & Huppert (1980) which utilized an extension of the theory by Benjamin (1968) to predict the speed of propagation during the initial slumping phase. Applying the typical convention of a reference frame that is moving with the front, the gravity current appears stationary and can be treated as a steady state problem. Mass and momentum conservation (flow force balance) is then applied to arrive at one equation and three unknowns. To close the system, they assumed that energy is conserved within the control volume by applying Bernoulli's equation along the upper and lower ambient layer. However, as with the case of the intrusive gravity current discussed earlier, the solutions to the model equations yielded multiple solutions. To reconcile this, they proposed an additional constraint that for a fixed volume inflow rate, the realizable physical solution is obtained by maximizing dissipation and hence the mass flux associated with the gravity current.

1.3 Thesis outline

In this thesis, an alternate theory is presented which utilizes an explicit relation, derived through heuristic reasoning, of the amplitude of an interfacial disturbance that appears along the ambient interface. By coupling this with mass and momentum conservation and Bernoulli's equation applied along either, but not both, the upper or lower ambient layer, analytical predictions are obtained that are devoid of multiple solutions. A discussion of the challenges associated with extending this model to the more general case where $D < H$ will also be reviewed.

The rest of thesis is organized as follows: in §2.1.1 Benjamin's discussion is adapted so as to predict the initial front speed of a full depth boundary gravity current propagating through a two-layer medium. In §2.1.2, attempts to extend this theory to the more general partial depth case where $D < H$ is discussed. Model fidelity is tested by contrasting theoretical solutions against the output of analogue experiments, which are described in §3, and numerical simulations, which are described in Tan et al. (2010a). A comparison between numerical simulations and analogue experiments are presented in §4.1. Results of the comparison between the model and measured results are presented in §4.2 and §4.3. In §4.4, the impact of the interface thickness is considered and in §4.5 the point at which the gravity current front begins to decelerate is examined. Finally, conclusions and applications of this work are discussed in §5.

Portions of the thesis have appeared in Tan et al. (2010a). The present research was also discussed at a pair of conferences: Wave Phenomena IV held in June 2010 at the University of Alberta and the International Conference of Environmental Science and Engineering held in Aug. 2010 in Singapore. As part of the latter, a conference proceeding (Tan et al. 2010b) was prepared which outlines the sensitive dependence of the interfacial disturbance on the

initial conditions. Writing responsibilities for journal manuscript were shared between the author of this thesis and Dr. Morris R. Flynn, who also edited my contribution with additional editorial input from Drs. Brian A. Fleck and David S. Nobes. The conference proceeding was primarily written by the author of this thesis; minor revisions were suggested by Dr. Flynn.

Throughout the thesis, numerical and experimental results are presented. The author only contributed the latter data but numerical simulation results are herein included with the purpose of validating the experimental results. Details on the numerical simulations can be found in Tan et al. (2010a).

Chapter 2

Theory

2.1 Model development

2.1.1 Full-depth lock release gravity currents

The primarily horizontal flow of a gravity current, illustrated schematically in Fig. 2.1, is considered. The dense current of density ρ_0 propagates into a two-layer ambient where the lower and upper layers have densities $\rho_1 < \rho_0$ and $\rho_2 < \rho_1$ and undisturbed depths h_1' and h_2', respectively. Due to the forcing imparted by the gravity current, the ambient layers are assumed to contract so that far downstream in a translating reference frame (i.e. far to the left in Fig. 2.1), the lower and upper layer depths are, respectively, h_1 and h_2. Correspondingly, the interfacial disturbance is assumed to vary monotonically with amplitude η. Conditions under which the above assumptions cannot be justified are identified in §2.2. Far upstream of the forward stagnation point, O, the fluid velocity, U, in the ambient layers is equal whereas far downstream of O, the contracted lower and upper layers have associated depth-independent velocities u_1 and u_2, respectively. The parameters U, u_1 and u_2 may be related by applying mass conservation, i.e.

$$u_1 h_1 = U h_1' \qquad \text{and} \qquad u_2 h_2 = U h_2'. \tag{2.1}$$

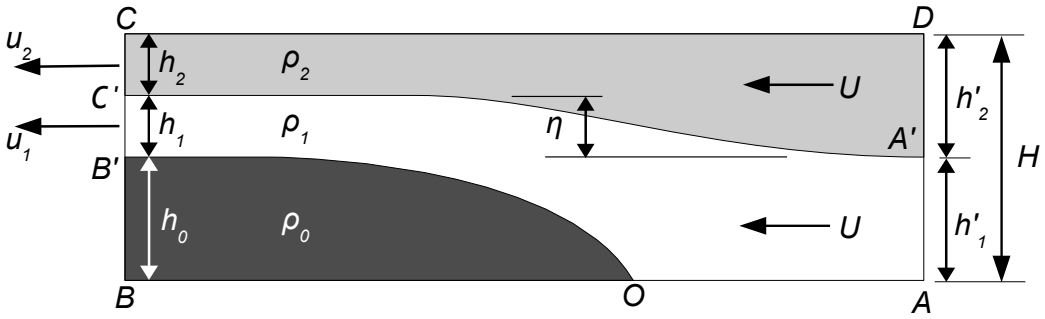

Figure 2.1: Definition sketch of a dense gravity current (fluid of density ρ_0) and the control volume $ABCD$. The frame of reference is chosen so that the gravity current is at rest relative to a moving two-layer ambient, which flows, without mixing, from right to left.

Note that U is the speed of propagation of the gravity current in the laboratory reference frame. Consideration is herein restricted to the incipient slumping phase of motion for which U, or its non-dimensional analogue

$$\text{Froude number, Fr} \equiv \frac{U}{\sqrt{g'_{02}H}} \tag{2.2}$$

is time independent so that the flows exhibited schematically in Fig. 2.1 can be considered steady. This definition of Fr differs from the one shown previously and is applicable for configuration depicted in Fig. 2.1. An alternative definition for Fr, which is more representative of the ambient configuration as Benjamin's energy conserving solution of $\text{Fr} = \frac{1}{2}$ is recovered when h'_1/H is either 0 or 1, is also possible and is discussed briefly in Appendix B. From Fig. 2.1, $H = h'_1 + h'_2$ is the total channel depth and the reduced gravity g'_{02} is defined as $g(\rho_0 - \rho_2)/\rho_{00}$ in which ρ_{00} is a reference density and g is gravitational acceleration. By assumption, the Boussinesq approximation applies so that $g'_{02} \ll g$. Consistent with Benjamin (1968) and numerous follow-up studies, it is assumed that, away from the gravity current front, vertical accelerations are negligible so that the pressure field is hydrostatic. Accordingly, along the vertical segment AD,

$$p = \begin{cases} -\frac{1}{2}\rho_1 U^2 - \rho_1 g z & 0 \le z \le h'_1 \\ -\frac{1}{2}\rho_1 U^2 - \rho_1 g h'_1 - \rho_2 g(z - h'_1) & h'_1 < z \le H \end{cases} \tag{2.3}$$

Here Bernoulli's equation has been applied in writing the pressure at point A, $p_A = -\frac{1}{2}\rho_1 U^2$; without loss of generality the pressure at the stagnation point, p_O, is taken to be zero. Similarly, along the vertical segment BC,

$$p = \begin{cases} -\rho_0 g z & 0 \leq z \leq h_0 \\ -\rho_0 g h_0 - \rho_1 g (z - h_0) & h_0 < z \leq h_0 + h_1 \\ -\rho_0 g h_0 - \rho_1 g h_1 - \rho_2 g (z - h_0 - h_1) & h_0 + h_1 < z \leq H \end{cases} \tag{2.4}$$

where h_0 is the gravity current height as defined in Fig. 2.1. These results are independent of shear. Bernoulli's equation with associated loss terms will separately be applied so that pressure remains continuous across the interfaces. Equations 2.3 and 2.4 may be applied in writing the following expression for horizontal momentum (or "flow force") conservation:

$$\begin{aligned} \int_A^D p + \rho u^2 \, \mathrm{dz} &= \int_B^C p + \rho u^2 \, \mathrm{dz} \Leftrightarrow \\ \frac{1}{2} U^2 H + \frac{1}{2} g'_{02} H^2 &= g'_{12} \left[h'_1 \left(H - \frac{1}{2} h'_1 \right) + \frac{1}{2} h_2^2 \right] + \frac{1}{2} g'_{01} (h_1 + h_2)^2 \\ &\quad + U^2 \left(\frac{h_1'^2}{h_1} + \frac{h_2'^2}{h_2} \right) \end{aligned} \tag{2.5}$$

Here g'_{01} is defined similarly to g'_{02} and (2.1) has been applied in writing, for example, u_1 in terms of U, h_1 and h'_1. This equation shows the appropriate limiting behaviour when compared against Benjamin's solution with h_2, $h'_2 \to 0$ and $\rho_2 \to \rho_1$. Equation (2.5) represents a general equation with three unknowns (U, h_1, h_2) and consequently two further relations are needed for model closure.

In the dissipation-free analysis of Holyer and Huppert (1980), as discussed in §1.2.3, Bernoulli's equation is applied immediately above the streamlines OB' and $A'C'$ requiring energy to be conserved in the two ambient layers. Hence

$$\frac{1}{2} U^2 = g'_{01} \frac{h_1^2}{h_1'^2} (H - h_1 - h_2) \tag{2.6}$$

and

$$\frac{1}{2} U^2 = \frac{h_2^2}{h_2'^2} \left[g'_{02} (H - h_1 - h_2) - g'_{12} (h'_1 - h_1) \right] \tag{2.7}$$

respectively. Application of both equation (2.6) and (2.7) is potentially problematic, however, particularly when the interfacial disturbance takes the form of a bore: from the discussion of Baines (1995, §3.5), two-layer bores do not conserve energy in both the expanding and contracting layers. Although this difficulty can, in principle, be resolved by defining layer-specific dissipation functions (see e.g. equations 4.3 and 4.4 of Holyer and Huppert 1980), the introduction of these two additional parameters requires that further assumptions be made and/or that further quantities such as the volume inflow of fluid of density ρ_0 be specified. Opportunities for model validation by comparison with experimental data are correspondingly restricted, particularly when one considers the finite-volume or lock release, long the staple experimental configuration for gravity current flows (Simpson 1997).

Here, the aim is to develop a model whose output is (i) devoid of the multiplicities that characterize Holyer and Huppert's energy-conserving solutions, and, (ii) easily comparable against the data from full-depth lock release experiments, illustrated schematically in Fig. 2.2 a, where $D = H$. In this vein, the equation (2.5) is retained along with one, but not both, of equation (2.6) or (2.7). For model closure, the amplitude of the interfacial disturbance is parameterized as follows:

$$\eta = \frac{1}{2}H - \frac{1}{2}h_1' \tag{2.8}$$

so that the deflection to the ambient interface is governed by the vertical scale of the gravity current. Note from Fig. 2.1, however, that $\eta = h_2' - h_2$. Thus equation (2.8) yields

$$h_2 = \frac{1}{2}h_2' \tag{2.9}$$

showing that the upper ambient layer contracts to one-half its original depth, i.e. $u_2 = 2U$. In a similar spirit to the analysis of Cheong et al. (2006), (2.8) is motivated by judicious examination of relevant limiting cases. When

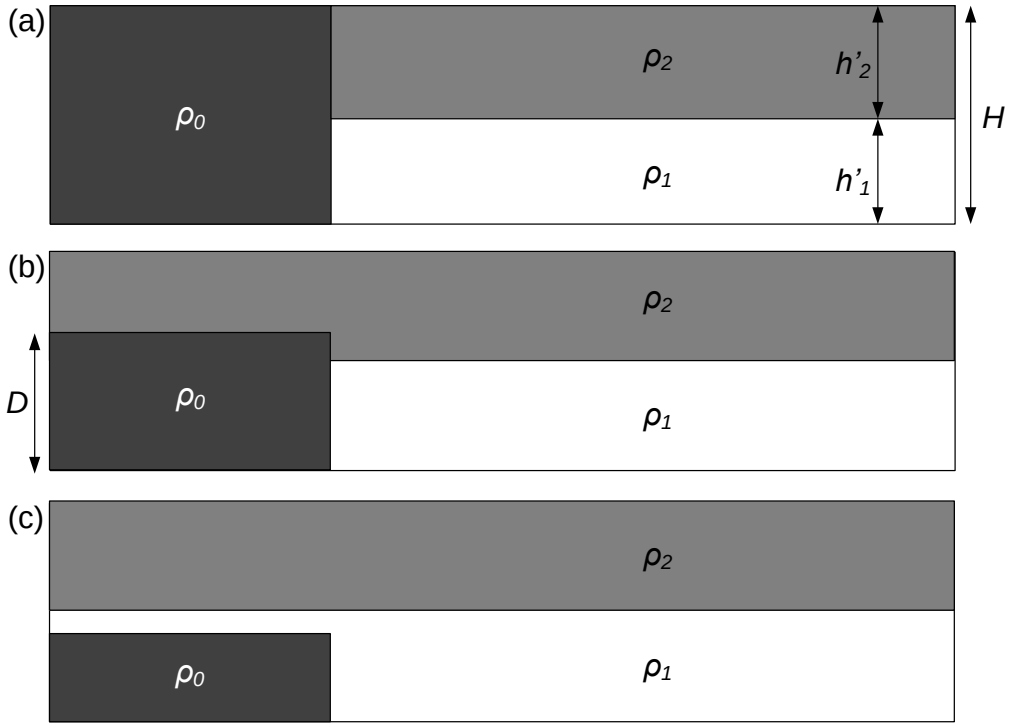

Figure 2.2: **a** Initial conditions for a dense gravity current of density ρ_0 in a two layer ambient where the upper and lower layers span a depth of h_2' and h_1', respectively, and where the initial height of the gravity current fluid, D equals the channel depth, H. **b** As with panel a but with $h_1' < D < H$. **c** As with panel a but with $D < h_1' < H$

$h_1' \to 0$, Benjamin's energy-conserving solution predicts $h_0/H \to 1/2$ and thus $\eta/H \to 1/2$. Conversely, when $h_1' \to H$ the upper ambient layer is vanishingly thin so that $\eta \to 0$. Equation (2.8) is constructed by connecting these limiting cases with a straight line. Although this is the simplest possible functional dependence, the agreement with experimental and numerical data, to be considered in §4.1, will be shown to be satisfactory, suggesting that a more complicated relation, in particular one incorporating layer density information, is not required.

To flesh out the appropriate analytical details, observations from preliminary experiments showed that the interfacial disturbance takes the form of a long wave and a bore, respectively, as $h_1'/H \to 1$ and $h_1'/H \to 0$. From Baines

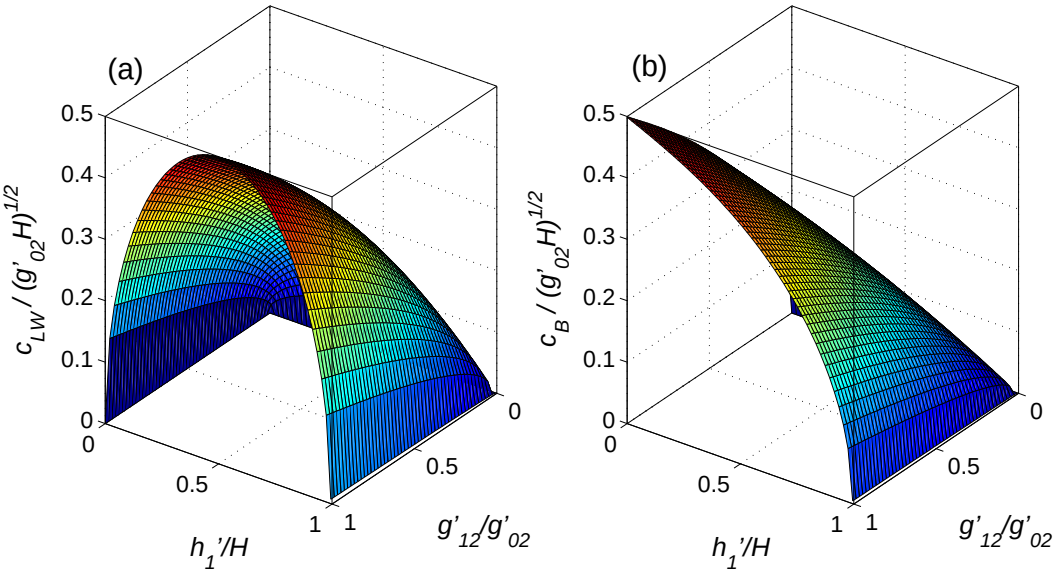

Figure 2.3: **a** Surface plot of $c_{LW}/\sqrt{g'_{02}H}$ vs. g'_{12}/g'_{02} and h'_1/H where c_{LW} is as defined in (2.11). **b** Surface plot of $c_B/\sqrt{g'_{02}H}$ vs. g'_{12}/g'_{02} and h'_1/H where c_{LW} is as defined in (2.10).

(1995), the long wave speed can be written as:

$$c_{LW} = \sqrt{g'_{12}\frac{h'_1 h'_2}{H}} \tag{2.10}$$

Meanwhile Klemp, Rotunno & Skamarock (1997) argue that the bore speed is given by

$$c_B = \sqrt{\frac{g'_{12}(h'_1+\eta)^2(H-h'_1-\eta)(2H-2h'_1-\eta)}{H^2(2h'_1+\eta)-H(h'_1+\eta)(2h'_1-\eta)}}. \tag{2.11}$$

For comparison, Fig. 2.3 shows $c_{LW}/\sqrt{g'_{02}H}$ (panel a) and $c_B/\sqrt{g'_{02}H}$ (panel b) plotted against g'_{12}/g'_{02} and h'_1/H. From the experimental images, it is difficult to ascertain the exact point at which the interfacial disturbance changes from long wave-like to bore-like. Indeed, in the latter case, and consistent with experimental images presented by Rottman & Simpson (1989), Lim, Ivey & Nokes (2008) and others, moderate interfacial slopes are observed as compared to the idealized discontinuity of layer depths shown, for example, in Fig. 3.6 of Baines (1995). Nonetheless, it is reasonable to expect transition near $h'_1 = 0.299$ where $c_{LW} = c_B$ (c.f. equation 6.5 of Shin, Dalziel & Linden 2004). When $U >$

$\max(c_{LW}, c_B)$, the interfacial disturbance of Fig. 2.1 is expected to remain fixed to the gravity current front. However, when $U < \max(c_{LW}, c_B)$, this interfacial disturbance is expected to propagate ahead of the front. In this latter case, the assumption of a steady flow is invalid. As will be demonstrated in the following section, the point of model breakdown is in general close to the point at which the gravity current transitions from supercritical to subcritical.

Equations (2.5), (2.8) and (2.6) or (2.7) represent a closed system of algebraic equations from which follow predictions for h_1, h_2, η and U. It should be emphasized, however, that there is no material difference between applying Bernoulli's equation along the upper surface of OB' or the lower surface of $A'C'$; in either case, energy must be conserved in layer 1 so that (2.6) applies. Thus the distinction between (2.6) and (2.7) is one of rather limited degree: is energy conserved above the ambient interface (i.e. in the upper ambient layer) or below the ambient interface (i.e. in the lower ambient layer)?

Energy dissipation may be estimated by evaluating the change of the Bernoulli function, $R = \frac{1}{2}u^2 + gz + p/\rho$, between A' and C' in whichever layer is not assumed to conserve energy so that Bernoull's equation may be applied. For example, if energy is conserved in the lower and upper ambient layer, it can be shown that

$$\Delta R_{A'C'} = 2\left(\frac{h_2}{h_2'}\right)^2 [g_{12}'(h_1 - h_1') + g_{02}'(H - h_1 - h_2)] - U^2 \tag{2.12}$$

and

$$\Delta R_{OB'} = 2g_{01}'\left(\frac{h_1}{h_1'}\right)^2 (H - h_1 - h_2) - U^2 \tag{2.13}$$

respectively. In distinguishing between physical and unphysical solutions, ΔR is expected to be positive signifying that energy is dissipated in moving from right to left in Fig. 2.1. Solutions with $\Delta R < 0$ require an unphysical addition of mechanical energy and are therefore ignored.

2.1.2 Partial-depth gravity currents

Equation (2.8) is implicitly limited to a special class of gravity currents, namely those that, in the context of the canonical lock-exchange experiment, occupy the entire channel depth, H, at $t = 0$. From previous studies with a uniform ambient where the gravity current fluid initially occupies a depth $D < H$, it is well known that the half-depth solution is not recovered (see e.g. Fig. 13 of Shin et al. 2004). Thus equations (2.5), (2.8) and (2.6) or (2.7) cannot be expected to be accurate for this more general category of "partial depth" lock releases, illustrated schematically in Fig. 2.2 b and c, which are truer analogues of numerous environmental flows as compared to the special, though experimentally convenient, case $D = H$. Rather, the following new parameterization of η is proposed, which yields $\eta \to 0$ as $h_1' \to H$, recovers (2.8) when $D = H$ and specifically incorporates the geometric variable D:

$$\eta = \frac{D}{H}\left[\alpha - (\alpha - \frac{1}{2})\frac{D}{H}\right](H - h_1'). \tag{2.14}$$

In equation (2.14), the numerical value of α is obtained from the measurements of Rottman & Simpson (1983), who performed a series of partial-depth lock release experiments in ambient fluid of uniform density. From Fig. 10 of their paper, $\alpha = 0.867 \pm 0.017$. Deriving an estimate of α from first principles is a complicated problem that is beyond the scope of the present inquiry. The uncertainty associated with α was obtained by calculating the standard error for the estimated slope of a linear regression line as described in Chapter 9.1 of Moore and McCabe (1993).

The combination of equations (2.14) and (2.5) yields an incomplete system of algebraic equations (i.e. two equations, three unknowns). In order to close the system, several methods have been explored. Utilizing (2.6) as the third equation results in non-physical behaviour in the limiting case, $h_1'/H \to 1$. Observations of experiments and numerical simulations suggests that upon re-

lease, the gravity current fluid collapses to some fraction of the initial height i.e. $h_0 \lesssim \frac{1}{2}D$. However, using the above mentioned system of equations, as $h_1'/H \to 1$, $h_0/H \to \frac{1}{2}$ independent of the initial height of the gravity current fluid, D. Correspondingly, the predictions for the speeds u_1 and u_2 are similarly independent of D in this limit. This erroneous prediction occurs because in the limit $h_1'/H \to 1$, $\eta/H \to 0$ and the system of equations reduces to the uniform ambient energy-conserving solution derived by Benjamin (1968) which predicts that $h_0/H = \frac{1}{2}$.

Utilizing equation (2.7), instead, to close the system of equations results in non-physical behaviour when $h_1'/H \to 0$. It is expected that when $h_1' = 0$, $h_1 = 0$. However, the model predicts a non-zero value of h_1 when $h_1' = 0$ and so the mass balance equation, $u_1 h_1 = U h_1'$, can only be satisfied by setting $u_1 = 0$, a physically dubious result. This change in behaviour from the special case of $D = H$ to the more general $D < H$ occurs abruptly as D becomes less than H.

While the predictions for u_1, h_0 and h_1 may be unreliable for both models, the predictions for Fr are surprisingly reasonable for a wide range of parameter space. In the hopes that future researchers deriving a more robust model might benefit from these admittedly imperfect equations, further details of the solutions described above is included in Appendix D.

2.2 Model predictions for full-depth gravity currents

Fig. 2.4 presents examples of model output as determined from the solution of equations (2.5), (2.8) and (2.6). Panels a, c, e indicate, respectively, the variation of h_1, h_2 and h_0 with h_1' for $0 \leq g_{12}'/g_{02}' \leq 1$. Notice, in particular, the following three features: (i) consistent with (2.9), h_2 is a linearly decreasing function whose slope and intercept are independent of the density ratio; (ii) h_1 has as strict upper and lower bounds h_1' and $h_1'/2$ respectively; and (iii)

reminiscent of Benjamin (1968), h_0 has a maximum value of $\frac{1}{2}$, which is obtained when $h_1' = 0$ or $h_1' = 1$. Corresponding velocity profiles are exhibited in Fig. 2.4, panels b, d, f from which two further inferences may be drawn. Firstly,

$$\mathrm{Fr} \equiv \frac{U}{\sqrt{g_{02}' H}} \leq \frac{u_1}{\sqrt{g_{02}' H}} \leq \frac{u_2}{\sqrt{g_{02}' H}}. \tag{2.15}$$

Secondly, Fr is a decreasing function of both h_1' and ρ_1: as the volume or density of intermediate density fluid within the channel increases, the driving force for motion, given by the difference of density between the gravity current and some suitably weighted average ambient density, diminishes. This latter trend is also evident from the upper coloured surface of Fig. 2.5 a, which shows Fr as a function of h_1' and g_{12}'/g_{02}'. From this figure, Fr is observed to show the appropriate limiting behaviour, i.e. $\mathrm{Fr} \to \frac{1}{2}$ when $h_1' \to 0$ or $\rho_1 \to \rho_2$.

Comparable results starting from (2.5), (2.8) with (2.7) rather than (2.6) are exhibited in Fig. 2.6 and Fig. 2.7 a. As suggested by the discussion of §2.1.1, differences between the respective panels of Fig. 2.4 and Fig. 2.6 are relatively small.

An interesting feature of solutions from equations (2.5), (2.8) and (2.6) or (2.7) is that they become degenerate for sufficiently large g_{12}'/g_{02}', a boundary demarcated in Fig. 2.5 a and Fig. 2.7 a by the dotted lines in the h_1'–g_{12}'/g_{02}' planes. Examples of model breakdown in Benjamin-type descriptions of gravity current or intrusion flow are well-documented (see, most recently, Flynn & Linden 2006 and also the discussion of the Holyer & Huppert 1980 solution in §1.2.2), so the appearance of degeneracy here comes as no particular surprise. Insights into this breakdown come from contrasting the gravity current speed with the speed of the interfacial disturbance displayed schematically in Fig. 2.1. Loosely speaking, model breakdown is found to approximately coincide with the transition from a super- to a subcritical gravity current. In the latter case, the interfacial disturbance is able to "outrun" the gravity current and hence the

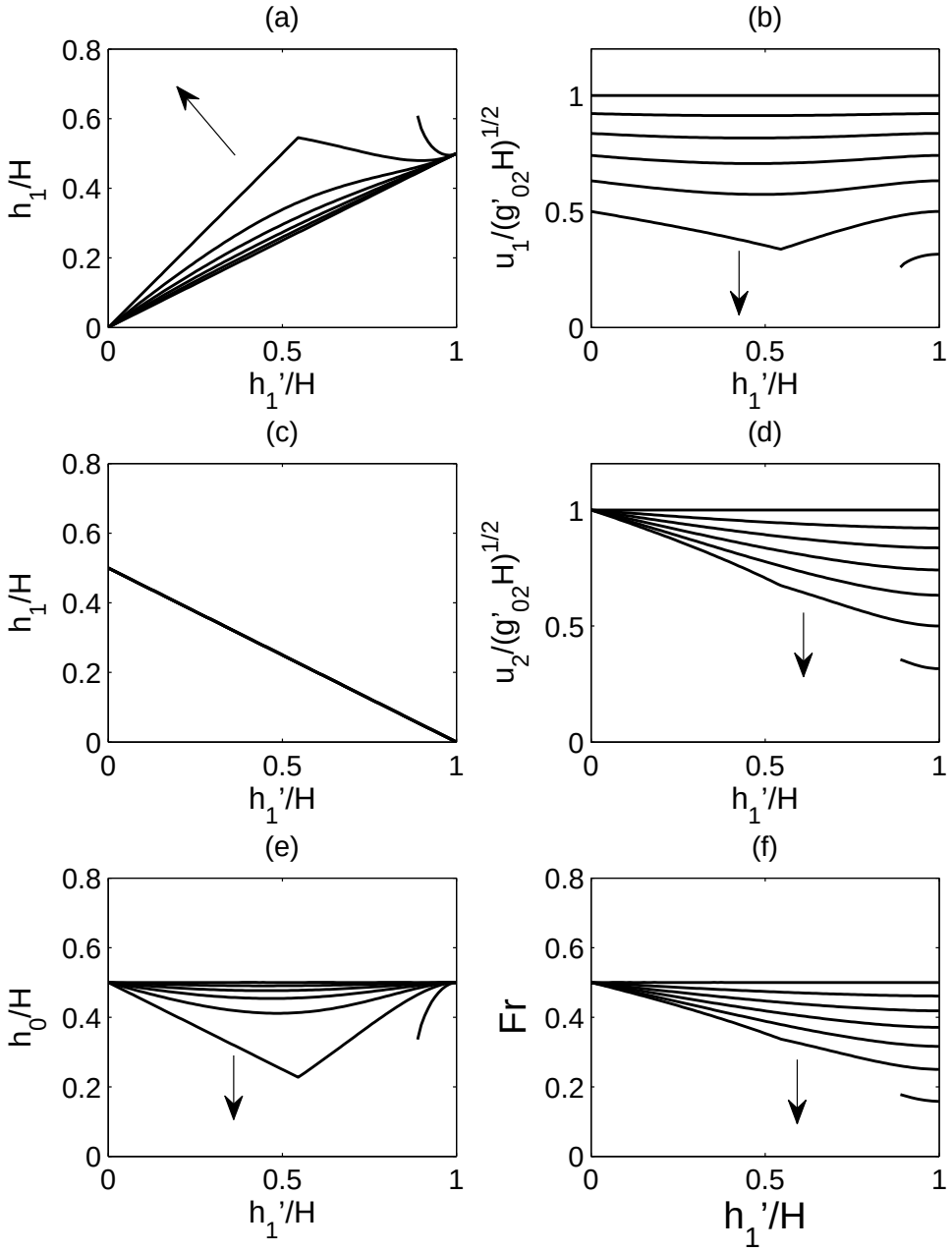

Figure 2.4: Model output based on the solution of (2.5), (2.8) and (2.6). Panels **a, c, e** show, respectively, h_1/H, h_2/H and h_0/H vs. h_1'/H where the associated dimensional lengths are defined in Fig. 2.1. Solutions are drawn for $g_{12}'/g_{02}' =$ 0.15, 0.30, 0.45, 0.60, 0.75 and 0.90; arrows indicate the direction of increasing g_{12}'/g_{02}'. Panels **b, d, f** show, respectively, $u_1/\sqrt{g_{02}'H}$, $u_2/\sqrt{g_{02}'H}$ and $\mathrm{Fr} \equiv U/\sqrt{g_{02}'H}$ vs h_1'. Broken lines for large h_1'/H and g_{12}'/g_{02}' are indicative of model breakdown.

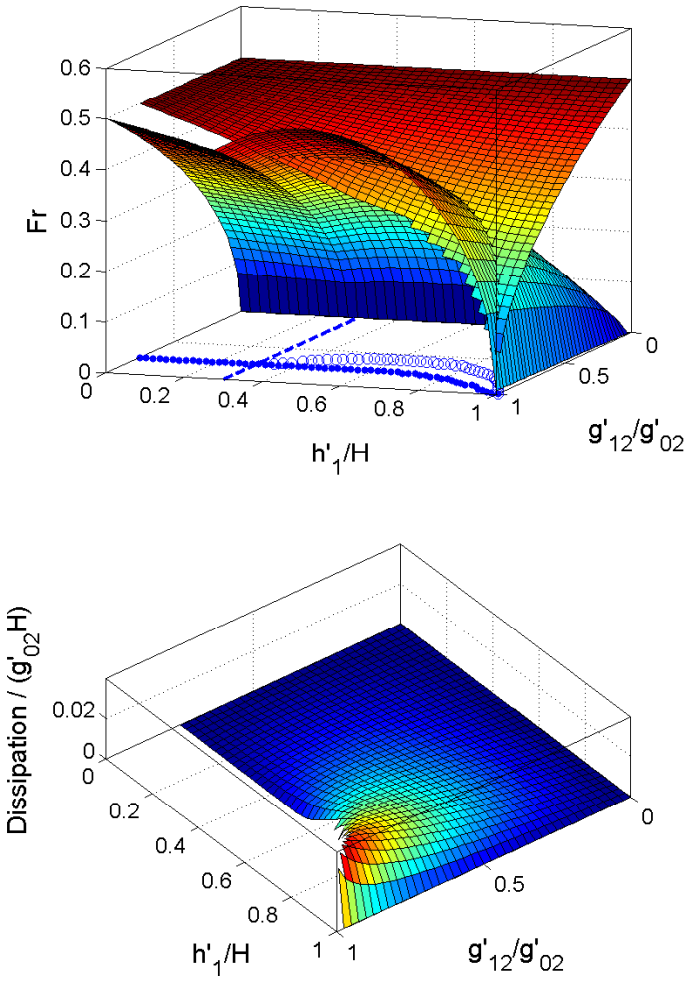

Figure 2.5: **a** Upper surface: non-dimensional gravity current speed, Fr, as defined by (2.2), vs. g'_{12}/g'_{02} and h'_1/H. Results are based upon the solution of equations (2.5), (2.8) and (2.6). Lower surface: composite showing the larger of the long wave speed, given in dimensional form by (2.10), and the Klemp et al. (1997) bore speed, given in dimensional form by (2.11). The dotted and dashed lines are described in text as is the locus of circles. **b** The dissipation function defined by (2.12).

assumption of a steady state flow becomes invalid. Thereafter the interfacial wave evolves into an undular train, strongly reminiscent of the interfacial waves considered by Rottman & Simpson (1989) for the special case where $h'_1 \ll h'_2$.

The lower coloured surfaces of Fig. 2.5 a and Fig. 2.7 a are composite surfaces showing c_{LW} for $h'_1 > 0.299$ and c_B for $h'_1 < 0.299$. To both sides of this

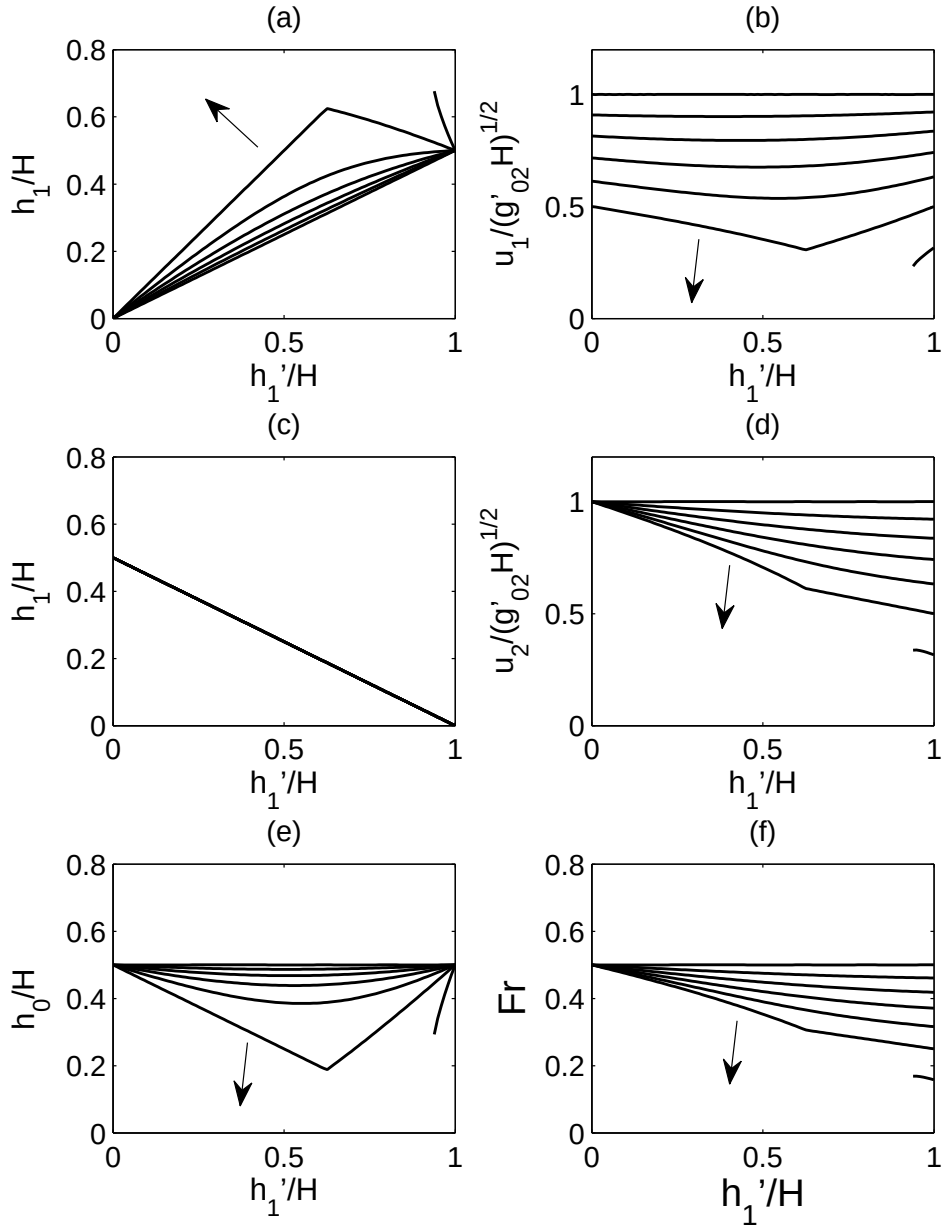

Figure 2.6: As in Fig. 2.4 but showing model results based upon the solution to equations (2.5), (2.8) and (2.7).

divide, denoted in Figs. 2.5 a and Fig. 2.7 a by the dashed lines, the speed of the interfacial disturbance is vanishingly small when $\rho_1 \rightarrow \rho_2$ but grows with increasing interfacial density contrast. By the point at which model breakdown occurs, $c_{LW}/\sqrt{g'_{02}H}$ or $c_B/\sqrt{g'_{02}H}$ is typically close in magnitude to Fr. Plot-

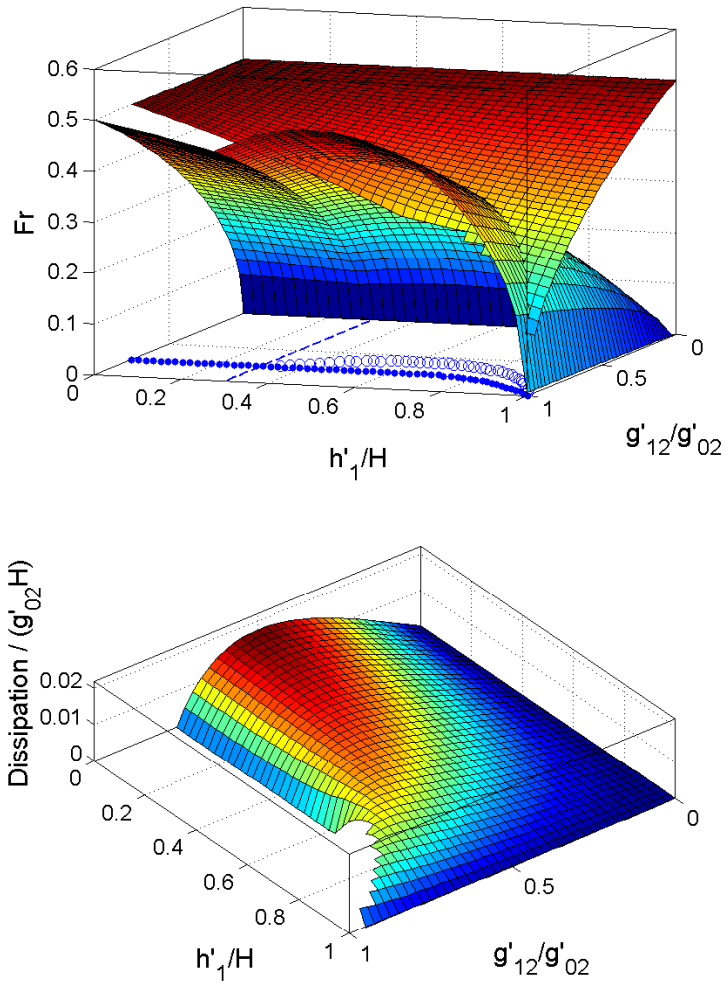

Figure 2.7: As in Fig. 2.5 but showing model results based upon the solutions of equations (2.5), (2.8) and (2.7). The lower panel is based on the solutions to equation (2.13). Note that the lower surface of the upper panel is identical to that of Fig. 2.5.

ted along the g'_{12}/g'_{02}–h'_1 plane of Fig. 2.5 a and 2.7 a are a loci of circles that are points where the gravity current is predicted to be critical with respect to an interfacial long wave or bore. The fact that the loci and dotted lines do not exactly coincide is to be expected: in studying similar flows, Rottman & Simpson (1989) found the existence of a bistable scenario whereby either super- or subcritical (therein termed "partially blocked") regimes may arise depending

on the means of flow initiation.

One may derive an alternative rationale for model breakdown based solely on energetic arguments; such is the purpose of Figs. 2.5 b and 2.7 b which show the predicted non-dimensional dissipation corresponding, respectively, to equations (2.12) and (2.13). Comparison of the two figures reveals a number of interesting disparities, most especially in that the surface of Fig. 2.7 b attains its maximum value when $h_1'/H = 0$ and $g_{12}'/g_{02}' = 0.5$ whereas that of Fig. 2.5 b attains its maximum value when $h_1'/H \simeq 0.95$ and $g_{12}'/g_{02}' \simeq 0.96$. More important than the differences, however, are the similarities in particular that $\Delta R_{A'C'}$, $\Delta R_{OB'} \to 0$ when $g_{12}'/g_{02}' = 3/4$ with $h_1'/H \lesssim 0.5$. Therefore, in order to realize a steady flow with $g_{12}'/g_{02}' > 3/4$ when $h_1'/H \lesssim 0.5$, energy must, in general, be added. In the present configuration, however, there is no such source of energy that would allow such a flow to arise.

Along the boundary of model breakdown, Figs. 2.4 a and 2.6 a show that $h_1 = h_1'$ over non-trivial intervals. For $g_{12}'/g_{02}' > 3/4$, h_1 is predicted to exceed h_1', a circumstance that contradicts our previously stated assumption that the ambient layers of Fig. 2.1 cannot expand in moving from right to left. Thus, consistent with (4.9) of Holyer and Huppert (1980), $\frac{1}{2} \leq h_1/h_1' \leq 1$.

Due to the similarities in the solution when Bernoulli's equation is applied in either the lower or upper ambient layer for the special case where $D = H$, the remainder of the discussion will be focused on results stemming from the former which offers marginally better agreement with our measured results.

Chapter 3

Experiments

To verify the analytical results presented above, in particular the estimate of the front speed made by the model described in §2.1.1, a series of laboratory experiments was performed. Experimental modeling was subsequently extended to two scenarios not easily describable by theory: gravity currents that (i) are subcritical, and, (ii) flow through an ambient with a thick interface.

Experiments were performed in a tempered glass tank measuring 227.5 cm long, 25.0 cm wide and 30.0 cm tall with a watertight acrylic lock gate guided by a pair of sliders mounted at a distance ℓ from the left end wall. Uniform illumination was provided by an Electric Vinyl lightsheet placed behind the tank. Images were recorded at 4 or 8 fps using a pair of 1280 x 1064, 12 bit cameras (LaVision GmbH Imager 3) mounted with 35mm Nikon (AF Nikkor) lenses placed 4.25 m from the front of the tank and 80 cm apart. The calibration factor, required to convert from pixels to cm, was obtained by taking a picture of a 60cm ruler with each camera. As θ, illustrated in Fig. 3.1, was small (6.7°), parallax error was negligible. Therefore, a more complex calibration method was unnecessary.

Fluid densities were measured using an Anton Paar DMA 38 densitometer and are considered accurate to within $0.0005\,\mathrm{g/cm^3}$. For reference, data from experiments described here as well as numerical simulations described in Tan

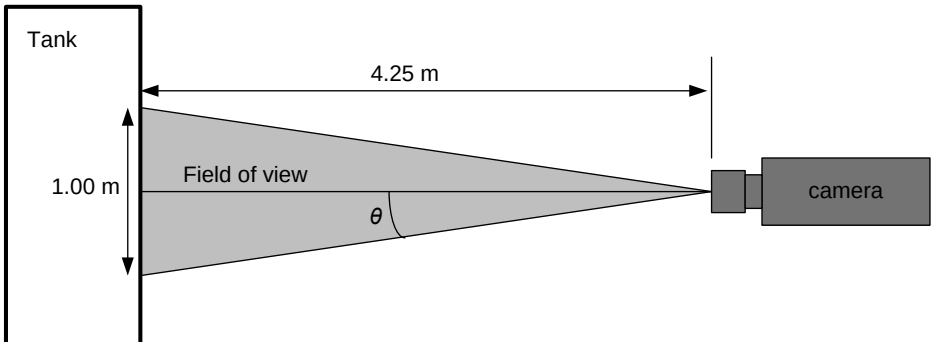

Figure 3.1: Top down schematic diagram of the orientation of the camera with respect to the tank. Lines extending from the camera represent the field of view and θ is as shown in the diagram.

et al. (2010a) can be found in Appendix F.

3.1 Thin interface experiments

When $D = H$, the ambient layers were established by first filling the tank with dyed tap water of density $\rho_2 \simeq 0.9982\,\mathrm{g/cm^3}$ to a height of h_2'. Next, salt water of density ρ_1 was gently added through a foam covered nozzle placed $\sim 4\,\mathrm{mm}$ from the bottom of the tank. When the combined height of both layers reached a depth of H, the flow of salt water was terminated and the lock gate was lowered into the tank. Food colouring and salt water were then mixed into the lock fluid until the density was ρ_0.

When $D < h_1'$, the ambient layers were established as described above. After lowering the lock gate, fluid from the lower layer of the lock region with a density of ρ_1 was drained through a pipe placed at the bottom of the tank. Simultaneously, fluid of density ρ_2 was allowed to flow into the lock without mixing through a pair of small holes in the gate located at heights of approximately 17.5 cm and 20.0 cm[1]. This eliminated a significant difference between the hydrostatic pressures of the lock and ambient regions which might have otherwise caused leakage across the imperfect seals of the lock gate. Siphoning was

[1]The precise locations of the holes are not critical to the process described here.

terminated once the desired volume of fluid had been removed. Salt water of density ρ_0 premixed with dye was then slowly added to the lock region through the foam covered nozzle until the combined height, H, of the fluids on both sides of the lock gate reached the desired value.

When $h_1' \leq D < H$, the ambient layers were established as described above except that the lighter ambient layer of density ρ_2 was filled to a height of $h_2' + \Delta H$. The lock gate was then lowered. Food colouring and salt were then mixed into the lock fluid until the lock fluid density was ρ_0. Fluid was siphoned from the bottom of the lock whilst fluid of density ρ_2 again simultaneously flowed into the lock, this time through the upper small hole only. Siphoning continued until fluid of density ρ_0 spanned a height of D inside the lock.

A small number of experiments where the gravity current propagated along the free surface (i.e. $\rho_0 < \rho_2 < \rho_1$) were also performed in order to investigate the retarding effects of bottom friction on U and the validity of the Boussinesq approximation employed in the derivation of the model. The ambient layers were established as described for the bottom propagating case where $D \geq h_1'$. The lock gate was then lowered and the confined fluid was gradually replaced with fresh water until the lock fluid density reached the desired value.

The experiments began by initiating the image recording and smoothly removing the lock gate once residual motion from mixing the lock fluid had subsided. Representative experimental snapshots are provided in Fig. 3.2, which shows time series images of a super- (LHS) and subcritical (RHS) gravity current and a detailed discussion is presented in §4. The speed of the gravity current, U was measured by evaluating the position of the leading edge of the gravity current through a sequence of images. Two methods were utilized to track the position of the front: (i) manual selection of the leading edge for each image and, (ii) utilizing the built-in Matlab normalized two-dimensional cross-correlation algorithm (`normxcorr2`) which reduced the amount of time, through automa-

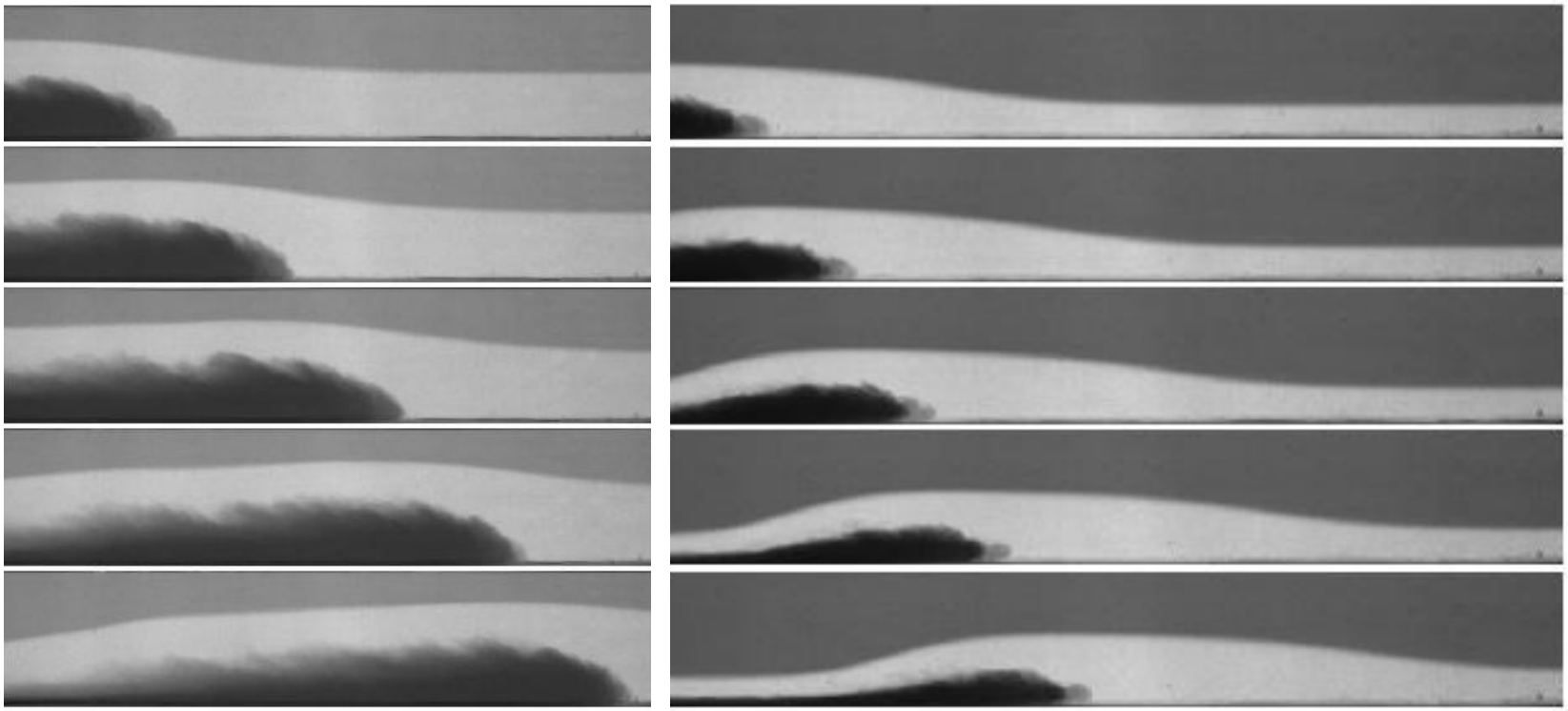

Figure 3.2: (LHS) Time evolution of a supercritical gravity current with $D/H = 1$, $h_1'/H = 0.50 \pm 0.01$, $g_{12}'/g_{02}' = 0.620 \pm 0.045$ and $t^\star \equiv (t/H)\sqrt{g_{02}'H} = 16.9$, 19.6, 22.2, 24.9 and 27.5. The field of view is 99 cm across by 20 cm tall. (RHS) Time evolution of a subcritical gravity current with $D/H = 1$, $h_1'/H = 0.25 \pm 0.01$, $g_{12}'/g_{02}' = 0.878 \pm 0.064$ and $t^\star = 18.7$, 20.5, 22.2, 23.9 and 25.7. The field of view is 101 cm across by 15 cm tall.

tion, required to process the images of an experiment. The horizontal position of which deceleration first begins, X, discussed in §4.5, was obtained by first curve-fitting the linear portion of the front position vs. time plot. The approximate location where the fitted line first deviates from the measured front position is taken to be X.

The amplitude of the interfacial disturbance, η was measured by evaluating the difference in interface heights far downstream and just above the crest of the gravity current head. Image thresholding was applied to minimize subjective biasing errors. Whereas in a select and relatively small subsample of experiments it is observed that η increased slightly as the flow evolved, the increase is modest, i.e. $\lesssim 5\%$ over a window of interrogation that spans approximately 1 m. Given that this behaviour is sporadic rather than systematic, it is assumed to be related to the finite extent of the tank rather than a volume-independent physical effect. The height of the gravity current, h_0 was obtained by measuring the vertical position of the gravity current crest relative to the bottom surface and is averaged through the entire constant speed phase. However, due to the turbulent structures behind the front, this parameter is difficult to measure and thus has a large uncertainty range. Once h_0 and η are known, h_1 and h_2 can be straightforwardly calculated. The initial height of the gravity current fluid, D, was measured prior to the initiation of the experiment using a conductivity probe (Precision and Measurement Engineering, MSCTI) which was mounted to a computer controlled traverse (Velmex, X-Slide). The relationship between voltage and density is linear and was verified using stock solutions of known density.

In these experiments, ρ_1 ranged from $0.9987\,\mathrm{g/cm^3}$ to $1.0446\,\mathrm{g/cm^3}$, ρ_0 ranged from $1.0200\,\mathrm{g/cm^3}$ to $1.0962\,\mathrm{g/cm^3}$. The following combinations of channel depth and lock length were employed: $H = 20 \pm 0.1$ cm when $\ell = 32.4 \pm 0.1$ cm and $H = 15 \pm 0.1$ cm when $\ell = 16.5 \pm 0.1$ cm. The latter combination proved

especially valuable in visualizing instances where the gravity current head was overtaken by the interfacial disturbance.

Three separate experiments were conducted at lower Reynolds number (i.e Re $\equiv UH/(2\nu) \simeq 5 - 6 \times 10^3$ vs. Re $\simeq 7 - 8 \times 10^3$), mimicking more closely the numerical simulations described in Tan et al. (2010a). For these experiments, $\rho_1 \simeq 1.0150\,\mathrm{g/cm^3}$, $\rho_0 \simeq 1.0205\,\mathrm{g/cm^3}$, $H = 20\,\mathrm{cm}$ and $\ell = 34.0\,\mathrm{cm}$.

Fig. 3.3 shows timeseries images of a surface propagating supercritical gravity current with $D/H = 1$, $h_1' = 0.75 \pm 0.01$ and $g_{12}'/g_{02}' = 0.755 \pm 0.069$. Notice that the subcritical gravity current shown in this figure is essentially a mirror image of the bottom-propagating "heavy" gravity currents shown in Fig. 3.2. This similarity attests to the validity of the Boussinesq approximation applied in §2.1.1.

3.2 Thick interface experiments

In a second laboratory investigation, the interface position was fixed at $H/2$ and $D/H = 1$ but the interface thickness, δ, was systematically varied. Several methods were employed in obtaining a diffuse interface. Firstly, the tank was filled to a depth of h_2' with fresh water of density ρ_2. Salt water of density ρ_1 was then carefully added to the tank, which was subsequently left undisturbed for up to $\sim$12 h over which time the interface broadened by molecular diffusion. In a second method, the tank was filled to a depth of $h_2 - \delta/2$ with water of density ρ_2 after which salt water of gradually increasing density was added up to a depth of $h_2' + \delta/2$. Thereafter, salt water of density ρ_1 was added until the desired total channel depth of H was obtained. Thirdly, a standard lock-exchange experiment of the type shown in Fig. 2 a of Shin et al. (2004) was conducted with the lock gate placed at the approximate midpoint of the tank. As a result of the mixing associated with the counter-flowing upper and lower gravity currents, the quiescent steady state consisted of upper and lower

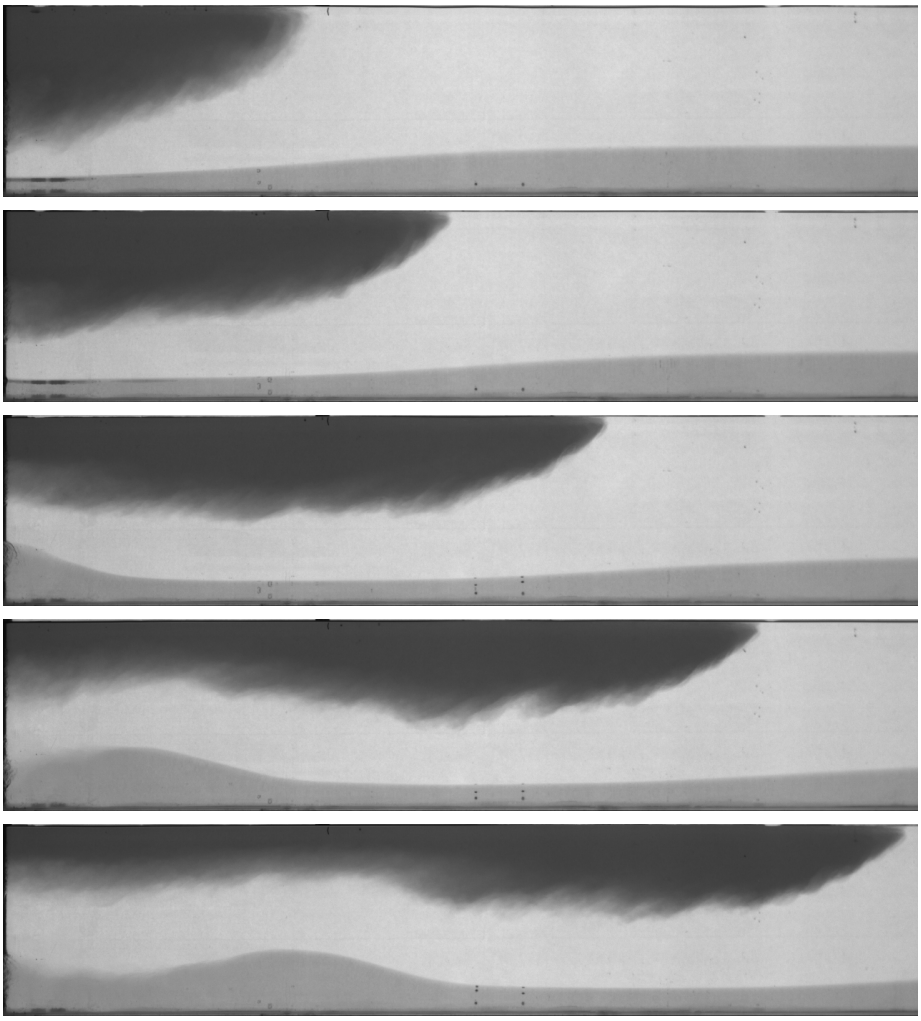

Figure 3.3: Time evolution of a surface-propagating supercritical gravity current with $D/H = 1$, $h_1' = 0.75 \pm 0.01$, $g_{12}'/g_{02}' = 0.755 \pm 0.069$, and $t^\star = 5.4$, 8.0, 10.7, 13.4 and 16.1. The field of view is 101 cm across by 20 cm tall.

layers of densities ρ_2 and ρ_1, respectively, with an intervening thick interface that was approximately 4cm thick. Finally, the tank was filled from top to bottom with uniformly stratified salt water using a variation of the Oster (1965) double bucket technique. In all cases, density profiles were measured using the conductivity probe. A sample density profile can be found in Appendix C. For

non-zero values of δ, measurements of η are based on the average elevation of the (thick) interface.

3.3 Error Analysis

3.3.1 Discussion on experimental error

Errors in the experimental results arose from several sources. The first major source of error were those that were caused by the experimental setup. For example, (1) non-uniformity of the saline solutions due to incomplete mixing that could lead to incorrect density readings, (2) inadequate seals of the lock gate that resulted in fluid leakage which would alter the density and initial height of the fluids, and (3) imperfections in the ambient stratification (e.g. non-linearities in the interface region for thick interface experiments) which could affect the dynamics of the flow.

Errors also originated from the measuring equipment (e.g. densitometer, conductivity probe, ruler) which each have their associated uncertainties. Additionally, the measurement of the calibration factor was performed with that assumption that parallax errors are small. However, these errors were still present and had a minor affect on accuracy of the measurements. Finally, the most significant sources of error are those that occur during the measurement of parameters (e.g. U, η, X) in matlab. For example, to measure the interfacial amplitude, η, the position of the interface far upstream and just above the crest of the gravity current head was selected. This procedure was further complicated by the fact that the interface was relatively thick, resulting in a subjective measurement that could vary from person to person. As a further example, measurements of U requires a selection of an interval within the linear portion of the front position vs. time plot in order to perform a curve fit. Depending on the size of this interval, U would vary slightly.

3.3.2 Sample error calculation

Representative error bars are shown in each figure presenting experimental results. A sample calculating of the error, taking h_1'/H as an example, is as follows:

$$\begin{aligned} \mathrm{d}\left(\frac{h_1'}{H}\right) &= \frac{\mathrm{d}h_1' H + (-\mathrm{d}H)h_1'}{H^2} \\ &= \frac{\mathrm{d}h_1'}{H} + \frac{(-\mathrm{d}H)h_1'}{H^2} \end{aligned} \tag{3.1}$$

where $\mathrm{d}h_1'$ and $\mathrm{d}H$ are errors associated with h_1' and H, respectively. Taking the worst case scenario, i.e. both errors do not cancel out, (3.1) can be written as:

$$\mathrm{d}\left(\frac{h_1'}{H}\right) = \frac{\mathrm{d}h_1'}{H} + \frac{(\mathrm{d}H)h_1'}{H^2} \tag{3.2}$$

The representative error bars are calculated by averaging the error associated with each experimental data point shown in the figure.

Chapter 4

Results and discussion

4.1 Comparison between numerical and experimental results

Fig. 4.1 contrasts snapshot images of experimental (panels a & c) and numerical (panels b & d) data. In panels a and b, $h_1'/H = 0.38 \pm 0.01$, $D/H = 0.45 \pm 0.02$, $g_{12}'/g_{02}' = 0.746 \pm 0.047$. Images are shown at $t^\star = 3.37$; 6.73 and 10.10 where the non-dimensional time is defined by

$$t^\star = \frac{t}{H}\sqrt{g_{02}' H}. \tag{4.1}$$

Conversely in panels c and d, $h_1'/H = 0.25 \pm 0.01$, $D/H = 0.72 \pm 0.02$, $g_{12}'/g_{02}' = 0.511 \pm 0.045$; images are shown at $t^\star = 4.83$; 11.28 and 17.72. In both cases, fluid densities in the numerical simulations are chosen to match those from the analogue experimental runs. The correlation between image pairs is satisfactory: in each case, generally strong agreement is noted when comparing the front position and interfacial wave structure. As the Direct Numerical Simulation (DNS) algorithm used to generate the numerical simulations is two-dimensional, one observes in the numerical images more pronounced vortices in the lee of the gravity current front. By comparison, these vortices are rapidly broken down by spanwise instabilities in the real three-dimensional flow. Correspondingly, a series of abrupt deflections to the ambient interface well behind the gravity current head is observed, particularly in Fig. 4.1 d, which are not

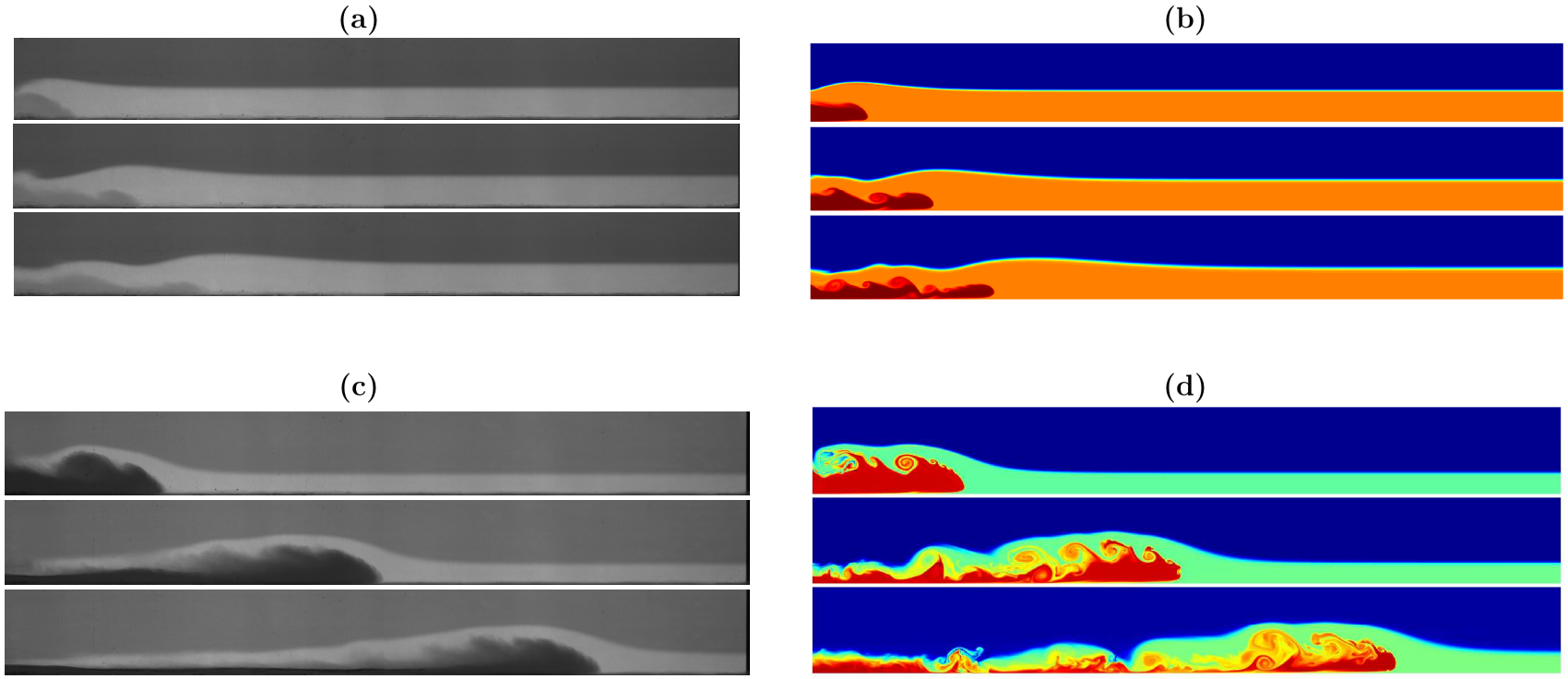

Figure 4.1: (TOP ROW): Time evolution images with $h_1'/H = 0.38 \pm 0.01$, $D/H = 0.45 \pm 0.018$ and $g_{12}'/g_{02}' = 0.746 \pm 0.047$ at $t^\star \equiv (t/H)\sqrt{g_{02}'H} = 3.37, 6.73$ and 10.10. The field of view is 176 cm across by 20 cm tall. (BOTTOM ROW): Time evolution images with $h_1'/H = 0.25 \pm 0.01$, $D/H = 0.72 \pm 0.020$ and $g_{12}'/g_{02}' = 0.511 \pm 0.045$ at $t^\star = 4.83, 11.28$ and 17.72. The field of view is 178 cm across by 20 cm tall. Panels **a** and **c** are experimental images while panels **b** and **d** are numerical simulations. The latter are performed using the algorithm summarized in §4 of Tan et al. (2010a).

evident in the experimental images of Fig. 4.1 c. Fortunately, given the aims of the present investigation, such observations are unimportant since the front speed, U, is unaffected by the coherence of the trailing vortices (Cantero et al. 2007) and their associated deflections to the ambient interface.

4.2 Comparison of theoretical predictions and measured results for full depth gravity currents

One of the principal assumptions applied in the development of the analytical model of §2.1.1 is quantified by the dimensional equation (2.8), which anticipates a linear variation of η upon h_1'. A test of this assumption employing both experimental and numerical data is given in Fig. 4.2. Generally, the fit between measurement and theory is found to be satisfactory. In particular, and consistent with (2.8), observations of Fig. 4.2 show relatively little variation of the amplitude of the interfacial disturbance with the density ratio for $0.125 \leq g_{12}'/g_{02}' \leq 0.762$. The largest deviations are noted when h_1' and g_{12}'/g_{02}' are both small. This is to be expected because (i) the interfacial density jump is, in this case, relatively small so that large amplitude, transient distortions may be easily generated and (ii) with a thin lower layer, it is often difficult to distinguish between ambient and gravity current fluid. The positive agreement observed in Fig. 4.2 a is further reinforced by the favorable comparison between theory and experiment exhibited in Fig. 4.3. It shows h_1, h_2 and h_0 as a function of h_1' for a particular density ratio. Numerical results are omitted from Fig. 4.3 because the algorithm of §4 in Tan et al. (2010a) is two-dimensional: spanwise instabilities cannot develop so that whatever billows develop along interface OB' from Fig. 2.1 remain coherent and large in scale (Härtel et al. 1999 and Fig. 4.1). This in turn complicates the measurement of h_0 and h_1.

Fig. 4.4 a-c show the variation of Fr with g_{12}'/g_{02}' for $h_1' = 0.25$, 0.50 and 0.75,

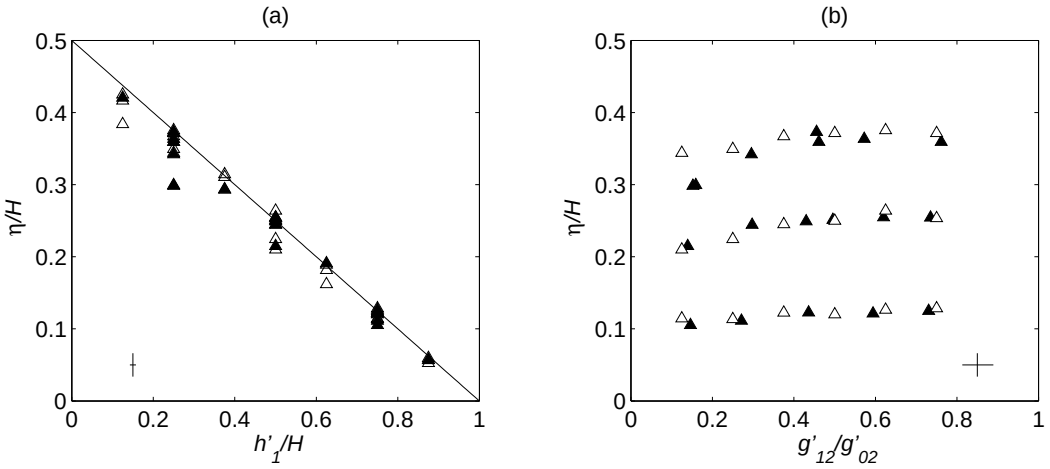

Figure 4.2: (a) Non-dimensional amplitude, η/H, of the interfacial disturbance versus the non-dimensional ambient lower layer depth, h_1'/H. *Open* and *solid triangles* show, respectively, numerical and experimental results whereas the solid line shows the hypothesized correlation of (2.8). (b) η/H versus the density ratio g_{12}'/g_{02}' for $h_1'/H = 0.25$ (*upper row* of data points), $h_1'/H = 0.50$ (*middle row*) and $h_1'/H = 0.75$ (*lower row*). Representative error bars are located on the bottom left (panel a) and bottom right (panel b).

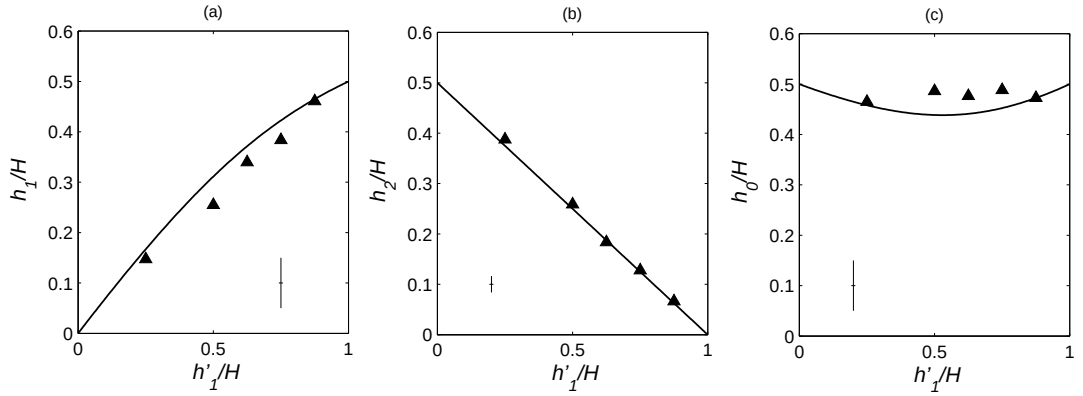

Figure 4.3: Non-dimensional layer depths as a function of h_1'/H for $g_{12}'/g_{02}' \simeq 0.45$. Theoretical curves are based upon the solution of equations (2.5), (2.8) and (2.6); experimental data points are shown by the *solid triangles*. Representative error bars are as indicated.

respectively. Theoretical results are indicated by the solid curves. Consistent with Fig. 4.3, these are extracted from the upper surface of Fig. 2.5 a and extend up until $g_{12}'/g_{02}' \simeq 0.75$. Experimental and numerical results are indicated, respectively, by the solid triangles/stars and the open triangles. Although the

latter under-predict the former, the deviation is small, i.e. within experimental error. There is a more notable discrepancy between theory and measurements, which reflects the influence of drag forces, chief among them bottom friction (Härtel et al. 1999), that are not accounted for in the model of §2.1.1.

The open circles in Fig. 4.4 c show experimental data from gravity currents propagating along the free surface. The measured speeds of the data points at $g'_{12}/g'_{02} \simeq 0.25$ are observed to be greater than the bottom-propagating experiments which attests to the effects of bottom friction. Additionally, repeated experiments show greater amount of variability. This behaviour is postulated to be caused by the bottom-up removal of the lock gate which interacted with the lighter gravity current fluid as it rose, perturbing the initial conditions. When $g'_{12}/g'_{02} \simeq 0.25$, the model under-predicts the measured results which is unusual but not necessarily unphysical. Unlike the energy-conserving Benjamin solution for gravity currents in a uniform ambient, dissipation is allowed to occur by requiring that energy be conserved in only one of the ambient layers.

Our results are consistent with those from several earlier investigations as indicated by Fig. 4.4 d, which shows measured values of Fr versus the Reynolds number, $\mathrm{Re} = UH/(2\nu)$, in the limit $g'_{12}/g'_{02} \to 0$. Included therein is data from the present analysis (triangles) and also the studies of Lowe et al. (2004)–solid circles; Härtel et al. (1999)–stars; and Keulegan (1957)–open squares. In all cases measured values are within 16% of Benjamin's energy-conserving prediction of $\frac{1}{2}$.

Notwithstanding the aforementioned offset between theory and measurement, strong qualitative agreement is observed between the solid curves and the data points of Fig. 4.4. In particular whereas Fr is predicted to decrease with g'_{12}/g'_{02} in all three panels, the model of §2.1.1 accurately captures the higher sensitivity of Fr to g'_{12}/g'_{02} as h'_1 is increased.

An additional intriguing feature of the analytical model is its breakdown at

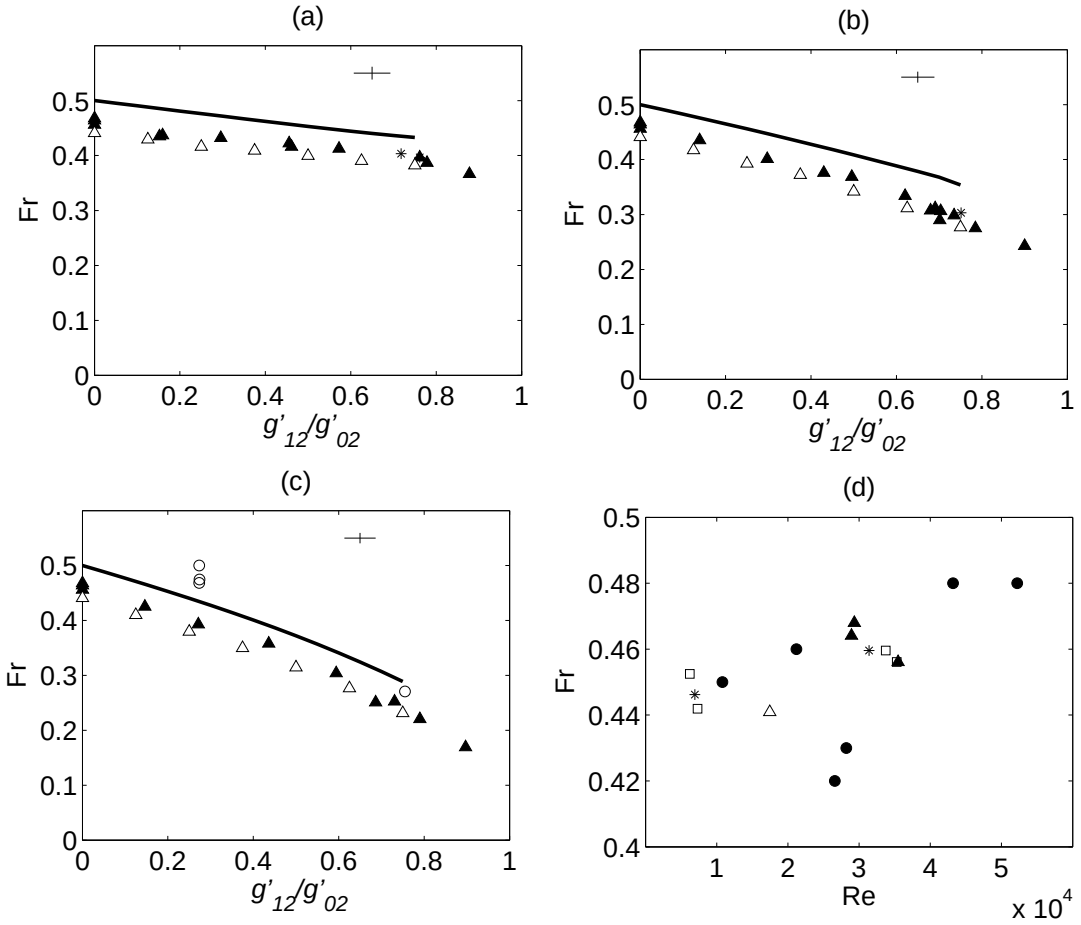

Figure 4.4: Fr, as defined by (2.2), vs. g'_{12}/g'_{02} for a $h'_1/H = 0.25$, (b) $h'_1/H = 0.50$ and (c) $h'_1/H = 0.75$. Data points are as follows: *open triangles*–numerical results; *solid triangles*–high-Re experimental results; *stars*–low-Re experimental results. The solid curve gives the corresponding theoretical result. Representative error bars for the experimental data are as indicated. *Open circles* in panel (c) show experimental data of a gravity current propagating along the free surface. Panel (d) shows the variation of Fr with Re for the limiting case where $g'_{12}/g'_{02} = 0$; data points are defined in the text.

large values of g'_{12}/g'_{02}. Reasons for model breakdown are discussed in §2.2 where it is suggested that the boundary located at sufficiently large values of g'_{12}/g'_{02} approximately delineates between the supercritical and subcritical regimes. Whereas flow behaviour in the immediate parametric neighborhood of the boundary is difficult to classify, laboratory evidence that supports the interpretation discussed above is presented in Fig. 3.2. The LHS panels of Fig. 3.2 show a supercritical gravity current with $D = H$, $h'_1/H = 0.50 \pm 0.01$ and $g'_{12}/g'_{02} = 0.620 \pm 0.045$. Over the indicated time interval, the gravity current front and interfacial disturbance are observed to propagate at the same speed. It is not until the gravity current begins to decelerate that the interfacial disturbance is able to overtake the front. A qualitatively different picture is painted by the RHS panels of Fig. 3.2, which consider a gravity current with $D = H$, $h'_1/H = 0.25 \pm 0.01$ and $g'_{12}/g'_{02} = 0.878 \pm 0.064$. Here, the front speed is again constant over the indicated time interval, but the interfacial disturbance propagates ahead of the gravity current with a speed that is approximately 20% larger than U.

4.3 Partial depth gravity currents

An important component in the attempt to extend the model of §2.1.1 to the more general case where $D < H$ is (2.14) which generalizes the parameterization for the interfacial disturbance to account for the geometric variable D. A careful comparison with experiments was performed in order to ensure the validity of this equation. Fig. 4.5 a, b are surface plots of η/H vs. D/H and h'_1/H. A qualitative comparison of the two surface plots, where the upper panel is the solution to (2.14) and the lower panel was generated using interpolated experimental results, show promising agreement. On the η/H–h'_1/H plane of the lower panel, the circles, right facing triangles and diamonds represent experimental data points and solid lines are solutions to (2.14) for various D/H.

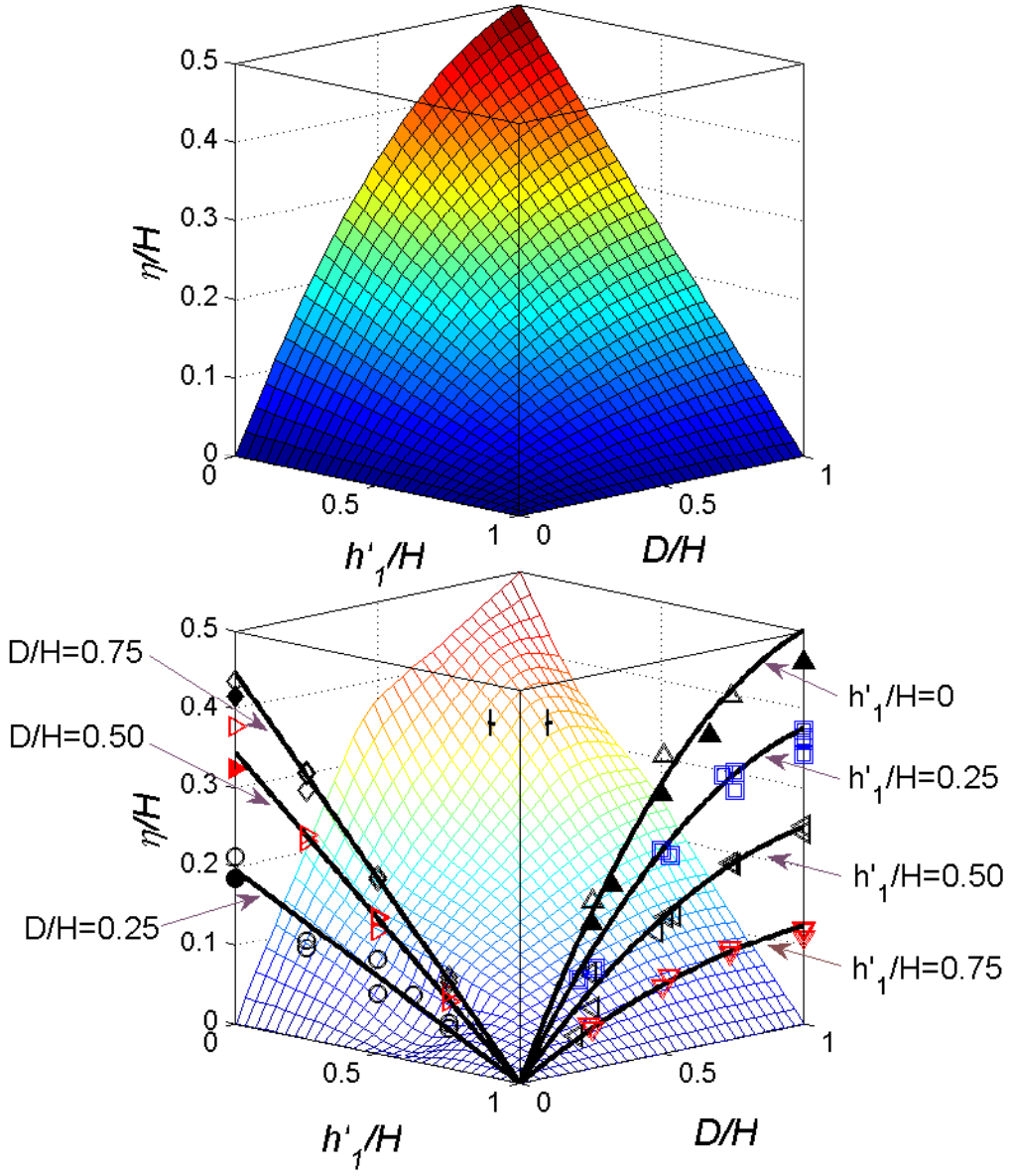

Figure 4.5: Surface plots of the non-dimensional wave amplitude, η/H versus the non-dimensional lower ambient layer height, h_1'/H, and the non-dimensional height of the lock fluid, D/H. **Upper Panel:** Solution to (2.14). **Lower Panel:** Surface plot generated from interpolated experimental data. On the $\eta/H - h_1'/H$ plane, *circles, right facing triangles* and *diamonds* are experimental data points for D/H =0.25, 0.50 and 0.75, respectively. The *solid* lines are the solutions to (2.14) for various D/H. On the $\eta/H - D/H$ plane, *downward facing triangles, left facing triangles, squares* and *upward facing triangles* are experimental data for $h_1'/H = 0.75$, 0.50, 0.25 and 0 respectively. The *solid* lines are the solutions to (2.14) for various h_1'/H. In both of the above mentioned planes, solid markers represent data taken from Rottman and Simpson (1983). Representative error bars are as indicated.

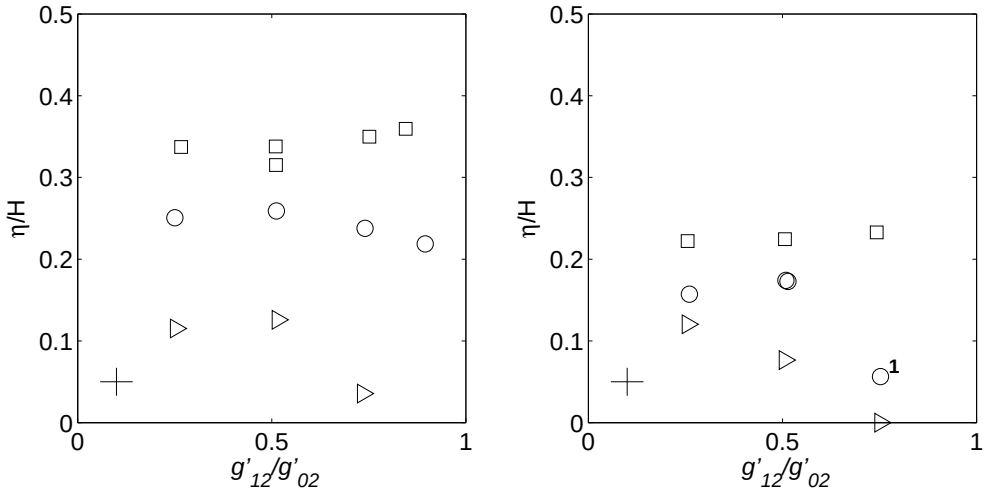

Figure 4.6: Non-dimensional wave amplitude, η/H versus density ratio, g'_{12}/g'_{02}. **LHS** Experimental results with $h'_1/H = 0.25 \pm 0.01$, $D/H = 0.239 \pm 0.017$ *(rightward facing triangles)*, $D/H = 0.519 \pm 0.019$ *(circles)* and $D/H = 0.749 \pm 0.021$ *(squares)*. **RHS**: Experimental results with $h'_1/H = 0.50 \pm 0.01$, $D/H = 0.230 \pm 0.017$ *(rightward facing triangles)*, $D/H = 0.491 \pm 0.019$ *(circles)* and $D/H = 0.743 \pm 0.021$ *(squares)*. Representative error bars are as indicated. A timeseries snapshot of the data point demarkated by "1" is given in Fig. 4.7.

The agreement between prediction and measurement is generally within experimental error. On the η/H–D/H plane, the downward facing triangles, left facing triangles, squares and upward facing triangles are experimental data and the solid lines are solutions to (2.14) for various h'_1/H. In this comparison, the level of agreement is satisfactory except for low values of D/H where the theory tends to over-predict the experimental results. In general, as will be shown in Fig. 4.12 d, deceleration of the gravity current is observed to occur sooner as D/H becomes smaller. The lower values of η/H may reflect the fact that the gravity current begins to decelerate before the interfacial disturbance has the chance to develop fully.

An additional component of equation (2.14) is the prediction that η/H is independent of the density ratio, g'_{12}/g'_{02}. Fig. 4.6 depicts the variation of η/H with g'_{12}/g'_{02}. The LHS panel shows experimental results with $h'_1/H = 0.25 \pm 0.01$, $D/H = 0.239 \pm 0.017$ (rightward facing triangles), $D/H = 0.519 \pm 0.019$

(circles) and $D/H = 0.749 \pm 0.021$ (squares). The RHS panel shows experimental results with $h_1'/H = 0.50 \pm 0.01$, $D/H = 0.230 \pm 0.017$ (rightward facing triangles), $D/H = 0.0.491 \pm 0.019$ (circles) and $D/H = 0.743 \pm 0.021$ (squares). The results show that the approximation is satisfactory except at high g_{12}'/g_{02}' with low D/H. As discussed by Tan et al. (2010a, b), deceleration of the gravity current front occurs sooner as g_{12}'/g_{02}' increases. This, coupled with the effects of low D/H on deceleration, results in the observed decreasing trend. Fig. 4.7 shows timeseries images of the experiment defined in Fig. 4.6 by the number "1" where deceleration occurs at < 1 lock length, in contrast to the 3-10 lock lengths previously observed for partial depth gravity currents in a uniform ambient (Fig. 11 of Rottman & Simpson 1983). Correspondingly, the amplitude of the interfacial disturbance remains underdeveloped. A different result will not be obtained when using a longer lock length as the front will still be very quickly overtaken by the interfacial wave.

Fig. 4.8 shows the variation of Fr due to h_1'/H with the top, middle and bottom rows corresponding to $g_{12}'/g_{02}' = 0.25$, 0.50 and 0.75, respectively. Columns (i), (ii), (iii) and (iv) correspond to $D/H = 0.25$, 0.50, 0.75 and 1.00, respectively. The solid curves of column (iv) represent the solution to (2.5), (2.6) and (2.8). The dashed curves represent a composite curve of the larger of the long wave and internal bore speeds quantified by equations (2.10) and (2.11), respectively, with η defined as (2.14). Experimental and numerical data are depicted by circles and triangles, respectively. The measured results in column (iv) are identical to the ones in Fig. 4.4 and thus show similarly good agreement with the exception of an offset caused primarily by bottom friction. A monotonic and nonlinear decrease of Fr with decreasing D/H is observed. This is consistent with previous studies (Huppert & Simpson 1980, Rottman & Simpson 1983) where measurements of the speed of a full depth lock release gravity current in a uniform ambient are closest to Benjamin's energy conserving solution of Fr

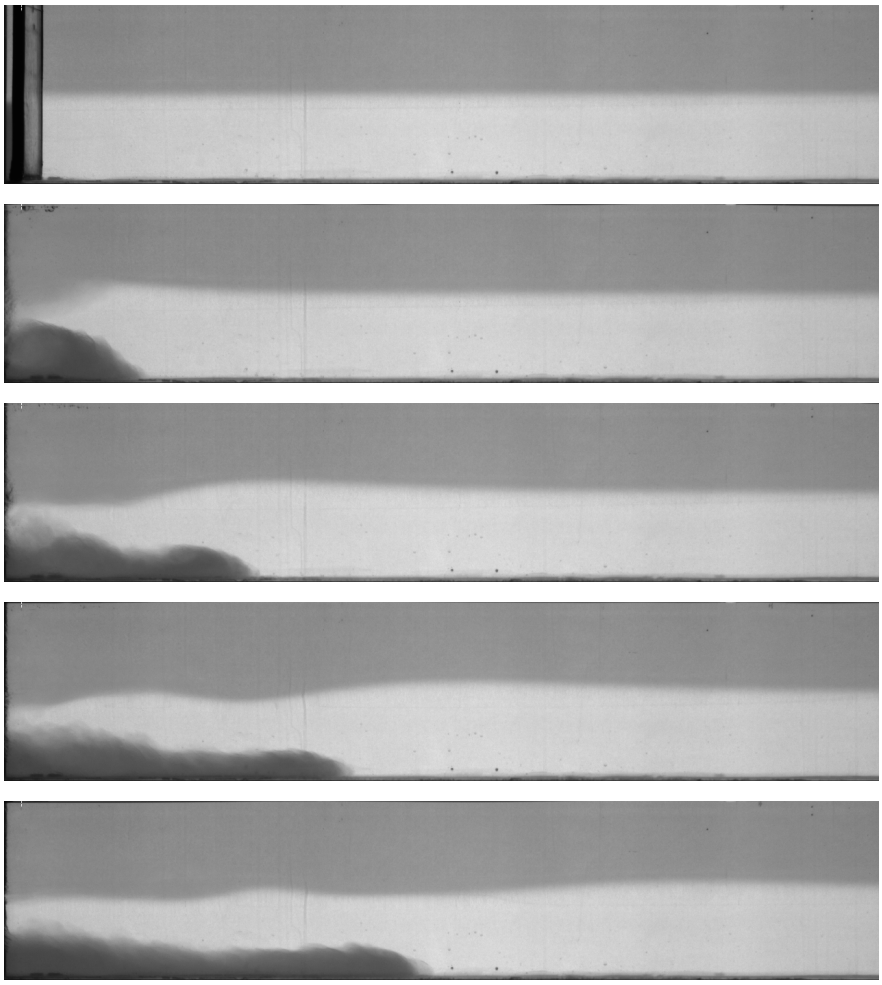

Figure 4.7: Time evolution of a subcritical gravity current with $D/H = 0.470 \pm 0.019$, $h_1' = 0.50 \pm 0.01$, $g_{12}'/g_{02}' = 0.752 \pm 0.064$, and $t^\star \equiv (t/H)/\sqrt{g_{02}'H} = 0.0$, 3.5, 7.1, 10.6 and 14.1. The field of view is 101 cm across by 20 cm tall.

$= \frac{1}{2}$ when $D/H = 1$. This is to be expected because the amount of initially available potential energy, which is then converted to kinetic energy once the flow is initiated, is at a maximum when $D/H = 1$. Smaller values of D have less initial potential energy and are consequently slower. While our theory only applies for the special case where $D/H = 1$, the agreement is observed to be surprisingly satisfactory for D/H as low as approximately 0.5.

A higher Reynolds number experiment was performed in order to investigate

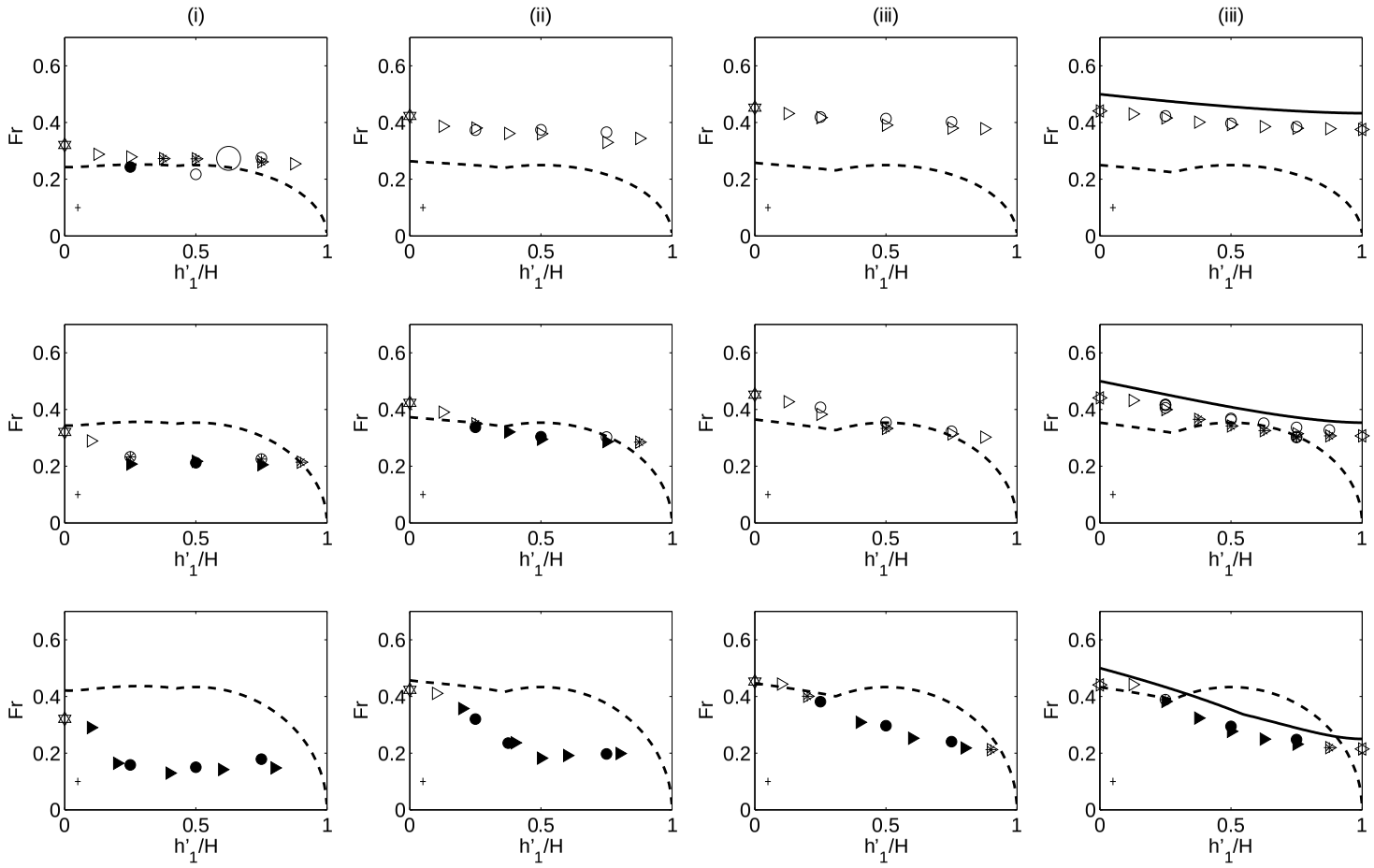

Figure 4.8: Fr vs. h_1'/H for $D/H = 0.25$ (column i), $D/H = 0.50$ (column ii), $D/H = 0.75$ (column iii), and $D/H = 1$ (column iv). The top, middle, and bottom row show solutions for $g_{12}'/g_{02}' = 0.25$, 0.50 and 0.75, respectively. The solid lines in column (iv) show the solutions to (2.5), (2.6) and (2.8). The dotted lines are composite curves showing the larger of the wave amplitude speed given in (2.10) and the bore speed given in (2.11), where η is defined in (2.14). Experimental data (*circles*) and numerical simulations (*right facing triangles*) are also shown. Open and solid markers represent supercritical and subcritical gravity currents, respectively. Open markers with a star represent in-between cases. 6-pointed star markers represent uniform ambient experiments. The larger circle in the upper left hand panel corresponds to a high Re experimental run. Representative experimental error bars are as indicated.

the possibility that the lower values of Fr was caused by viscous effects. This experiment, represented by the large circle in the *Top Row–(i)* panel of Fig. 4.8, was performed at a higher Reynolds number of Re$\equiv UD/\nu = 6085$ compared to the Re $\simeq$ 3680 of other experiments with similar D/H and g'_{12}/g'_{02}. The difference of Fr was found to be negligible within experimental error. Another observation that discouraged this line of reasoning is that numerical runs were performed at lower Reynolds number (e.g. average Re=2686 for simulations with $D/H = 0.25$ and $g'_{12}/g_{02} = 0.250$) but show negligible difference, within experimental error, when compared with analogue laboratory results.

In Fig. 4.8, subcritical gravity currents, where the interfacial disturbance was seen to propagate ahead of the front, are represented by solid markers. Supercritical gravity currents, where the interfacial disturbance was seen to remain attached to the front, are represented by open markers. In between cases are represented by open markers with a star. As discussed in §2.2, when Fr>max(c_{LW}, c_B) the interfacial disturbance is expected to remain attached to the gravity current front and is therefore supercritical. In the converse scenario, when Fr<max(c_{LW}, c_B), the interfacial disturbance propagates away from the front and the flow is therefore subcritical. As shown in Fig. 4.8, markers that fall below the dashed curves, which represent max(c_{LW}, c_B), are typically solid while those that lie above the curves are typically open.

4.4 Thick interface results

One of the defining characteristics of an intrusive gravity current propagating in a two-layer stratified medium is that the initial front speed decreases as the thickness, δ, of the ambient interface increases (Faust & Plate 1984, Sutherland & Nault 2007). To assess the impact of the interfacial thickness for the flow depicted schematically in Fig. 2.1, a series of laboratory experiments were performed as outlined above. Results from this analysis are depicted in Fig. 4.9 a

and b. They show, as a function of δ/H the normalized front speed, expressed as

$$\frac{\mathrm{Fr}}{A} = \frac{\mathrm{Fr}}{\sqrt{1-(3/4)\times(g'_{12}/g'_{02})}}. \tag{4.2}$$

The normalization factor A is motivated by equation (14.24) of Ungarish (2009) and serves to substantially reduce the variation between experiments run at different density ratios. Fig. 4.9 a and b consider, respectively, super- and sub-critical gravity currents.

In sharp contrast to the experimental observations of Faust and Plate (1984), it is seen from Fig. 4.9 a that the speed of a supercritical gravity current is essentially independent of the interface thickness, at least within experimental error. This result is to be expected when $\delta/H \ll 1$: the theory of §2.1.1 predicts U to be a function of the depth-integrated pressure, $\int p\,\mathrm{d}z$, whose magnitude is unaltered by interfacial diffusion in the ambient. The fact that the front speed remains constant even as $\delta/H \to 1$ is surprising, however. In these cases, the smearing of density is not confined solely to the neighborhood of the interface. Rather there is a pronounced vertical variation in the density of the ambient fluid immediately adjacent to the (advancing) gravity current.

Also included in Fig. 4.9 a are three theoretical solutions. These apply in the limiting case of a uniformly stratified ambient (i.e. $\delta/H \to 1$) and are based on the analysis summarized in Chap. 14 of Ungarish (2009). In ascending order and consistent with the experimental data, the theoretical solutions, given in Fig. 4.9 a by the horizontal lines, correspond to $g'_{12}/g'_{02} = 0.230$, 0.499 and 0.672. Consistent with Fig. 4.4, theory moderately over-predicts measured results; bottom friction is again believed to be responsible for the discrepancy. As a further check on the consistency of our measured data, results from the study of Maxworthy et al. (2002) who similarly considered gravity currents in a uniformly stratified ambient (see §1.2.1) are included along the RHS axis of Fig. 4.9 a. The solid data points of Fig. 4.9 a correspond to the solution of their

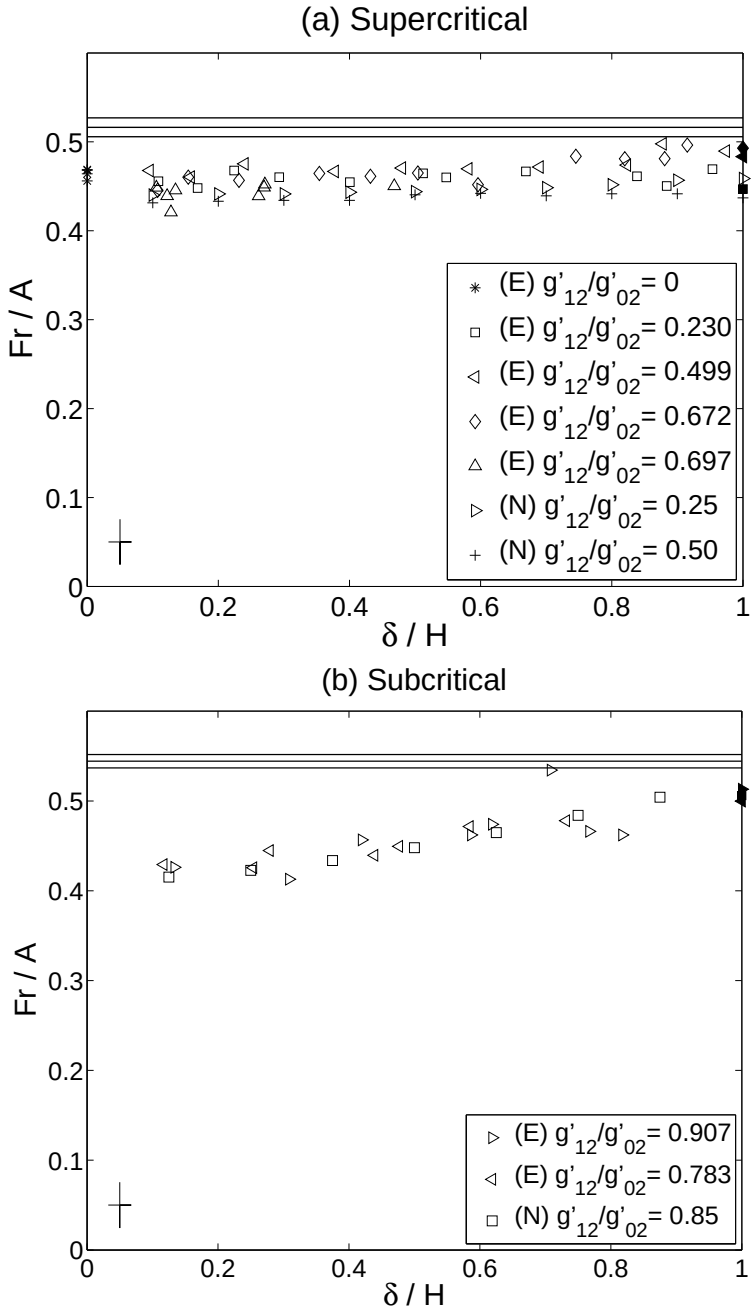

Figure 4.9: Normalized front speed versus the normalized interface thickness. (a) Supercritical flows, (b) subcritical flows. The non-dimensional front speed is given by (4.2). In the legends E and N refer, respectively, to experimental and numerical results; the latter of which are taken from Tan et al. (2010a). Lines correspond to the theoretical solution of Ungarish (2009) and are further described in the text. Results derived from the empirical correlations of Maxworthy et al. (2002) are given by the solid data points on the RHS axis. For this data, density ratios are chosen to match those of the experimental data points so that, for example, the *solid left-facing triangle* in (a) corresponds to $g'_{12}/g'_{02} = 0.499$. Representative *error bars* are as indicated.

equation (6), an empirical result based on curve fitting experimental and numerical data. Within experimental error, these results of Maxworthy et al. (2002) are indistinguishable from the present large δ/H measurements.

Analogous results for subcritical gravity currents are shown in Fig. 4.9 b. In contrast to the supercritical data, the normalized front speed of a subcritical gravity current increases, albeit rather modestly, with δ/H. The trend of the data is therefore opposite to that documented by Faust and Plate (1984). Although a satisfactory physical explanation for this trend is unknown, it seems unrelated to the magnitude of η: Appendix E shows experimental data indicating that η is independent of δ whether $g'_{12}/g'_{02} > 3/4$ or $g'_{12}/g'_{02} < 3/4$, at least when $h'_1 = h'_2$. As with the data of Fig. 4.9 a, the agreement, in the limit as $\delta/H \to 1$, with the experimental results of Maxworthy et al. (2002) and the theoretical solutions of Ungarish (2009), here exhibited for $g'_{12}/g'_{02} = 0.783$, 0.850 and 0.907, appears robust.

4.5 Deceleration

A limitation of the theoretical analysis of §2.1.1 is that, in contrast to shallow water models, it is unable to predict the horizontal location, X, where the gravity current front begins to decelerate. This analytical deficiency is addressed by presenting below experimental data that show the variation of X/ℓ with h'_1, δ/H, etc. where ℓ is the lock length. Measured results focus disproportionately on subcritical experimental data for the following reasons: (i) subcritical gravity currents typically begin to decelerate before their supercritical counterparts, and, (ii) Cantero et al. (2007) argue that two-dimensional numerical simulations of the type described in Tan et al. (2010) can, in some cases, yield erroneous predictions for X.

Fig. 4.10 shows time series of the front position for $g'_{12}/g'_{02} \simeq 0.911 \pm 0.090$ and $h'_1/H = 0.25$, 0.38, 0.5 and 0.75 ± 0.01. When the lower ambient layer

is relatively thin, the front is observed in physical (and analogue numerical) experiments to propagate without deceleration over relatively large horizontal distances. In this region of parameter space, it is postulated by Sutherland and Nault (2007) that a leaky closed-core solitary wave can be readily excited.

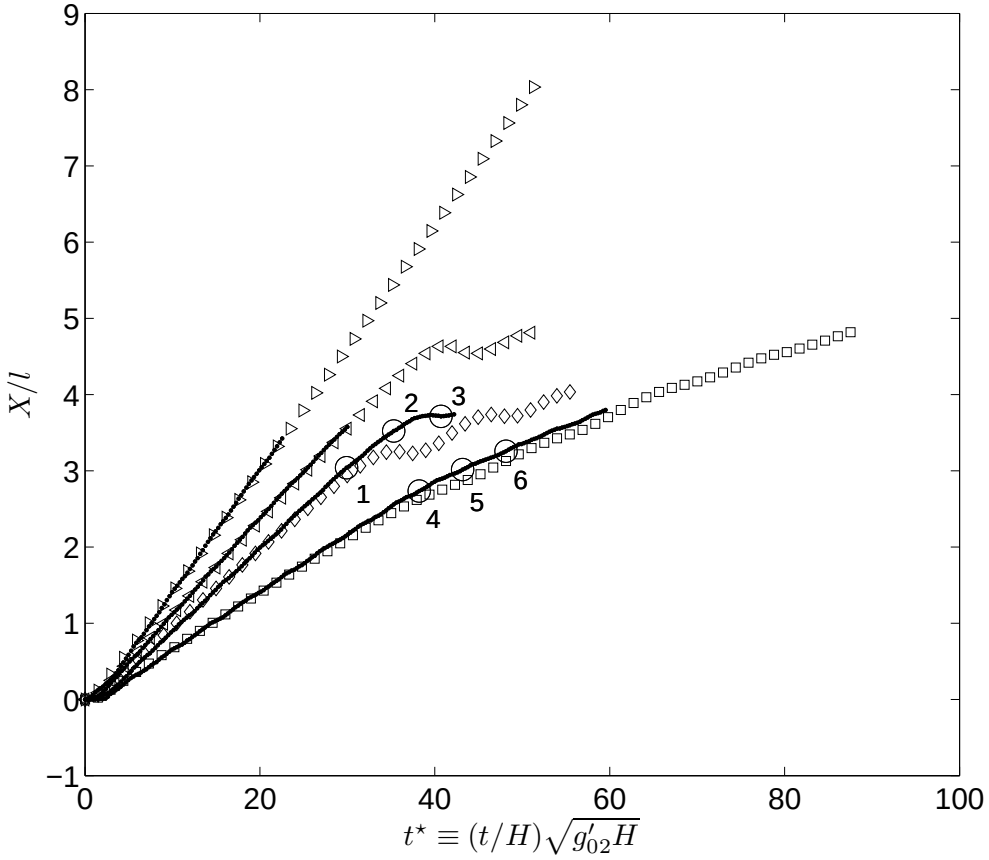

Figure 4.10: Front position versus time for four subcritical gravity currents with $g'_{12}/g'_{02} \simeq 0.911$. Numerical data points are as follows: *right-facing triangles*, $h'_1/H = 0.25$; *left-facing triangles*, $h'_1/H = 0.38$; *diamonds*, $h'_1/H = 0.50$; *squares*, $h'_1/H = 0.75$. Corresponding experimental data are given by the thin solid lines. The experimental and numerical experiments were conducted in domains of length 227.5 and 400.0 cm, respectively. Snapshots of the flow field at points 1-6 are provided below.

The wave envelops the gravity current head and transports gravity current fluid long distances at a constant speed equal to the original front speed. By contrast when $h'_1/H \geq 0.25$, the gravity current head is overtaken relatively quickly

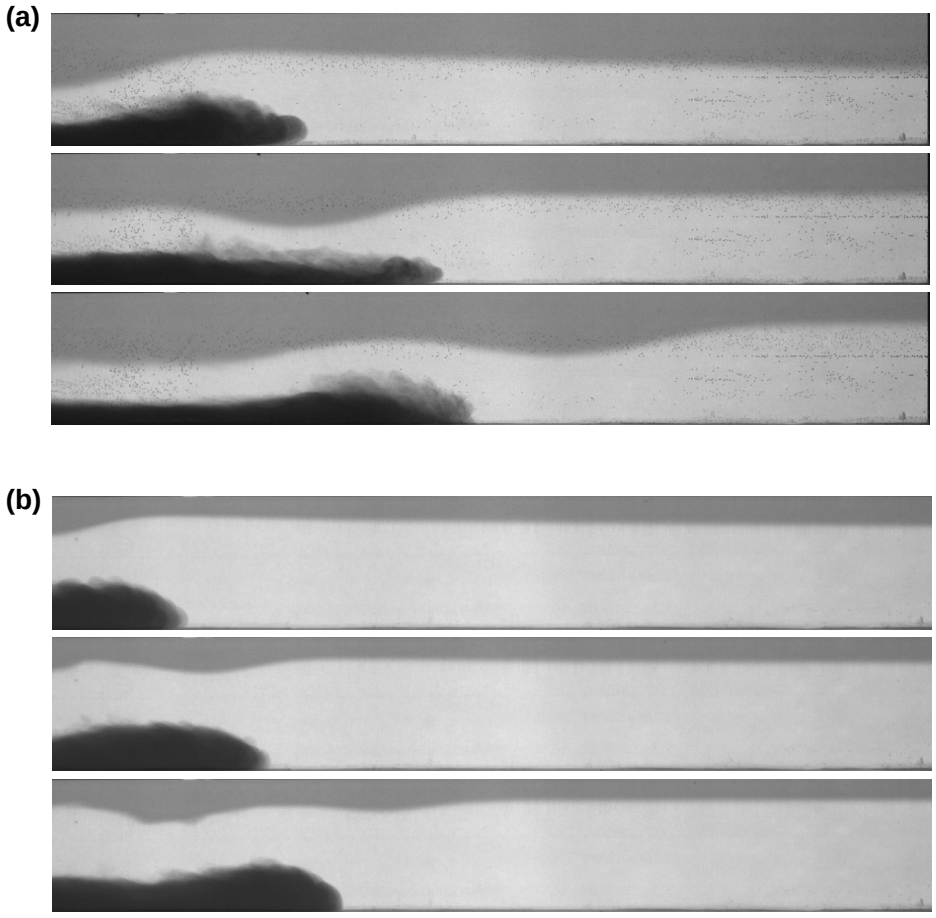

Figure 4.11: Flow snapshots corresponding to points 1, 2 and 3 (panels a) and 4, 5 and 6 (panels b) from Fig. 4.10. In all cases, the field of view is 101 cm across by 15 cm tall.

by an interfacial disturbance. In Fig. 4.10, this is exhibited most clearly by the time series associated with $h_1'/H = 0.38$ and $h_1'/H = 0.50$, which exhibit well-defined kinks at the horizontal locations where overtaking occurs. While a satisfactory theoretical estimate for the front speed of a subcritical gravity current prior to overtaking has not been successfully derived, Fig. 4.10 makes clear the restrictions of such a predictive tool: in general, it would apply over a limited spatiotemporal window. For example, when $h_1'/H = 0.50$, the front speed is constant only up until $X/\ell \simeq 3$. This is noticeably less than the corresponding transition distance for supercritical gravity currents and is also less than the non-dimensional distance at which a full-depth lock release gravity current propagating through a uniform ambient begins to decelerate (Rottman & Simpson 1983).

Experimental snapshots of the flow field at the six points defined in Fig. 4.10 are shown in Fig. 4.11. The upper and lower images consider, respectively, $h_1' = 0.50$ and 0.75. In the former case, it is observed from Fig. 4.10 a that a pronounced deceleration of the front occurs when $t^\star \equiv (t/H)\sqrt{g_{02}'H} \simeq 37$. As the wave overtakes the front, the shape of the gravity current head is demonstrably altered. A much less dramatic change of shape is noted in the lower images of Fig. 4.11 where (i) the ambient interface is further from the gravity current, and, (ii) the interfacial wave amplitude is smaller (Fig. 4.2 a). In both cases and consistent with Figs. 1, 7 and 8 of Rottman and Simpson (1989), a train of waves ultimately appears upstream of the (decelerating) gravity current front.

The variation of X/ℓ with h_1' for different g_{12}'/g_{02}' is depicted in Fig. 4.12 a. Although there is some scatter in the data reflecting the possible influence of end wall effects, it seems clear that X/ℓ increases with decreasing h_1'/H and g_{12}'/g_{02}'. In particular and consistent with the above remarks and also the investigation of Sutherland and Nault (2007), the gravity current is observed to propagate

for long distances at constant speed when $g'_{12}/g'_{02} \leq 0.25$.

The dependence of X/ℓ on g'_{12}/g'_{02} for various ambient interface heights is further elucidated by Fig. 4.12 b. Subcritical gravity currents begin to decelerate after traveling as little as 3 lock lengths (see also Fig. 4.10); their supercritical counterparts travel without change of speed over much longer horizontal distances, particularly as $g'_{12}/g'_{02} \to 0$.

In Fig. 4.12 c, X/ℓ is observed to be an increasing function of the interface thickness for the special case where $h'_1 = h'_2$. This observation can be understood in connection with the data of Fig. 4.12 a: as δ/H increases, the effective depth of the lower ambient layer decreases so that the gravity current is again able to travel long distances without deceleration. Also, from the discussion of Fig. 4.9 b, recall that the front speed of a subcritical gravity current increases with δ whereas η, and presumably the wave speed, c, shows no systematic variation (see Appendix E). Because X and $c - U$ are inversely related i.e. $X \propto c/(c-U)$, X is therefore expected to increase with δ.

Finally, in Fig 4.12 d, X/ℓ is shown to be an increasing function of D/H. While the experimental data considered in the panel are for $h'_1/H = 0.50$, the trend is expected to be similar for other values of h'_1/H. As D decreases, the volume of the gravity current fluid decreases, resulting in a more rapid deceleration of the gravity current front. This observation further reinforces the explanation for the decreasing trend found in Fig. 4.6.

4.6 Dimensionless numbers

In this study, two dimensionless numbers were discussed in some detail: Reynolds number and Froude number. For completeness, other dimensionless numbers are considered here. The Rossby number, $\mathrm{Ro} \equiv U/(Lf)$, where $f \sim 10^{-4}\,\mathrm{s}^{-1}$ and L is the characteristic length, describes the ratio of inertial to Coriolis forces. For the experimental setup described here, $\mathrm{Ro} \simeq 434$ which is sufficiently large such

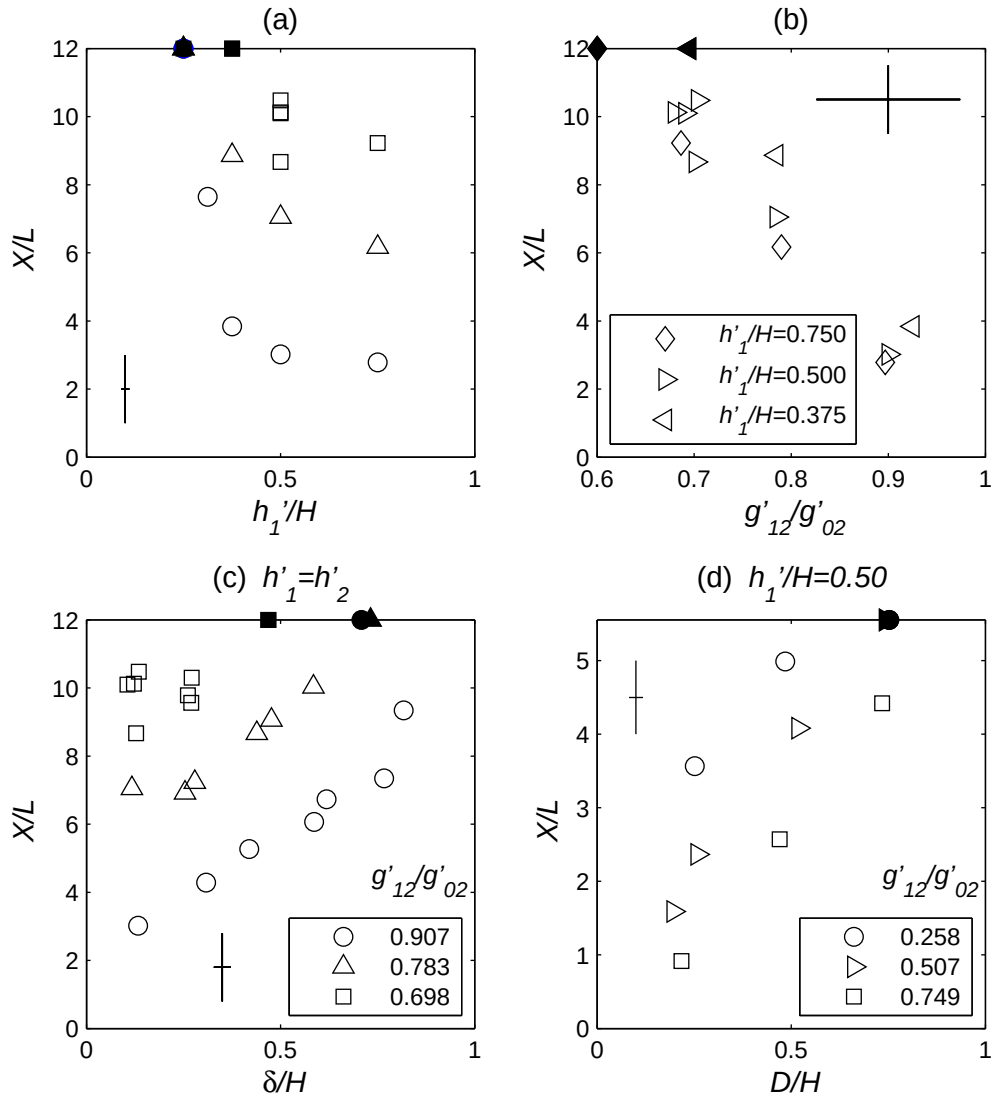

Figure 4.12: Normalized point of first deceleration, X/ℓ, vs. (a) h_1'/H for $g_{12}'/g_{02}' = 0.900$ (circles), $g_{12}'/g_{02}' = 0.785$ (triangles), and, $g_{12}'/g_{02}' = 0.694$ (squares) with $\delta/H \simeq 0.123$; (b) g_{12}'/g_{02}' for various h_1'/H with $\delta/H \simeq 0.123$; (c) δ/H for various g_{12}'/g_{02}' with $h_1' = h_2'$; and, (d) D/H for various g_{12}'/g_{02}' with $h_1'/H = 0.50$. In each case, only experimental data is considered. For panels (a), (b), (c) solid markers denote runs for which $X/\ell > 12$. Solid markers in panel (d) denote runs where $X/\ell > 5.5$. Representative error bars are as indicated. In panel (b), the horizontal error bar is longer than those of Fig. 4.4 because of the larger values for g_{12}'/g_{02}' considered here.

that Coriolis effects are small. For environmental flows, taking $U = 10\,\mathrm{m/s}$, L is approximately 100 km when $\mathrm{Ro} \simeq 1$, indicating that the gravity current must travel a long distance before Coriolis effects become important.

The Rayleigh number can be expressed as $\mathrm{Ra} = \mathrm{Re} \times \mathrm{Pe}$ where $\mathrm{Pe} \equiv HU/\alpha$ is the Péclet number and α is the thermal diffusivity. The Reynolds number for the experiments and environmental flows are $\sim 10^4$ and $\sim 10^8$, respectively. The Péclet number, which describes the ratio of the rate of advection to diffusion, is approximately $\sim 10^5$ and $\sim 10^9$ for laboratory experiments and environmental flows (i.e. due to temperature variations in water), respectively. In either case, both parameters are sufficiently large such that the dynamics of larger scale gravity currents can be captured in smaller laboratory setups.

The Richardson number, $\mathrm{Ri} \equiv N^2/(\mathrm{d}u/\mathrm{d}z)^2$, where N is the buoyancy frequency. The dimensionless number measures the ratio of suppression of turbulence due to buoyancy and the shear generation of turbulence. As is evident from experimental images of the phenomena (see Fig. 3.3), the turbulent structures are very prominent behind the gravity current head. However, at the front, the interface between the gravity current and the ambient fluid is sharp and devoid of the aforementioned structures. Furthermore, the speed of the front, U, is observed to be relatively insensitive to the turbulent structures as is evident by the strong agreement between the measured results and the theoretical model, which does not consider these effects. Additionally, the fluids in this study are miscible so that dimensionless numbers that consider the effects of surface tension (e.g. Bond number, Weber number) are trivial.

Chapter 5

Conclusions

5.1 Summary of present contribution

The behaviour of a gravity current in uniform surroundings has been debated, if not resolvedly understood, for 40 years, however, less attention has been devoted to the scenario of a stratified ambient, in particular a two-layer stratified ambient where the layer densities are either both smaller than or larger than that of the intruding horizontal flow. For the case of a dense Boussinesq gravity current with an upper layer of infinite depth, Rottman & Simpson (1989) argued that subcritical conditions are likely to be observed whereby the gravity current front speed, U, is less than that of the interfacial disturbance (see e.g. Figs. 2 and 7 of their paper). In contrast, the present work considers ambient layers of finite vertical extent. From the theoretical model of §2.1.1, itself an extension of the classical theory of Benjamin (1968), it is shown that a supercritical gravity current is assumed whenever $g'_{12}/g'_{02} \leq 3/4$ and $D = H$, where D is the initial depth of the gravity current fluid and H is the channel height.

A further and more tangible objective of the analysis is to estimate the front speed of a supercritical gravity current during the slumping phase of motion. Fig. 4.4 shows a comparison between measured and predicted non-dimensional front speeds for various combinations of layer depths and densities corresponding to full depth lock release experiments. The former data set is comprised of both

experimental (§3) and independent numerical measurements. Notwithstanding a constant offset between theory and observation, which is also observed in related studies and is due, most likely, to surface drag effects, the level of agreement is encouraging. Over the broad range of parameter space considered in Fig. 4.4, model output does not display the discontinuities or multiplicities that characterize other theoretical solutions (i.e. Holyer & Huppert 1980). Note as well that an *a-priori* estimate of the volumetric flow rate is not required in order to make the comparison. Rather, model closure is obtained via (2.8), which proposes, from heuristic reasoning, an equation for the amplitude of the interfacial disturbance in terms of the depths of the upper and lower ambient layers. The order-one validity of (2.8) is established by a favorable comparison against measured data (Fig. 4.2 and Fig. 4.3).

In order to extend the theoretical model to the more general case where $D < H$, a new parameterization of the amplitude of the interfacial disturbance is required. This parameterization, (2.14), is presented in §2.1.2. Despite the favorable comparison between the proposed parameterization and measured results, as shown in Fig. 4.5, combining the new parameterization with mass and momentum conservation (2.5) along with energy conservation along either the upper (2.7) or lower ambient layer (2.6), yielded unphysical results. However, as shown in Fig. 4.8, the model derived for the special case where $D = H$ adequately predicts the speed of propagation in the range $0.5 \lesssim D/H \leq 1$. In Fig. 4.8, it is observed that supercritical gravity currents are typically faster than the larger of the long wave speed (2.10) and the internal bore speed (2.11) while subcritical gravity currents are typically slower.

Recognizing that interfaces in the environment are often diffuse rather than sharp, the impact of the interfacial thickness, δ is considered in §4.4. Surprisingly, it is observed that the variation of U with δ is either modest (subcritical gravity currents) or practically nonexistent (supercritical gravity currents) even

as the interface comes to span the entire channel depth (Fig. 4.9). In the limiting case $\delta/H \to 1$, one can draw comparisons against analogue analytical results (Ungarish 2009). As in the two-layer case, theory moderately over-predicts the measured results, which in turn agree with the empirical results of Maxworthy et al. (2002).

The investigation is concluded with an experimental examination of the horizontal distance, X, at which the gravity current front begins to decelerate. Results are presented in Fig. 4.12, which shows the variation of X with the ambient interface height, g'_{12}/g'_{02}, δ/H and D/H. Conversely in Fig. 4.11, two instances in which the gravity current head is overtaken by the interfacial disturbance are compared. The severity of the ensuing deceleration is observed to depend most especially on the ambient interface height.

5.2 Outlook and future work

The investigation described here is but a first step in describing flows in the environment as they are typically characterized by many factors not considered here. While a flat bottom boundary is assumed in this study, naturally occurring gravity currents typically propagate across nonuniform bottom boundaries such as mountainous terrain and buildings. The assumption of a rectilinear geometry also limits the applicability of the model. Previous observations (e.g. Simpson 1997) have shown that axisymmetric dispersion where the gravity current fluid originates from a single point source are more common. Examples of this are thunderstorm outflows, or an oil spill originating from a single tanker. Moreover, smaller scale gravity currents that occur in buildings, for example, are typically affected by obstacles such as doorways, complex building designs, tables and other common objects, etc. Further complications may arise if the effects of factors such as diurnal variations and anthropogenic sources (e.g. heat from vehicles, buildings etc.) on ambient stratification are considered.

Future works could extend the model to the more general case where $D < H$. Additionally, the subcritical regime, where a physical solution utilizing a steady state model was not obtained, could be studied in further detail. Investigating the dynamics of the gravity current when complicating factors, such as obstacles and complex topography, are included is also a possibility. It would be worthwhile to develop a model that provides a solution for a variable number of layers, bridging the gap between the limit where the ambient is uniform to where it is linearly stratified. We hope that the analysis described here provides an adequate base of which future projects may be built from.

Bibliography

Baines, P. G. (1995). *Topographic Effects in Stratified Flows*. Cambridge UK: Cambridge University Press.

Benjamin, T. B. (1968). Gravity currents and related phenomena. *J. Fluid Mech. 31*, 209–248.

Cantero, M. I., J. R. Lee, S. Balachandar, and M. H. Garcia (2007). On the front velocity of gravity currents. *J. Fluid Mech. 586*, 1–39.

Cheong, H.-B., J. J. P. Kuenen, and P. F. Linden (2006). The front speed of intrusive gravity currents. *J. Fluid Mech. 552*, 1–11.

Faust, K. M. and E. J. Plate (1984). Experimental investigation of intrusive gravity currents entering stably stratified fluids. *J. Hydraul. Res. 22*(5), 315–325.

Fernando, H. J. S. (2010). Fluid dynamics of urban atmospheres in complex terrain. *Annual Review of Fluid Mechanics 42*, 365–389.

Flynn, M. R. and P. F. Linden (2006). Intrusive gravity currents. *J. Fluid Mech. 568*, 193–202.

Härtel, C., E. Meiburg, and F. Necker (1999). Vorticity dynamics during the start-up phase of gravity currents. *Il Nuovo Cimento 22*, 823–833.

Holyer, J. Y. and H. E. Huppert (1980). Gravity currents entering a two-layer fluid. *J. Fluid Mech. 100*, 739–767.

Hoult, D. P. (1972). Oil spreading on the sea. *Annual Review of Fluid Mechanics 4*, 341–368.

Huppert, H. E. and J. E. Simpson (1980). The slumping of gravity currents. *J. Fluid Mech. 99*, 785–799.

Keulegan, G. H. (1957). An experimental study of the motion of saline water from locks into fresh water channels. Technical Report 5168, Nat. Bur. Stand. Rept.

Klemp, J. B., R. Rotunno, and W. C. Skamrock (1997). On the propagation of internal bores. *J. Fluid Mech. 331*, 81–106.

Lim, K., G. Ivey, and R. Nokes (2008). The generation of internal waves by tidal flow over continental shelf/slope topography. *Environmental Fluid Mechanics 8*, 511–526.

Linden, P. F., G. F. Lane-Serff, and D. A. Smeed (1990). Emptying filling boxes: the fluid mechanics of natural ventilation. *J. Fluid Mech. 212*, 309–335.

Lowe, R. J., P. F. Linden, and J. W. Rottman (2005). The non-Boussinesq lock exchange problem. Part 1: Theory and experiments. *J. Fluid Mech. 537*, 101–124.

Maxworthy, T., J. Leilich, J. E. Simpson, and E. H. Meiburg (2002). The propagation of a gravity current into a linearly stratified fluid. *J. Fluid Mech. 453*, 371–394.

Moore, D. S. and G. O. McCabe (1993). *Introduction to the practice of statistics* (2nd ed.). New York: W. H. Freeman and Company.

Oster, G. (1965). Density gradients. *Sci. Am. 213*, 70.

Rottman, J. W. and J. E. Simpson (1983). Gravity currents produced by instantaneous releases of a heavy fluid in a rectangular channel. *J. Fluid Mech. 135*, 95–110.

Rottman, J. W. and J. E. Simpson (1989). The formation of internal bores in the atmosphere: A laboratory model. *Quarterly Journal of the Royal Meteorological Society 115*, 941–963.

Shin, J. O., S. B. Dalziel, and P. F. Linden (2004). Gravity currents produced by lock exchange. *J. Fluid Mech. 521*, 1–34.

Simpson, J. E. (1997). *Gravity Currents* (2nd ed.). Cambridge, England: Cambridge University Press.

Simpson, J. E. and R. E. Britter (1979). The dynamics of the head of a gravity current advancing over a horizontal surface. *J. Fluid Mech. 94*, 477–495.

Sutherland, B. R., P. J. Kyba, and M. R. Flynn (2004). Intrusive gravity currents in two-layer fluids. *J. Fluid Mech. 514*, 327–353.

Sutherland, B. R. and J. T. Nault (2007). Intrusive gravity currents propagating along thin and thick interfaces. *J. Fluid Mech. 586*, 109–118.

Tan, A., D. Nobes, B. Fleck, and M. Flynn (2010a). Gravity currents in two-layer stratified media. *Environmental Fluid Mechanics*, 1–21. 10.1007/s10652-010-9174-z.

Tan, A., D. Nobes, B. Fleck, and M. Flynn (2010b). Partial depth gravity currents in two-layer stratified media. Part 1: A study of the wave amplitude. In *International Conference of Environmental Science and Engineering*. World Academy of Science and Engineering.

Ungarish, M. (2006). On gravity currents in a linearly stratified ambient: a generalization of benjamin's steady-state propagation results. *J. Fluid Mech. 548*, 49–68.

Ungarish, M. (2009). *An introduction to gravity currents and intrusions.* Boca Ratol, FL, USA: CRC Press.

Ungarish, M. and H. E. Huppert (2002). On gravity currents propagating at the base of a stratified ambient. *J. Fluid Mech. 458*, 283–301.

Appendix A

Derivation of the Benjamin (1968) Solution

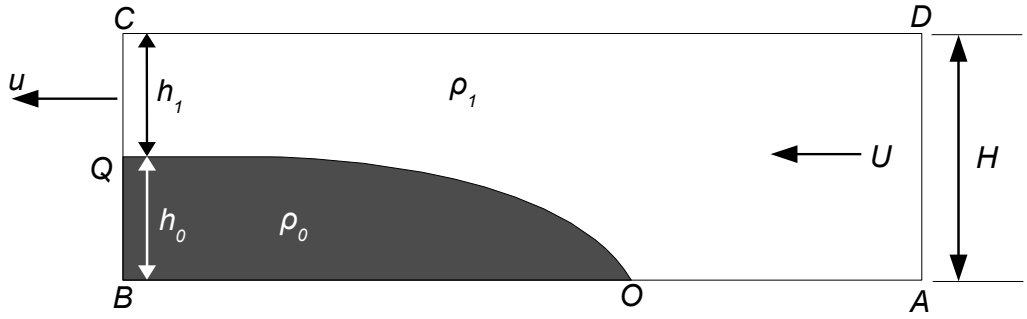

Figure A.1: Definition sketch of a dense gravity current (fluid of density ρ_0) and the control volume $ABCD$.

In this section, we briefly discuss the derivation of the model developed by Benjamin (1968) for a gravity current propagating into a uniform ambient. In Fig. A.1, a primarily horizontal flow of a dense gravity current propagating along a horizontal boundary through a uniform ambient of depth H is considered. In the analysis, the control volume $ABCD$ is chosen such that gravity current is stationary and ambient fluid flows, without mixing from right to left. The gravity current, considered to be horizontal away from the front, has a depth of h_0 and a density of $\rho_0 > \rho_1$. Far upstream from O, we may relate the fluid velocity U, which is the gravity current front speed in the laboratory reference frame, with the depth-independent ambient velocity u by applying

mass conservation:

$$uh_1 = UH. \tag{A.1}$$

Taking the pressure at the stagnation point, p_O to be zero, the pressure at point A maybe be found by applying Bernoulli's equation along OA such that

$$p_A = -\frac{1}{2}\rho_1 U^2. \tag{A.2}$$

Far up- and downstream, vertical accelerations are assumed to be negligible such that the pressure field is hydrostatic. Along the vertical segment AD the pressure field can be written as:

$$p = -\frac{1}{2}\rho_1 U^2 - \rho_1 g H. \tag{A.3}$$

Similarly, the pressure field along the vertical segment BC:

$$p = \begin{cases} -\rho_0 g z & 0 \leq z \leq h_0 \\ -\rho_0 g h_0 - \rho_1 g(z - h_0) & h_0 \leq z \leq H \end{cases} \tag{A.4}$$

Conservation of horizontal momentum flux within the constant volume $ABCD$ yields

$$\int_A^D p + \rho u^2 \, \mathrm{dz} = \int_B^C p + \rho u^2 \, \mathrm{dz} \tag{A.5}$$

which can then be combined with equations (A.3), (A.4) and (A.1) to arrive at the final expression relating the front speed, U to the height of the gravity current, h_0 and the channel depth, H:

$$\mathrm{Fr} \equiv \frac{U}{\sqrt{g'H}} = \sqrt{\frac{(H - h_0)(2H - h_0)}{(H + h_0)} \frac{h_0}{H^2}} \tag{A.6}$$

where $g' = g(\rho_0 - \rho_1)/\rho_1$ and g is the acceleration due to gravity. As mentioned briefly above, (A.6) represents one equation and two unknowns and thus an additional equation is required to close the system. If the system is assumed

to be free of dissipation, one can apply Bernoulli's equation along the interface OQ to arrive at the additional equation:

$$u = \sqrt{2g'h_0}. \tag{A.7}$$

Combining equation A.7 and A.1 with equation A.6 results in two solutions for depth of the gravity current:

$$\frac{h_0}{H} = \frac{1}{2} \qquad \text{or} \qquad \frac{h_0}{H} = 0. \tag{A.8}$$

The former solution shows that the gravity current must span half the channel depth and is realized to a very good approximation in full depth lock release experiments (Shin et al. 2004). Applying this result in equation (A.6), we arrive at the Benjamin's energy conserving solution: Fr= $\frac{1}{2}$.

Appendix B

Alternate Fr definition

An alternate definition for Fr is:

$$\mathrm{Fr}_e = \frac{U}{\sqrt{g'_e H}} \tag{B.1}$$

where

$$g'_e = \frac{g}{\rho_{00}} \left(\rho_0 - \frac{\rho_1 h'_1 + \rho_2 h'_2}{H} \right). \tag{B.2}$$

The two methods described in this thesis for non-dimensionalizing U have their respective merits and demerits. Equation (B.1) allows for Benjamin's energy conserving solution of Fr=$\frac{1}{2}$ to be recovered as $h'_1/H \to 0, 1$ in contrast to (2.2) which results in a different value for Fr when $h'_1/H \to 1$ (see Fig. 4.4). Moreover, the deviation between the predicted Fr and Benjamin's energy conserving solution of Fr = $\frac{1}{2}$ for a uniform ambient quantifies the dynamical impact of the interfacial disturbance shown schematically in Fig. 2.1. However, defining Fr as in (2.2) allows for a more intuitive understanding of the impact on the speed of a gravity current when a fluid of intermediate density (e.g. ρ_1) is added to the bottom of the ambient; that is, as more of the intermediate density fluid is added, the gravity current propagates slower.

Fig. B.1 a–c shows the variation of Fr_e with h'_1/H for $g'_{12}/g'_{02} = 0.25, 0.50$ and 0.75, respectively. As before, analytical solutions are obtained by solving

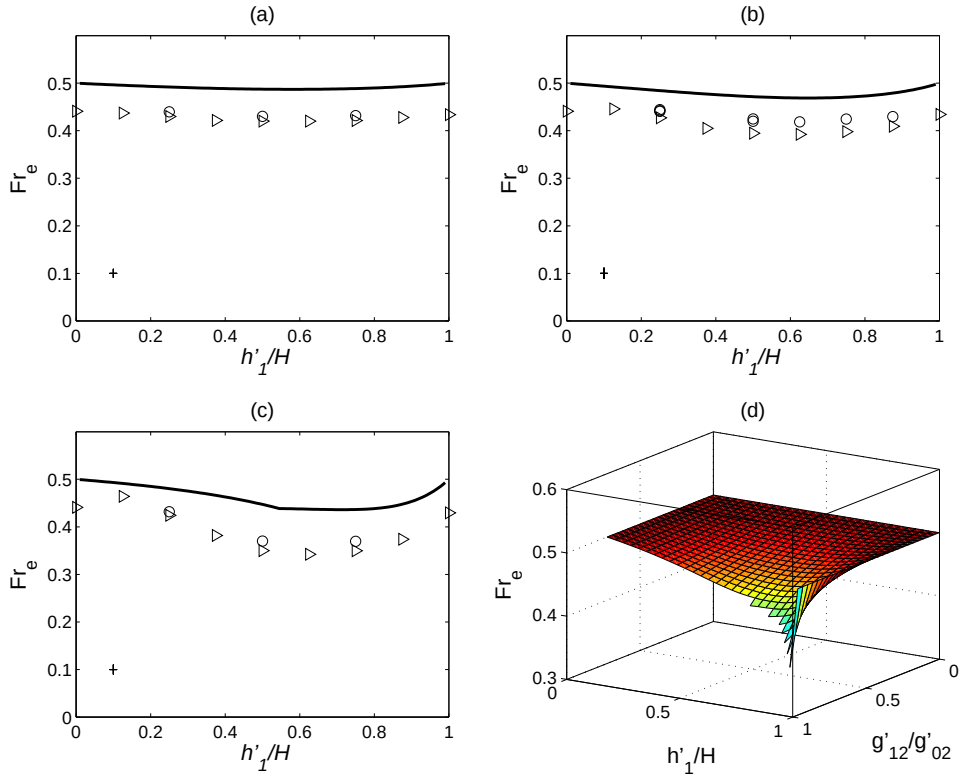

Figure B.1: (a) Fr_e, as defined by (2.2), vs. h_1'/H for $g_{12}'/g_{02}' = 0.250$, (b) $g_{12}'/g_{02}' = 0.500$ and (c) $g_{12}'/g_{02}' = 0.750$. Data points are as follows: *open triangles*–numerical results; *open circles*–experimental results. The solid curve gives the corresponding theoretical result. Representative error bars for the experimental data are as indicated. Panel (d) show the variation of Fr_e with h_1'/H and g_{12}'/g_{02}'.

(2.5), (2.6) and (2.8). Here, as with Fig. 4.4, the agreement between theoretical and measured results is satisfactory: though theory again over predicts the measured data, this feature is likely due to bottom friction. Consistent with the above remarks, the energy conserving solution of Benjamin (1968) is recovered in the limiting cases $h_1'/H = 0$, 1. Fig. B.1 d is analogous to the upper surface in Fig. 2.5 a except that U is now non-dimensionalized using (B.1). Here, we observe generally modest variations of Fr_e with h_1'/H and g_{12}'/g_{02}'. (Note the difference of vertical scales between Figs. B.1 and 2.5 a).

Appendix C

Sample density profile for thick interface experiments

Figs. C.1, C.2, and C.3 show sample density profiles for the ambient interface of laboratory experiments. The solid line is constructed from measurements of aconductivity probe (Precision and Measurement Engineering, MSCTI), which was mounted to a computer controlled traverse (Velmex, X-Slide). Calibration was performed against stock solutions of known density to ensure that conductivity is directly proportional to density. The dotted lines are curve-fits of the three sections of the ambient i.e. lower ambient layer, interface and upper ambient layer. The thickness of the interface is measured from the intersections of the dotted lines.

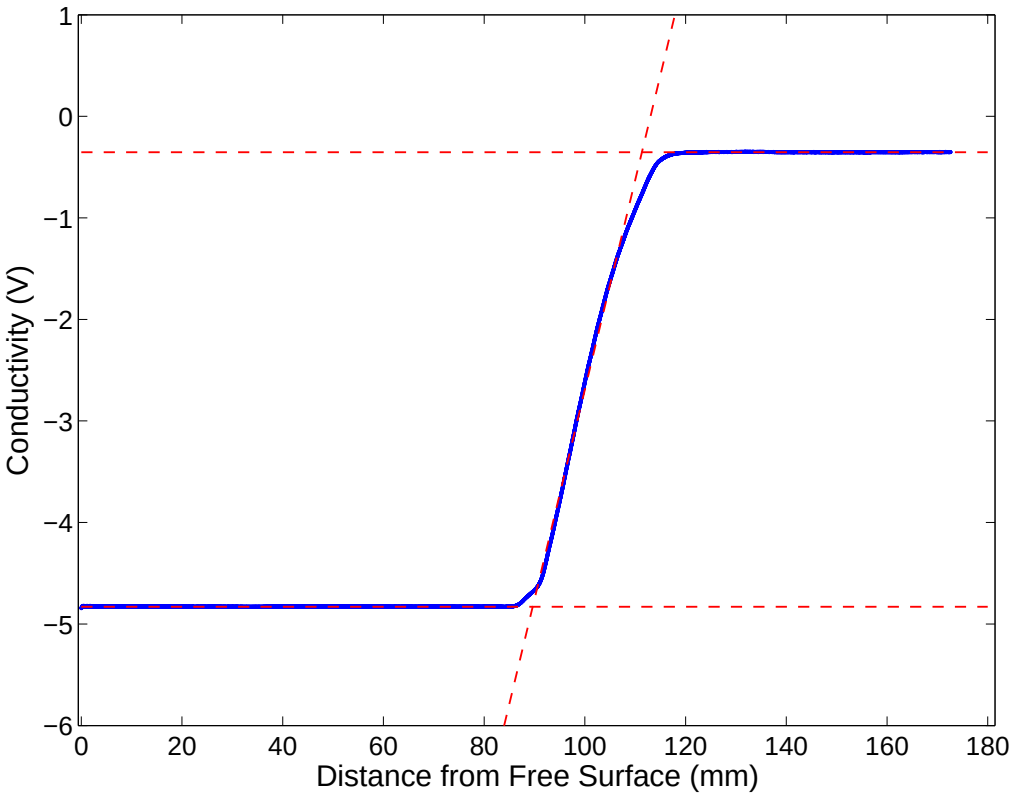

Figure C.1: Sample density profile for the ambient of a "thin" interface experiment.

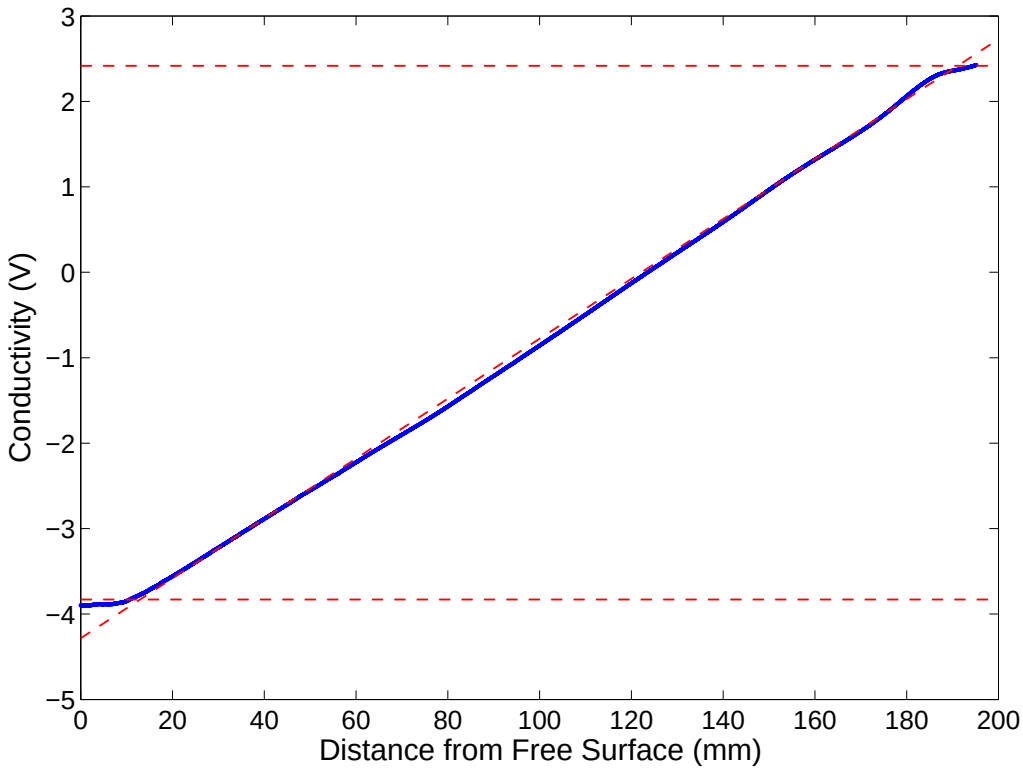

Figure C.2: Sample density profile for the ambient of a thick interface experiment.

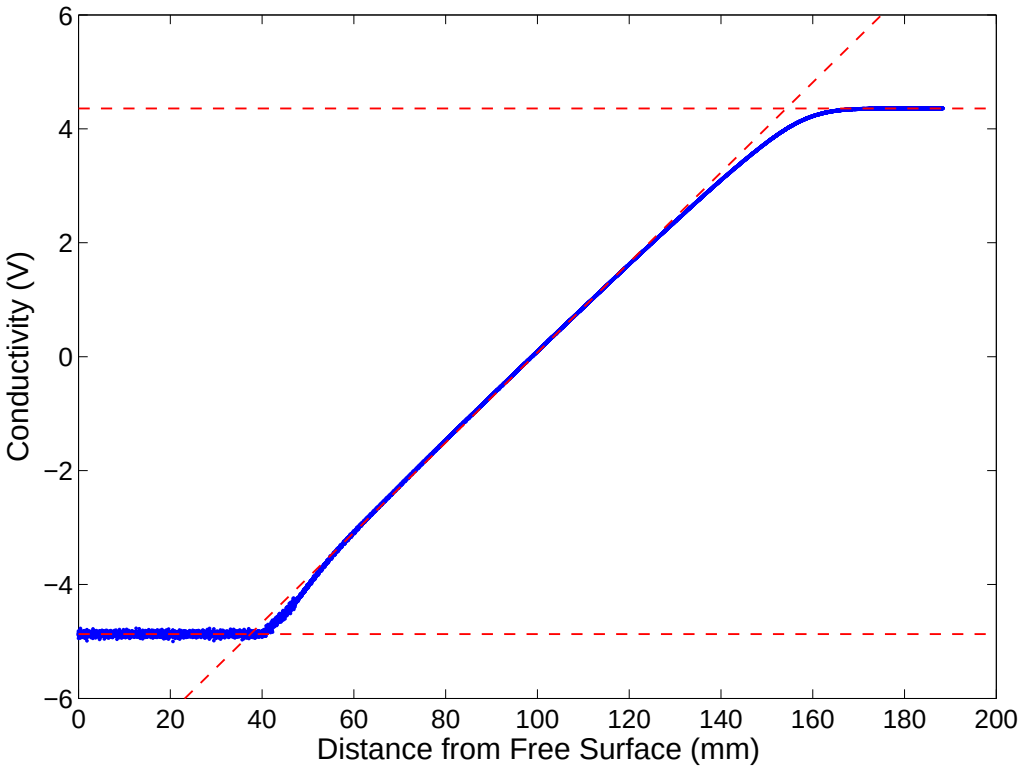

Figure C.3: Sample density profile for the ambient of a intermediate thickness interface experiment.

Appendix D

Conserving energy in lower or upper ambient layers for partial depth gravity currents

Fig. D.1 shows solutions generated from equations (2.5), (2.6) and (2.14). Panels a–d and e–h show variations of the non-dimensional layer depths h_1/H and h_0/H, respectively, with the lower ambient layer depth, h_1'/H, for $0 \leq g_{12}'/g_{02}' \leq 0.95$. The arrows indicate the direction of increasing g_{12}'/g_{02}'. Columns a, b, c, d represent $D/H = \frac{1}{4}, \frac{1}{2}, \frac{3}{4}$ and 1, respectively, so that panels d and h are identical to panels a and e in Fig. 2.4. A critical analysis of the panels shows that as $h_1'/H \to 1$, $h_0/H \to \frac{1}{2}$ regardless of the value of D/H. This indicates that even at low values of D/H, the gravity current will nonetheless span half the channel height, a prediction that is unphysical. This behaviour is observed because as $h_1'/H \to 1$, $\eta \to 0$ and the solution to the system of equations reduces to Benjamin (1968)'s energy conserving solution.

Fig. D.2 describes the variations of the non-dimensional speeds $u_1/\sqrt{g_{02}'H}$ (panels a, b, c, d), $u_2/\sqrt{g_{02}'H}$ (panels e, f, g, h) with h_1'/H for $0 \leq g_{12}'/g_{02}' \leq 0.95$ utilizing equation (2.6). The arrows indicate the direction of increasing g_{12}'/g_{02}'. Columns a, b, c, d represent $D/H = \frac{1}{4}, \frac{1}{2}, \frac{3}{4}$ and 1, respectively. Here, as with Fig. D.1, the variations due to D disappear as $h_1'/H \to 1$. In this limit, solutions are identical irrespective of D.

Fig. D.3 describes the variations of Fr (upper panel) and dissipation (lower panel) with g'_{12}/g'_{02} and h'_1/H for $D/H = \frac{1}{4}$ (panel a), $\frac{1}{2}$ (panel b), $\frac{3}{4}$ (panel c) and 1 (panel d) when equation (2.6) is utilized. Here, as with Fig. 2.5, the lower surface in the upper panels denote the composite long wave - bore surface. From the figure, we observe model breakdown at smaller values of g'_{12}/g'_{02} as $D/H \to 0$. Additionally, while a monotonic decrease of Fr as g'_{12}/g'_{02} and h'_1/H increases is observed for $D/H \gtrsim 0.5$, a non-monotonic trend is observed for $D/H \lesssim 0.5$; a prediction that cannot be recovered strictly from energy arguments of the type summarized by Cheong et al. (2006). However, this behaviour is observed as $h'_1/H \to 1$ and it is unclear whether the prediction is physical or merely an artifact of the model. The exponentially increasing dissipation at $h'_1/H \to 0$ and $g'_{12}/g'_{02} \to 0$ for $D/H \lesssim 0.5$ observed in the lower panel suggests that it is likely the latter.

Building on the solutions shown in Fig. D.3, Fig. D.4 show the variations of Fr with h'_1/H for various D/H and g'_{12}/g'_{02}. The solid lines show the solution to (2.5), (2.14), and (2.6). The composite long wave - internal bore speeds denoted by the dashed lines and measured results are indicated by the triangles and circles. Thus the latter data is identical to that shown in Fig. 4.8. While the predictions of layer heights and speeds in the limiting case of $h'_1/H \to 0$ are unphysical (Figs. D.1 and D.2), surprisingly, the prediction of Fr shows reasonable agreement with measurements, particularly for D/H not too close to 0: although the offset between theoretical and measured results observed in Fig. 4.4 is observed to increase steadily as $D/H < 1$, the qualitative agreement remains satisfactory. The broken solid curves at intermediate values of h'_1/H are caused by model breakdown and are observed to coincide with Fr $\simeq \max(c_{LW}, c_B)$.

Fig. D.5 describes the variations of h_0/H and h_1/H due to h'_1/H as in Fig. D.1 but showing model results utilizing equation (2.7) in place of (2.6). By conserving energy in the upper layer instead of the lower layer, Benjamin

(1968)'s solution is not recovered when $h_1'/H \to 1$ and $D < H$, therefore the expected behaviour (i.e. $h_0 < D$) is predicted by the model. However, when $h_1'/H \to 0$, the model predicts a non-zero value for h_1/H which is clearly unphysical. Correspondingly, h_0/H decreases rapidly in this limit. Fig. D.6, which is analogous to Fig. D.2 with the exception that equation (2.7) is utilized, shows similar behaviour. Moreover, since values of h_1 and U are non-zero, u_1 must then equal zero due to mass conservation (i.e. $u_1 h_1 = U h_1'$). This unusual behaviour is not present when $D = H$ and the change is observed to occur abruptly.

Fig. D.7 depicts the variation of Fr with g_{12}'/g_{02}' and h_1'/H as with Fig. D.3 but showing model results utilizing equation 2.7. The unusual prediction at $h_1'/H \to 0$ manifests here as well: in this limit, Fr drops rapidly when $D < H$. Moreover, dissipation increases to a large value indicating that the predictions in this limit are unphysical. As with Fig. D.4, Fig. D.8 shows variations of Fr due to h_1'/H for various values of D/H and g_{12}'/g_{02}'. Here also we observe that the theoretical predictions agree qualitatively with measured results with a steadily increasing offset between theory and measurements as $D/H < 1$. In contrast to Fig. D.4, however, the rapid drop of Fr as $h_1'/H \to 0$ is inconsistent with measured data and thus seems to be a spurious artifact of the model equations.

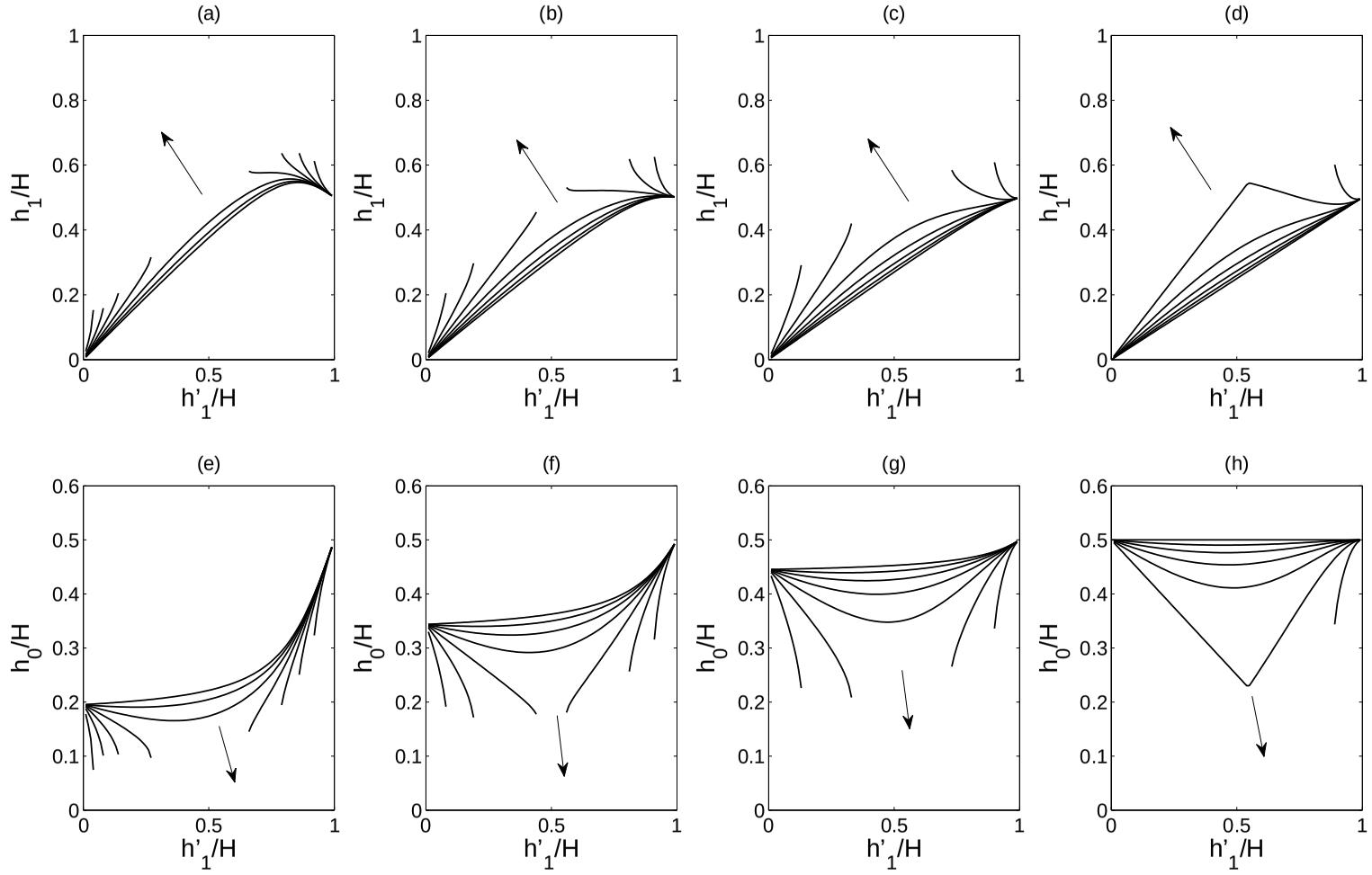

Figure D.1: Model output based on (2.5), (2.6) and (2.14). Panels a–d show h_1/H vs. h_1'/H with $D/H = \frac{1}{4}$, $\frac{1}{2}$, $\frac{3}{4}$ and 1, respectively. Panels e–h show h_0/H vs. h_1'/H with $D/H = \frac{1}{4}$, $\frac{1}{2}$, $\frac{3}{4}$ and 1, respectively. Solutions are shown for $g_{12}'/g_{02}' = 0.15$, 0.30, 0.45, 0.60, 0.75 and 0.90;. Arrows indicate the direction of increasing g_{12}'/g_{02}'. Broken lines for intermediate h_1'/H and large g_{12}'/g_{02}' are indicative of model breakdown.

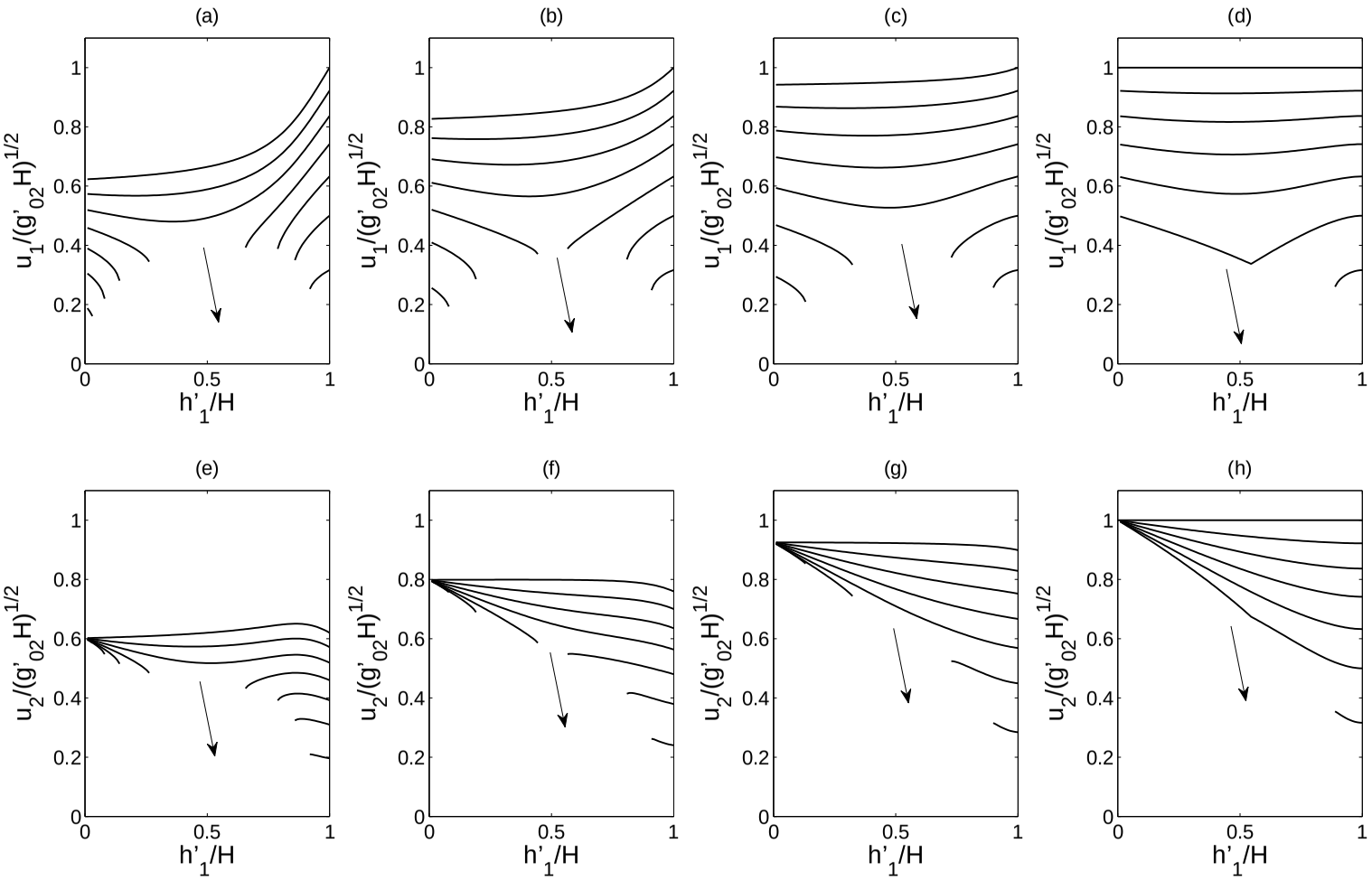

Figure D.2: As in Fig. 2.4, but showing the non-dimensional velocities $u_1/\sqrt{g'_{02}H}$ (panels a–d) and $u_2/\sqrt{g'_{02}H}$ (panels e–h)

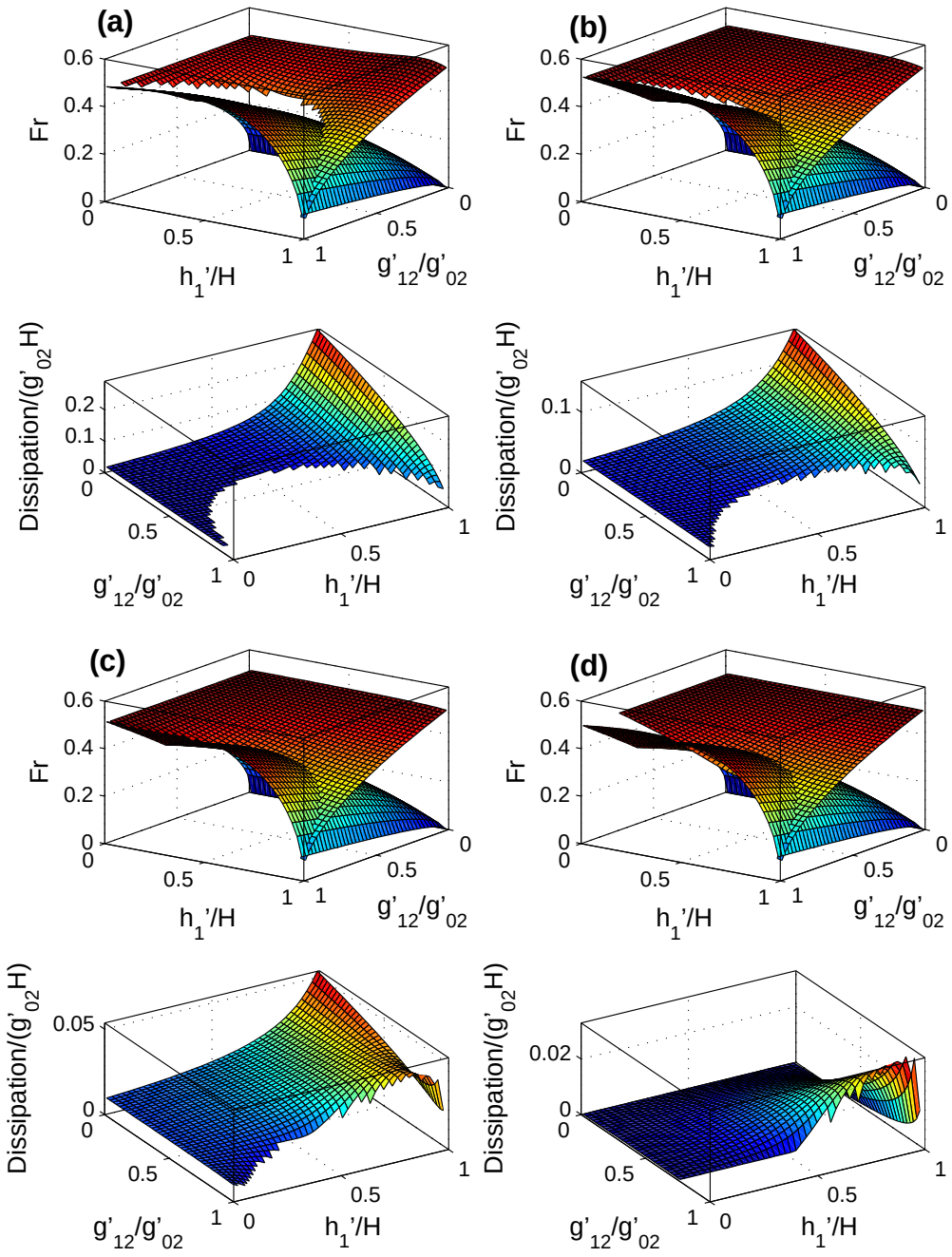

Figure D.3: (Upper panels): Non-dimensional gravity current speed, Fr, vs. g'_{12}/g'_{02} and h'_1/H (upper surface). The lower surface shows the larger of the long wave speed as predicted by (2.10) and the bore speed as predicted by (2.11) which was used with (2.14). (Lower panels): Non-dimensional dissipation function, $\Delta R/(g'_{02}H)$, as defined by (2.12). $D/H = \frac{1}{4}$, $\frac{1}{2}$, $\frac{3}{4}$ and 1 in panels a, b, c, d, respectively. Note that: (i) the orientation of the surfaces is different in the upper and lower images of each panel, (ii) axis scales of the lower image vary between each panel.

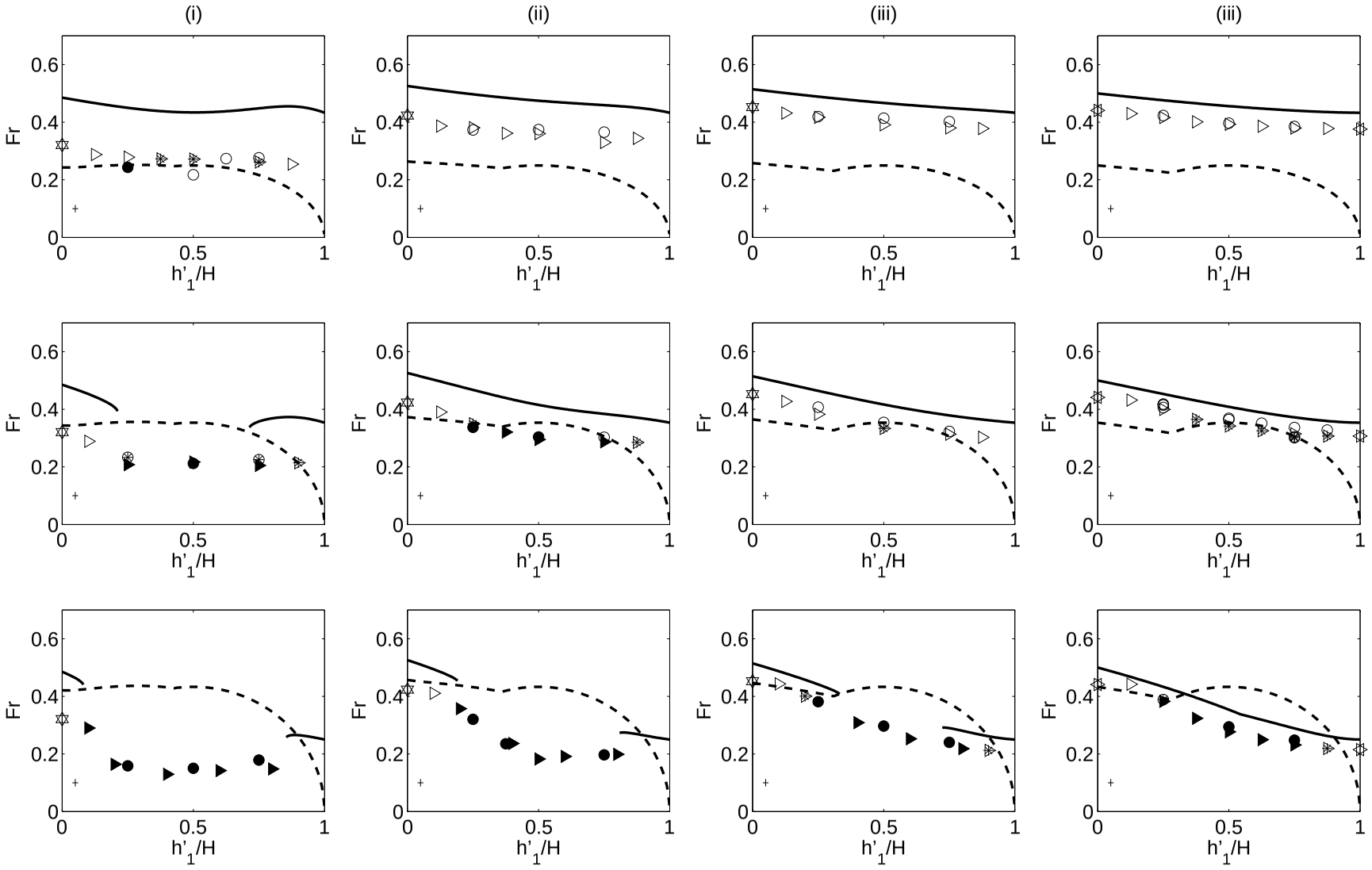

Figure D.4: As in Fig. 4.8 but showing model results based upon the solutions to equations (2.5), (2.6) and (2.14).

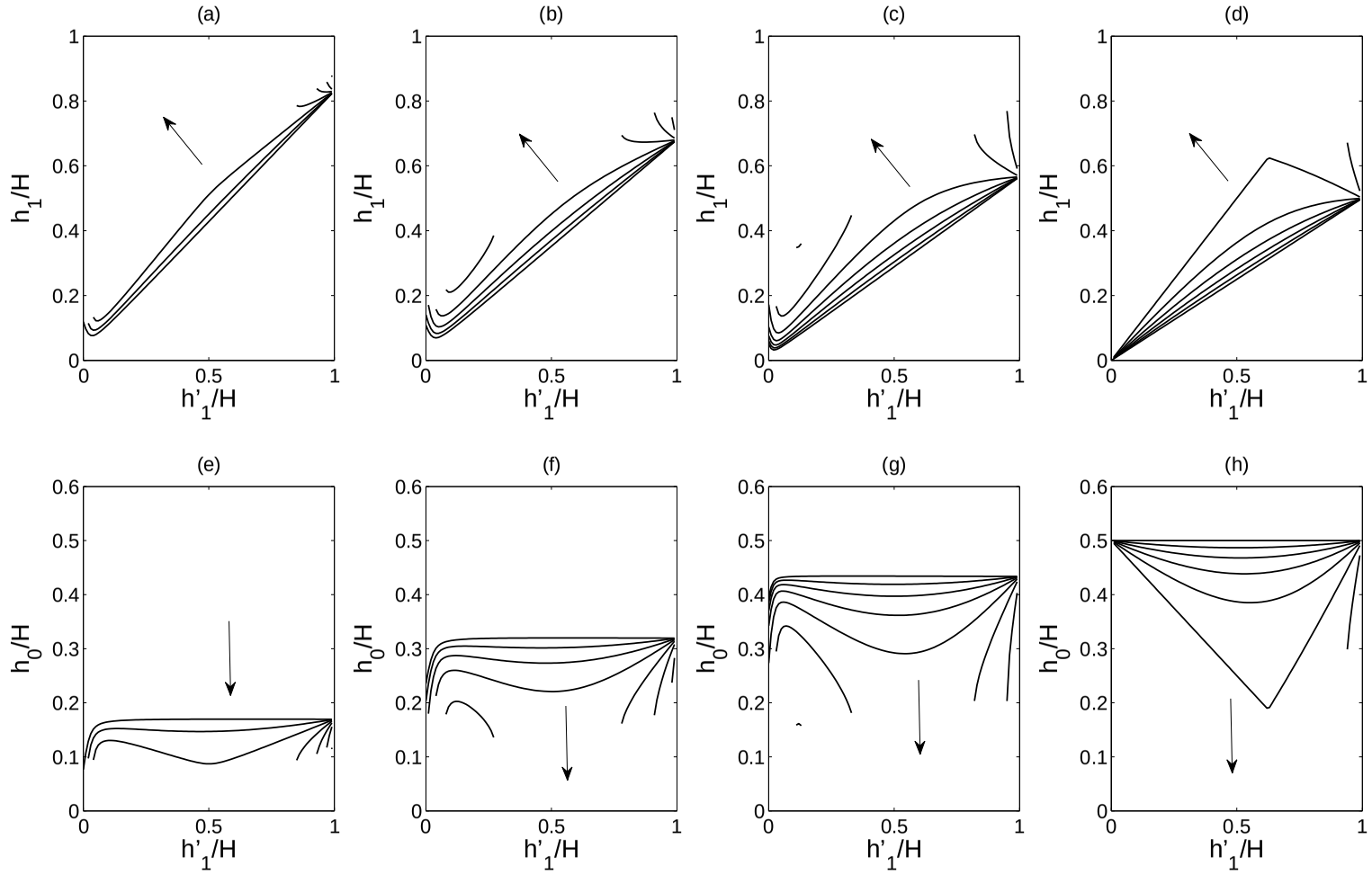

Figure D.5: As in Fig. 2.4 but showing model results based upon the solution to equations (2.5), (2.7) and (2.14).

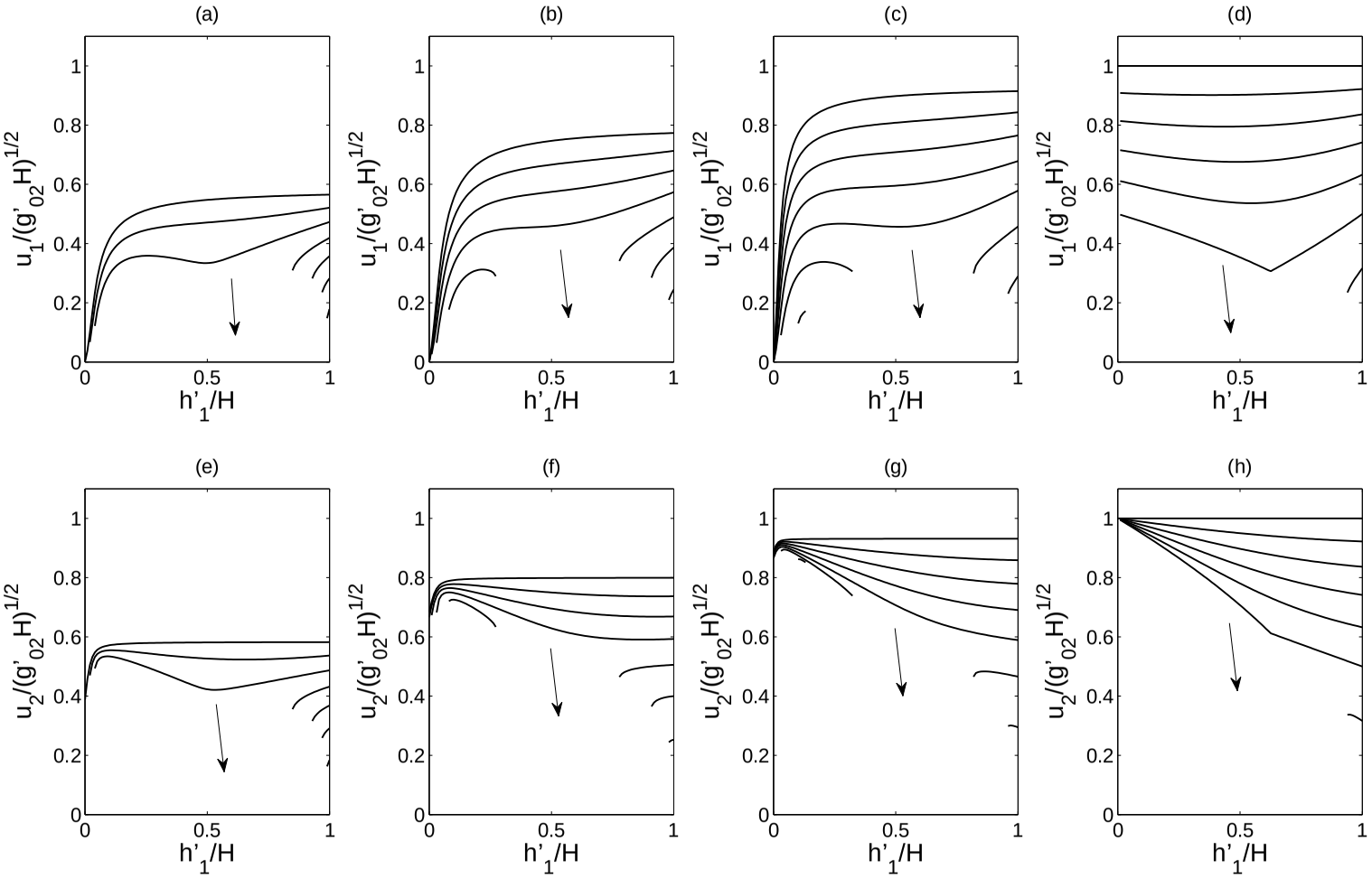

Figure D.6: As in Fig. D.2 but showing model results based upon the solution to equations (2.5), (2.7) and (2.14).

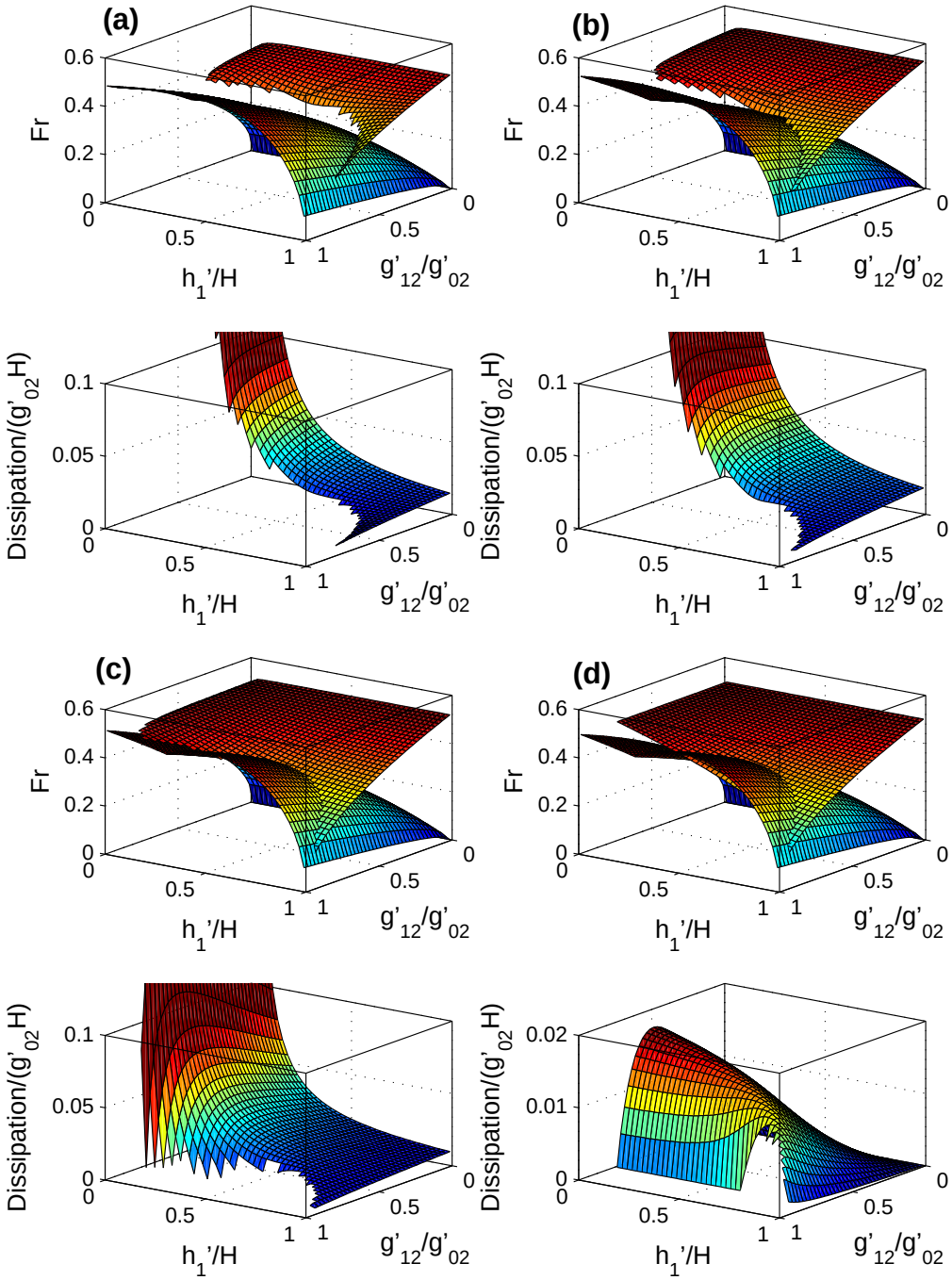

Figure D.7: As in Fig. D.3 but showing model results based upon the solution to equations (2.5), (2.7) and (2.14). The non-dimensional dissipation function is calculated using (2.13).

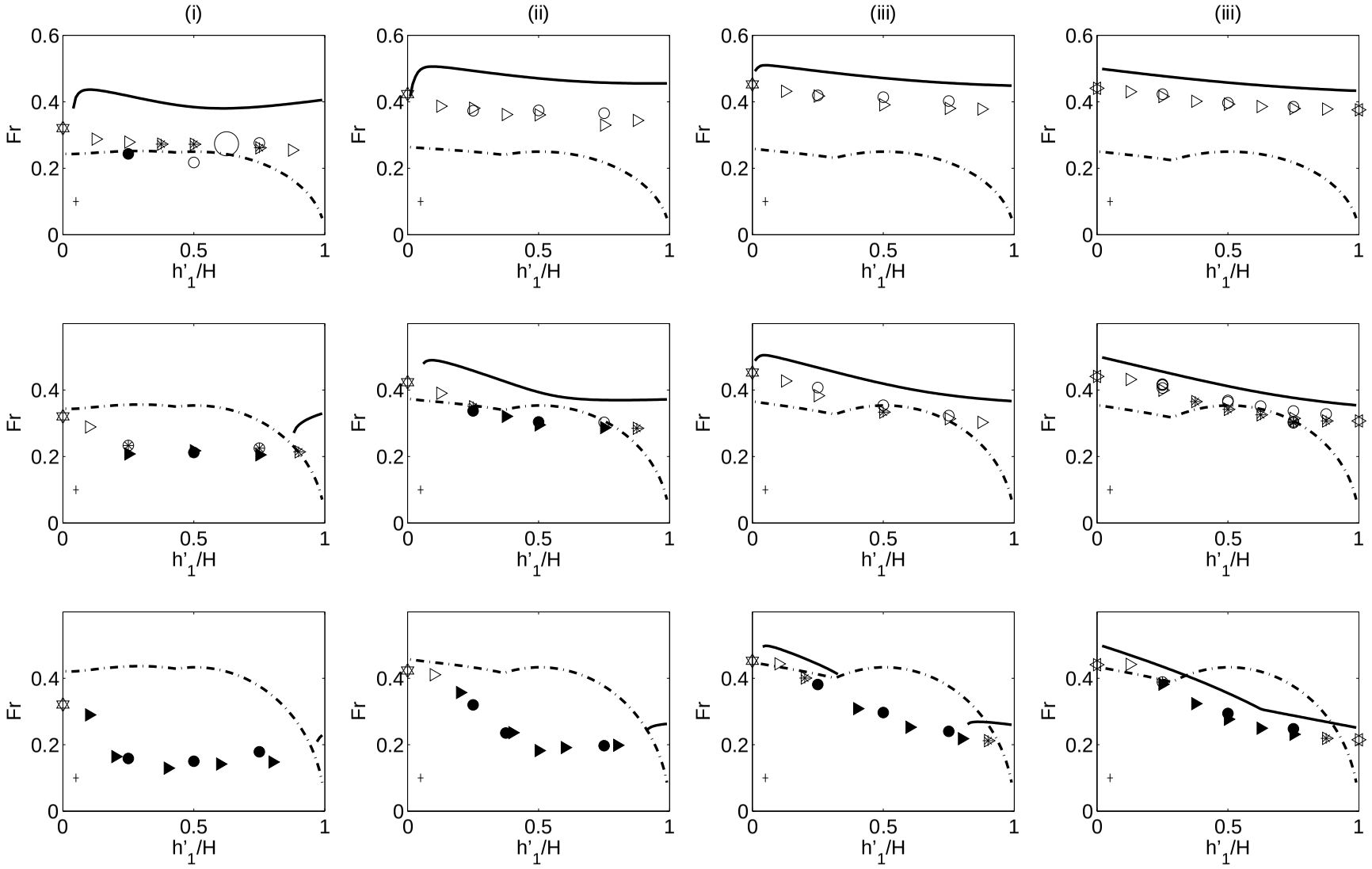

Figure D.8: As in Fig. 4.8 but showing model results based upon the solutions to equations (2.5), (2.7) and (2.14).

Appendix E

Interface thickness and deflection

The variation of η with δ is exhibited in Fig. E.1; both supercritical and subcritical experimental data are considered. In all cases, we find that the interfacial thickness has an insignificant impact on the deflection of the interface, at least within experimental error. For non-zero values of δ, measurements of η are based on the average elevation of the (thick) interface far downstream and just above the crest of the gravity current head.

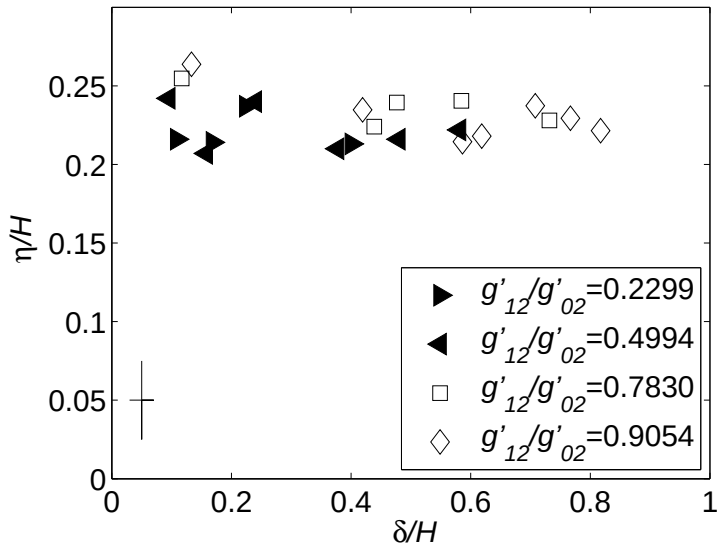

Figure E.1: The correlation of interface thickness and deflection for a range of values of g'_{12}/g'_{02}. For the experiments considered here, $h'_1 = h'_2$. Representative error bars are as indicated.

Appendix F

Measured data

Tables F.1 and F.2 show thin interface experimental data as described in §3. Variables H (cm), h_1' (cm), η (cm), $U \pm 0.12$ (cm/s), ρ_0 (g/cm^3), ρ_1 (g/cm^3) and ρ_2 (g/cm^3) are described schematically in Fig. 2.1. Ambient and lock fluid interface thickness are denoted by δ_{amb} (cm) and δ_ℓ (cm) respectively. Numbers in the "Config" column represent subcritical (0), supercritical (1), in-between (2) and uniform ambient (3) gravity current cases. Table F.3 shows data from thick interface experiments, as described in §3.2 where $h_1' = h_2'$ and $H = 20\,\text{cm}$. Column labels are as in Tables F.1 and F.2. Non-dimensional lower ambient depth and interface thickness are denoted by h_1'/H and δ/H respectively. Table F.4 shows measured data for experiments investigating the deceleration of gravity currents after the slumping phase. The interface thickness is denoted by δ (cm) and the non-dimensional point of front deceleration is denoted by X/ℓ where ℓ is the lock length. The remaining column variables are as defined in Tables F.1 and F.2. In all experimental cases, we employ the following combination of channel height, H and lock length, ℓ: $H = 20\,\text{cm}$ with $\ell = 32.4\,\text{cm}$ and $H = 15\,\text{cm}$ with $\ell = 16.5\,\text{cm}$. The measurement error for experimental data are: H, h_1', h_2', $\ell \pm 0.15$, $\eta \pm 0.30$, $\delta \pm 0.20$, $\rho \pm 0.0005$ and $U \pm 0.12$. Finally, Table F.5 and F.6 show data from numerical simulations described in Tan et al. (2010a). Column labels are as in Tables F.1 and F.2.

Run	H	Target h_1'/H	D	h_2'	$H-D$	δ_{amb}	δ_l	ρ_0	ρ_1	ρ_2	η	U	Config
29	20.0	0.5000	15.0530	11.0043	4.9470	2.0642	1.2633	1.0433	1.0107	0.9995	4.4415	12.129	1
35	20.0	0.5000	5.0313	10.1457	14.9687	2.2137	0.8002	1.0457	1.0108	0.9988	2.4047	6.5942	1
30	19.9	0.5000	9.6595	11.7406	10.2655	2.2244	2.2246	1.0383	1.0099	0.9999	3.1273	10.2425	1
8	20.0	0.2500	5.2858	17.5512	14.7142	1.0180	3.0525	1.0315	1.0155	0.9985	2.5147	5.9259	2
9	20.0	0.2500	9.9200	16.8131	10.0800	0.9439	1.8889	1.0323	1.0159	0.9987	5.1784	8.6547	0
10	20.0	0.2500	10.3984	16.6876	9.6016	1.4154	2.1208	1.0217	1.0157	0.9986	4.7542	6.8095	0
11	20.0	0.2500	10.5910	16.6788	9.4090	1.5112	1.9500	1.0463	1.0104	0.9984	5.0143	11.4357	1
12	20.0	0.2500	10.3942	16.6607	9.6058	1.9388	2.1543	1.0275	1.0245	0.9988	4.3736	7.3461	0
13	20.0	0.7500	5.1127	5.1068	14.8873	2.1165	0.5153	1.0320	1.0154	0.9982	1.0151	5.7906	2
16	20.0	0.5000	5.1581	10.0532	14.8419	2.2225	0.7341	1.0330	1.0159	0.9984	1.5297	5.5206	0
7	20.0	0.5000	14.8605	10.8868	5.1395	1.6583	1.4964	1.0301	1.0145	0.9985	4.4896	8.8137	1
14	20.0	0.5000	3.9225	10.1013	16.0775	2.0312	1.2400	1.0302	1.0148	0.9991	0.9153	4.7341	0
22	20.0	0.5000	10.3502	11.7666	9.6498	1.6812	2.2958	1.0322	1.0159	0.9990	3.4795	7.7564	0
17	20.1	0.7500	10.4910	5.1235	9.559	2.2521	1.1395	1.0309	1.0150	0.9986	1.9467	7.6364	1
18	20.0	0.7500	14.8314	6.3029	5.1686	2.0498	1.3905	1.0307	1.0150	0.9987	2.1983	8.0889	1
19	20.0	0.0000	10.0987	20.0000	9.9013	0.0000	1.1242	1.0326	0.9992	0.9992	7.5672	10.8333	3
20	20.0	0.0000	5.1686	20.0000	14.8314	0.0000	0.7692	1.0300	1.0007	1.0007	4.2540	7.6875	3
21	20.0	0.0000	14.9152	20.0000	5.0848	0.0000	1.6497	1.0300	0.9987	0.9987	8.713	11.2065	3
0	20.0	0.750	20.0000	5.0000	0.0000	2.0000	0.0000	1.0387	1.0187	0.9991	2.4522	9.3794	1
39	20.0	0.5000	14.6811	10.9751	5.3189	2.1481	1.4840	1.0353	1.0261	0.9995	4.6556	7.8605	0
23	19.9	0.2500	14.3049	15.9483	5.5951	2.1370	1.3853	1.0330	1.0164	0.9991	6.7235	10.4729	1
24	20.0	0.2500	4.1245	15.1718	15.8755	1.3919	1.1069	1.0590	1.0147	0.9997	2.3045	8.2926	0
25	20.0	0.2500	4.6569	15.1475	15.3431	1.1584	1.8669	1.0306	1.0223	0.9993	0.7119	3.9262	0
26	20.0	0.2500	14.9687	15.9157	5.0313	2.0020	1.3381	1.0295	1.0220	0.9993	6.9964	9.2763	0
27	20.0	0.2500	15.5200	15.8581	4.4800	2.9443	1.3109	1.0257	1.02165	0.99955	7.1896	8.5541	0
28	20.0	0.2500	15.1723	16.0090	4.8277	1.0001	1.5320	1.0410	1.0102	0.9990	6.7433	12.0327	1
31	20.0	0.7500	14.7830	6.1618	5.2170	3.5878	1.2828	1.0470	1.0112	0.9989	2.3203	12.3512	1
33	20.0	0.7500	10.0778	5.1831	9.9222	2.0469	1.6050	1.0433	1.0105	0.9991	1.6908	10.765	1
34	20.0	0.7500	4.8874	5.1611	15.1126	2.3144	1.3304	1.0440	1.0105	0.9990	1.1351	8.2027	1
1	20.0	0.7500	20.0000	15.0000	0.0000	2.0000	0.0000	1.0016	1.0338	1.0250	-	12.5652	1
2	20.0	0.7500	20.0000	15.0000	0.0000	2.0000	0.0000	1.0046	1.0304	1.0234	-	10.5363	1
3	20.0	0.7500	20.0000	15.0000	0.0000	2.0000	0.0000	1.0005	1.0307	1.0079	-	6.5826	1

Table F.1: Thin interface experimental data. Column labels and units are described in text.

Run	H	Target h_1'/H	D	h_2'	$H-D$	δ_{amb}	δ_l	ρ_0	ρ_1	ρ_2	η	U	Config
5	20.0	0.2500	20.0000	15.0000	0.0000	2.0000	0.0000	1.0274	1.0150	0.9984	7.2673	9.6800	1
6	20.0	0.2500	20.0000	15.0000	0.0000	2.0000	0.0000	1.0201	1.0149	0.9983	7.1849	8.0300	2
7	20.0	0.2500	20.0000	15.0000	0.0000	2.0000	0.0000	1.0345	1.0149	0.9985	7.4592	11.0200	1
28	20.0	0.2500	20.0000	15.0000	0.0000	2.0000	0.0000	1.0331	1.0145	0.9985	7.1981	10.8250	1
8	20.0	0.2500	20.0000	15.0000	0.0000	2.0000	0.0000	1.0313	1.0082	0.9985	6.841	10.7300	1
9	20.0	0.2500	20.0000	15.0000	0.0000	2.0000	0.0000	1.0486	1.0063	0.9987	5.9681	13.4000	1
14	20.0	0.2500	20.0000	15.0000	0.0000	2.0000	0.0000	1.0562	1.0076	0.9983	5.9879	14.1150	1
15	20.0	0.7500	20.0000	5.0000	0.0000	2.0000	0.0000	1.0350	1.0252	0.9982	2.4950	6.6550	1
16	20.0	0.7500	20.0000	5.0000	0.0000	2.0000	0.0000	1.0354	1.0204	0.9984	2.4231	8.1150	2
17	20.0	0.7500	20.0000	5.0000	0.0000	2.0000	0.0000	1.0410	1.0176	0.9995	2.4547	10.0750	1
18	20.0	0.7500	20.0000	5.0000	0.0000	2.0000	0.0000	1.0366	1.0087	0.9983	2.2247	10.5550	1
19	20.0	0.7500	20.0000	5.0000	0.0000	2.0000	0.0000	1.0441	1.0053	0.9985	2.1060	12.6000	1
40	20.0	0.5000	4.3425	10.1250	15.6575	1.8896	0.6985	1.0353	1.0264	0.9994	0.0000	3.9867	0
45	20.0	0.5000	9.4100	10.2845	10.5900	2.2392	1.9804	1.0390	1.0290	0.9986	1.1272	0.0000	0
44	20.0	0.5000	4.5946	10.1228	15.4054	2.3965	0.9540	1.0365	1.0335	0.9994	-	-	0
20	20.0	0.5000	20.0000	10.0000	0.0000	2.0000	0.0000	1.0470	1.0056	0.9989	4.2978	13.1700	1
3	20.0	0.5000	20.0000	10.0000	0.0000	2.0000	0.0000	1.0316	1.0151	0.9989	5.0229	9.2200	1
25	20.0	0.3750	20.0000	12.5000	0.0000	2.0000	0.0000	1.0455	1.0163	0.9984	5.876	12.3400	1
26	20.0	0.8750	20.0000	2.5000	0.0000	2.0000	0.0000	1.0352	1.0160	0.9984	1.12915	8.8000	1
27	20.0	0.6250	20.0000	7.5000	0.0000	2.0000	0.0000	1.0364	1.0164	0.9986	3.8194	9.5700	1
10	20.0	0.7500	20.0000	5.0000	0.0000	2.0000	0.0000	1.0181	1.0153	1.0009	-	0.0000	0
4	20.0	0.7500	20.0000	5.0000	0.0000	2.0000	0.0000	1.0094	1.0446	1.0349	0.0000	12.4642	1
36	20.0	0.6250	5.1282	7.6269	14.8718	1.8022	1.1207	1.0962	1.0249	1.0004	1.6743	11.8649	1
38	20.0	0.3750	9.0820	12.6010	10.9180	1.5173	1.2751	1.0358	1.0264	0.9988	2.4719	6.3383	0
21	20.0	0.5000	20.0000	10.0000	0.0000	2.0000	0.0000	1.0370	1.0101	0.9987	4.8844	10.8750	1
22	20.0	0.5000	20.0000	10.0000	0.0000	2.0000	0.0000	1.0377	1.0156	0.9989	4.9816	10.2200	1
41	20.0	0.7500	5.0531	5.1436	14.9469	2.1318	0.5167	1.0369	1.0272	0.9991	0.0000	4.8624	0
42	20.0	0.7500	9.2500	5.1352	10.7500	1.9089	1.2857	1.0374	1.0275	0.9995	0.0000	5.3661	0
43	20.0	0.7500	14.8950	5.8944	5.1050	2.2673	1.3256	1.0371	1.0274	0.9993	2.2247	6.5413	0
23	20.0	0.5000	20.0000	10.0000	0.0000	2.0000	0.0000	1.0342	1.0206	0.9984	5.0954	8.6650	2
24	20.0	0.5000	20.0000	10.0000	0.0000	2.0000	0.0000	1.0358	1.0261	0.9992	5.0862	7.8800	1

Table F.2: Thin interface experimental data. Column labels and units are described in text.

Run	ρ_0	ρ_1	ρ_2	h_1'/H	δ/H	U
1	1.0316	1.0151	0.9989	0.500	0.0250	9.4693
2	1.0303	1.0150	0.9995	0.500	0.2400	9.1005
3	1.0311	1.0151	0.9988	0.500	0.3775	9.2358
4	1.0321	1.0153	0.9987	0.500	0.4800	9.5352
5	1.0308	1.0153	0.9986	0.500	0.1580	9.0296
6	1.0313	1.0151	0.9986	0.500	0.5814	9.3765
19	1.0313	1.0149	0.9993	0.500	0.8231	9.4488
23	1.0314	1.0148	0.9989	0.500	0.6899	9.4612
28	1.0328	1.0153	0.9992	0.500	0.8776	10.2314
34	1.0303	1.0155	1.0014	0.500	0.9739	9.2784
39	1.0315	1.0151	0.9989	0.500	0.0952	9.3524
7	1.0315	1.0225	1.0027	0.500	0.1542	7.6146
8	1.0334	1.0223	1.0006	0.500	0.2315	8.2186
9	1.0319	1.0223	1.0011	0.500	0.3541	7.9374
10	1.0334	1.0228	1.0008	0.500	0.4319	8.1877
11	1.0339	1.0228	1.0006	0.500	0.5043	8.3993
18	1.0335	1.0220	0.9993	0.500	0.8199	8.8185
22	1.0326	1.0217	0.9995	0.500	0.7452	8.7481
25	1.0348	1.0230	0.9989	0.500	0.5959	8.4457
27	1.0423	1.0285	1.0000	0.500	0.8807	9.7391
37	1.0290	1.0201	1.0026	0.500	0.9151	7.9994
38	1.0331	1.0222	0.9994	0.500	0.1075	8.0183
12	1.0459	1.0121	1.0007	0.500	0.2928	12.3344
13	1.0443	1.0100	1.0007	0.500	0.1685	12.0022
14	1.0383	1.0100	1.0007	0.500	0.2241	11.4602
15	1.0459	1.0106	1.0005	0.500	0.4006	12.3815
16	1.0465	1.0104	1.0005	0.500	0.5123	12.7764
17	1.0464	1.0101	0.9999	0.500	0.8384	12.7291
24	1.0448	1.0100	0.9995	0.500	0.6691	12.6283
26	1.0443	1.0095	0.9993	0.500	0.5476	12.4466
30	1.0511	1.0120	1.0001	0.500	0.8838	12.9840
35	1.0502	1.0129	1.0016	0.500	0.9536	13.1312
40	1.0413	1.0092	0.9995	0.500	0.1086	11.8545

Table F.3: Thick interface experimental data. Here $h_1' = h_2'$ and $H = 20\,\mathrm{cm}$. Column labels and units are as described in text.

Run	ρ_0	ρ_1	ρ_2	h_1'	δ	X/ℓ	U	η/H
SGC 2	1.0206	1.0184	0.9997	11.2500	2.0000	2.7856	2.9655	-
6	1.0302	1.0239	1.0002	11.2500	1.8769	6.1712	4.6336	-
3	1.0361	1.0245	0.9991	11.2500	2.0033	9.2245	5.8545	-
12	1.0265	1.0242	0.9987	7.5000	4.6276	4.2848	4.6752	-
15	1.0163	1.0148	0.9983	7.5000	8.7960	6.0651	4.1864	0.2144
SGC 5	1.0208	1.0186	0.9988	7.5000	2.0000	3.0206	4.3707	0.2637
5	1.0299	1.0236	1.0004	7.5000	1.7556	7.0522	5.7355	0.2547
17	1.0187	1.0145	0.9997	7.5000	8.7670	10.0317	5.0683	0.2405
7	1.0303	1.0211	0.9995	7.5000	1.9150	8.6665	6.1686	-
10	1.0345	1.0269	0.9991	5.6250	1.5019	8.8648	7.0596	-
SGC 4	1.0211	1.0194	0.9990	5.6500	2.0000	3.8410	5.1613	-
9	1.0283	1.0247	0.9988	3.7500	1.3599	12.0000	7.6368	-
4	1.0300	1.0236	1.0011	3.7500	1.7649	12.0000	7.9796	-
18	1.0269	1.0244	0.9986	7.5000	10.6210	12.0000	6.1313	0.2373
19	1.0250	1.0197	0.9999	7.5000	3.8084	6.9184	5.2281	-
20	1.0237	1.0184	0.9982	7.5000	4.1860	7.2320	5.4889	-
21	1.0202	1.0139	0.9982	7.5000	4.0462	9.5658	5.5056	-
22	1.0185	1.0163	0.9984	7.5000	9.2774	6.7293	4.6981	0.2180
23	1.0130	1.0116	0.9989	7.5000	6.2919	5.2672	3.7316	0.2347
24	1.0142	1.0107	0.9984	7.5000	6.5814	8.6665	4.3229	0.2240
25	1.0168	1.0127	0.9984	7.5000	7.1498	9.0631	4.7613	0.2394
26	1.0198	1.0134	0.9989	7.5000	7.0250	12.0000	5.4695	-
27	1.0262	1.0235	0.9986	4.7000	1.6969	7.6425	6.5204	-
11	1.0314	1.0216	0.9992	5.6250	2.0136	12.0000	7.2727	-
29	1.0380	1.0257	0.9982	7.5000	1.5830	10.1009	7.5351	-
31	1.0292	1.0194	0.9986	7.5000	1.8296	10.1239	6.5254	-
32	1.0252	1.0194	0.9994	7.5000	10.9744	12.0000	6.0119	0.2280
34	1.0208	1.0188	0.9992	7.5000	11.5013	7.3473	4.6978	0.2294
35	1.0225	1.02025	0.9989	7.5000	12.2600	9.3398	4.8839	0.2215
36	1.0283	1.0195	0.9986	7.5000	2.0190	10.4745	6.4030	-
37	1.02705	1.0184	0.9986	7.5000	4.0650	10.2992	6.3970	-
38	1.02985	1.021	1.0001	7.5000	3.9227	9.7826	6.3174	-

Table F.4: Experimental data for experiments considering the point of front deceleration. Here $H = 15\,\text{cm}$. Column labels and units are as described in text.

Case	h_1'	D	H	ρ_2	ρ_1	ρ_0	U	η	Config
384	12.0	5	20	1	1.015	1.02	2.81	-	0
385	16.0	5	20	1	1.015	1.02	2.93	-	0
386	8.0	5	20	1	1.015	1.02	3.63	-	-
207	10.0	20	20	1	1.01	1.02	6.77	5.00	2
208	5.0	20	20	1	1.01	1.02	7.91	7.43	1
209	15.0	20	20	1	1.01	1.02	6.23	2.40	1
210	20.0	20	20	1	1.01	1.02	6.08	-	3
226	0.0	20	20	1	1.01	1.02	8.73	-	3
227	12.5	20	20	1	1.01	1.02	6.44	3.63	2
228	17.5	20	20	1	1.01	1.02	6.08	1.14	2
229	7.5	20	20	1	1.01	1.02	7.23	6.21	2
230	2.5	20	20	1	1.01	1.02	8.55	8.33	1
215	10.0	20	20	1	1.015	1.02	5.48	5.07	0
216	5.0	20	20	1	1.015	1.02	7.57	7.43	0
217	15.0	20	20	1	1.015	1.02	4.58	2.57	0
220	20.0	20	20	1	1.015	1.02	4.25	-	3
226	0.0	20	20	1	1.015	1.02	8.73	-	3
236	12.5	20	20	1	1.015	1.02	4.94	3.78	0
237	17.5	20	20	1	1.015	1.02	4.34	1.19	2
238	7.5	20	20	1	1.015	1.02	6.41	6.29	0
239	2.5	20	20	1	1.015	1.02	8.75	8.50	1
222	10.0	20	20	1	1.005	1.02	7.78	4.49	1
223	5.0	20	20	1	1.005	1.02	8.24	6.99	1
224	15.0	20	20	1	1.005	1.02	7.52	2.27	1
225	20.0	20	20	1	1.005	1.02	7.44	-	3
226	0.0	20	20	1	1.005	1.02	8.73	-	3
232	12.5	20	20	1	1.005	1.02	7.64	3.24	1
233	17.5	20	20	1	1.005	1.02	7.49	1.05	1
234	7.5	20	20	1	1.005	1.02	7.95	5.86	1
235	2.5	20	20	1	1.005	1.02	8.52	7.68	1
397	2.5	15	20	1	1.01	1.02	8.46	-	1
398	17.5	15	20	1	1.01	1.02	5.99	-	1
391	18.0	15	20	1	1.015	1.02	4.20	-	2
392	2.0	10	20	1	1.015	1.02	8.13	-	1
393	2.0	5	20	1	1.015	1.02	5.74	-	0
394	17.5	10	20	1	1.01	1.02	5.64	-	2
395	17.5	10	20	1	1.005	1.02	6.81	-	1
396	17.5	5	20	1	1.005	1.02	5.04	-	1
999	2.0	15	20	1	1.015	1.02	8.78	-	1

Table F.5: Measured data from numerical simulations as described in Tan et al. (2010a). Column labels and units are described in text.

Case	h_1'	D	H	ρ_2	ρ_1	ρ_0	U	η	Config
347	10.0	5	20	1	1.01	1.02	4.30	-	0
350	5.0	5	20	1	1.01	1.02	4.11	1.84	0
353	15.0	5	20	1	1.01	1.02	4.06	-	0
372	2.0	5	20	1	1.01	1.02	5.72	-	1
373	18.0	5	20	1	1.01	1.02	4.24	-	2
348	10.0	10	20	1	1.01	1.02	5.84	3.50	0
351	5.0	10	20	1	1.01	1.02	6.92	6.11	2
354	15.0	10	20	1	1.01	1.02	5.68	2.10	0
241	2.5	10	20	1	1.01	1.02	7.73	6.98	1
242	7.5	10	20	1	1.01	1.02	6.35	5.05	0
349	10.0	15	20	1	1.01	1.02	6.60	4.65	2
352	5.0	15	20	1	1.01	1.02	7.58	6.81	1
355	15.0	15	20	1	1.01	1.02	6.21	2.31	1
356	10.0	10	20	1	1.005	1.02	7.14	3.96	1
357	5.0	10	20	1	1.005	1.02	7.54	5.71	1
358	15.0	10	20	1	1.005	1.02	6.53	1.93	1
359	2.5	10	20	1	1.005	1.02	7.66	5.91	1
360	7.5	10	20	1	1.005	1.02	7.16	5.16	1
362	10.0	15	20	1	1.005	1.02	7.74	4.47	1
363	5.0	15	20	1	1.005	1.02	8.26	6.68	1
364	15.0	15	20	1	1.005	1.02	7.53	1.91	1
365	2.5	15	20	1	1.005	1.02	8.55	-	1
366	17.5	15	20	1	1.005	1.02	7.49	-	1
367	2.5	5	20	1	1.005	1.02	5.70	5.04	1
368	5.0	5	20	1	1.005	1.02	5.52	-	1
369	7.5	5	20	1	1.005	1.02	5.40	-	2
370	10.0	5	20	1	1.005	1.02	5.39	-	2
371	15.0	5	20	1	1.005	1.02	5.18	-	2
361	10.0	10	20	1	1.015	1.02	3.61	1.37	0
374	4.0	10	20	1	1.015	1.02	7.07	-	0
375	8.0	10	20	1	1.015	1.02	4.68	-	0
376	12.0	10	20	1	1.015	1.02	3.79	-	0
377	16.0	10	20	1	1.015	1.02	3.93	-	0
378	4.0	15	20	1	1.015	1.02	7.93	-	2
379	8.0	15	20	1	1.015	1.02	6.11	-	0
380	12.0	15	20	1	1.015	1.02	5.00	-	0
381	16.0	15	20	1	1.015	1.02	4.32	-	0
382	4.0	5	20	1	1.015	1.02	3.25	-	0
383	8.0	5	20	1	1.015	1.02	2.56	-	0

Table F.6: Measured data from numerical simulations as described in Tan et al. (2010a). Column labels and units are described in text.